

# Heat Transfer Studies of Cryogel<sup>®</sup> Z under Mechanical Pressure for Large-Scale Insulation of Particle Detectors

MASTER THESIS  
by

**Lennard Niclas Busch, B.Sc.**

European Organisation for Nuclear Research  
Institute for Technical Thermodynamics and Refrigeration  
Faculty of Chemical and Process Engineering  
Karlsruhe Institute of Technology

Assignment/1 <sup>st</sup> Referee:	Prof. Dr.-Ing. Steffen Grohmann
2 <sup>nd</sup> Referee:	Prof. Dr.-Ing. Thomas Wetzel
Supervision:	Dr. rer. nat. Torsten Köttig

Handed in on: July 2, 2019



## Master thesis

for Mr. B.Sc. Lennard Niclas Busch

Heat transfer studies of Cryogel® under pressure for large-scale insulation of particle detectors

Untersuchungen zum Wärmedurchgang von Cryogel® unter Druckbelastung zur großflächigen Isolation von Teilchendetektoren

### Background:

The “*Future Circular Collider*” (FCC) project at CERN is dedicated to the planning of a larger particle collider compared to the LHC, using stronger magnetic fields. This requires a different design of particle detectors. As a consequence, the thermal insulation of the superconducting magnets inside the particle detectors must be transparent with regard to particle radiation, as they are located between the interaction point and the particle detecting layers.

The thermal insulation has to fulfil two purposes: First, the suitable thermal insulation of the cold mass at 4.5 K against the ambience and second, the mechanical support of the vacuum enclosure on the superconducting magnet structure. The forces on the insulation are equivalent to 1 bar of pressure difference. Cryogel® as a glass-fibre based aerogel shows encouraging properties to meet either requirement. An experimental set-up shall therefore be designed that allows the evaluation of the eligibility of Cryogel® in this application.

### Scope of work:

This Master thesis includes the construction and commissioning of a dedicated test set-up, where the required temperature levels shall be provided by a two-stage pulse-tube cryocooler. The thesis includes the following work packages:


- characterisation of the cryocooler performance,
- numerical simulations and detailed design of the cryostat,
- construction and commissioning of the set-up,
- heat transfer experiments with Cryogel®,
- data analysis and discussion of results.

The Master thesis shall be written in English language. A two-sided summary in German shall be submitted together with the thesis. In addition, the results shall be presented in a 20 minutes presentation in the ITTK Institute seminar at KIT.

Start of work: 02.01.2019

Thesis submission:

Supervisor: Dr. Torsten Köttig (CERN, TE Department, Cryogenics  
Group, [torsten.koettig@cern.ch](mailto:torsten.koettig@cern.ch))



---

Prof. Dr.-Ing. Steffen Grohmann



## Declaration/ Erklärung

I hereby certify that this work has been composed only by me and no other than the named sources were used. I also agree that this thesis may be displayed in a library and excerpts may be copied.

Hiermit erkläre ich, diese Arbeit selbstständig angefertigt, alle benutzten Hilfsmittel vollständig und genau angegeben und alles kenntlich gemacht zu haben, was aus Arbeiten anderer unverändert oder mit Änderungen entnommen wurde.

Ich bin damit einverstanden, dass diese Arbeit der Öffentlichkeit ganz oder in Auszügen in gedruckter Form in der Bibliothek des Instituts für Thermische Verfahrenstechnik sowie als elektronisch publiziertes Dokument auf einem Fileserver zugänglich gemacht wird, falls es im Interesse des Instituts liegt. Dies beinhaltet die Möglichkeit, die Arbeit ganz oder in Auszügen zu kopieren.

---

Karlsruhe, July 2, 2019

# Acknowledgement

To start with, I would like to express my gratitude to Prof. Steffen Grohmann, whose lectures excited my curiosity in the field of cryogenics years ago at the KIT. He furthermore introduced me to CERN and made the conduction of this work possible for me by encouraging and supporting my application there.

Moreover, I want to thank my supervisor Dr. Torsten Köttig for the helpful discussions, his regular ideas, feedback and his constant guidance in cryogenics. His advice and backing of my work was essential to the success of this thesis and constantly motivated me at the workplace. His efforts in maintaining an outstanding working climate among the technical and PhD students in the Central Cryogenic Laboratory at CERN made my stay there truly exceptionally enjoyable.

At this point, I would also like to highlight my deepest gratitude to Madam Patricia Bourges Sousa. She guided me through the work in the laboratory, was available every time I was looking for further advice and proved to be an extraordinary proofreader of this thesis. Even beyond the working life, I could always count on her.

Furthermore, I want to take the opportunity here to thank my girlfriend Maria Anna Fonnesu, which I met at CERN and who continuously supported me during my stay there, especially in challenging times.

My gratitude additionally extends to the members of the Central Cryogenic Laboratory and the EP-ADO-SO section at CERN. Their experience, advice and the fruitful discussions with them were extremely valuable and highly appreciated. In particular, I want to mention Dorothea Fonnesu, Remy Kriboo, Kirtana Puthran, Mário Grosso Xavier and Agostino Vacca. Gratitude I owe also to my sister Anja Busch for her gladly accepted proofreading skills.

Finally, since this thesis marks the end of my studies as a process engineering student, I would further like to thank my family and friends for supporting me during all these years with the joys and challenges that came along with them.

## Abstract

The development of detectors for hadron-hadron colliders is one of the major challenges in the evolution process of the Future Circular Collider project at CERN. The ultrathin solenoid concept aims at significantly improving the magnetic field distribution efficiency within the detectors. Its design calls for a thermal insulation of the cold mass at 5 K that has to offer structural support while being sufficiently transparent for particle detection. The insulation material Cryogel<sup>®</sup>Z shows promising properties in this context. This thesis comprises the development of an experimental test setup that allows the evaluation of the Cryogel Z's eligibility for application in an ultrathin solenoid and first test results. The generation of two low-temperature levels by a pulse-tube refrigerator and the vacuum vessel were preconditions to the design of the experimental setup. Thus, after acquiring detailed performance data of the novel pulse-tube refrigerator with a given test stand, numerical simulations were conducted using these data to determine feasible design dimensions for the experimental setup. Based on the obtained dimensioning results, the new setup was designed in detail, commissioned and installed.

With this setup, first experiments were conducted using heat meters which determined heat loads through the Cryogel Z on the cold mass and an intermediate thermal shield, whose temperature was varied between 40 K and 80 K. In analogy with the conditions in the ultrathin solenoid, the Cryogel Z was compressed by a 1 bar mechanical pressure load throughout the conducted experiments. The obtained experimental results revealed the heat load values per square meter of 7-layer Cryogel Z insulation on both the cold mass and the thermal shield for shield temperatures of 40 K, 53 K and 80 K. Considering the results obtained in this work and the coefficients of performance of the existing cryoplants at CERN, a determination of an optimum thermal shield temperature of 46..47 K was possible.



---

## Abstract - German Version

Am CERN, der Europäischen Organisation für Kernforschung, wurde jüngst die Future Circular Collider-Studie präsentiert, welche einen Nachfolger des Large Hadron Colliders, der momentan am CERN betrieben wird, darstellt. Im Rahmen der Forschung zu dieser Studie werden unter anderem Entwürfe für neuartige, leistungsfähigere Partikeldetektoren untersucht. Ein Konzept zur Effizienzsteigerung der Magnetfeldverteilung innerhalb der Detektoren sind sogenannte ultrathin solenoids. Die in diesem Konzept vorgesehene Anordnung der kalten, supraleitenden Magnetspulen in den Detektoren unterscheidet sich von bisher existierenden Anlagen. Dies macht den Einsatz einer thermischen Isolierung der Spulen bei 5 K notwendig, die als Strukturträger gegen einen Differenzdruck von 1 bar fungiert und gleichzeitig hinreichend durchlässig für Partikeldetektion ist. Diesbezüglich weist das Isoliermaterial Cryogel<sup>®</sup>Z vielversprechende Eigenschaften aus. Die vorliegende Arbeit umfasst die Entwicklung und Installation eines experimentellen Aufbaus, der eine Beurteilung der Eignung von Cryogel Z für den Einsatz in ultrathin solenoids erlaubt, sowie die Durchführung und Auswertung erster Versuche. Die Bereitstellung von Kälteleistung auf zwei verschiedenen Temperaturstufen durch einen Pulsröhrenkühler und das Kryostatgefäß waren dabei bereits vorgegebene Randbedingungen im Bezug auf das Design des experimentellen Aufbaus. Zu dessen Dimensionierung wurden numerische Simulationen mit verschiedenen Modellgeometrien durchgeführt. Dazu wurden mit einem bereits bestehenden Teststand zuvor detaillierte Leistungsdaten des Pulsröhrenkühlers ermittelt. Anhand der so gewonnenen Bemaßungsergebnisse wurde der neue experimentelle Aufbau ausführlich konstruiert, installiert und in Betrieb genommen.

Mit diesem Aufbau wurden weiterhin erste Experimente durchgeführt, innerhalb derer, auf Basis von *in-situ* Wärmestromsensorkalibrierungen die Wärmelasten durch das Cryogel Z auf die kalte Masse bei 5 K und auf das thermische Schild bestimmt wurden. Hierbei wurde die Schildtemperatur zwischen 40 und 80 K variiert, um Erkenntnisse über die optimale Einsatztemperatur des Schildes zu gewinnen. Analog zu den Umgebungsbedingungen in den ultrathin solenoids wurde Cryogel Z über alle Versuche hinweg mit einem Drucklast von 1 bar komprimiert. Als Ergebnis wurden Werte für die Wärmestromdichten durch eine 7-lagige thermische Isolierung mit Cryogel Z auf die kalte Masse und das thermische Schild bei 40, 53 und 80 K erhalten. Unter Verwendung der in dieser Arbeit gewonnenen Ergebnisse und Berücksichtigung der Leistungszahlen der betriebenen Kälteanlagen am CERN konnte die optimale Einsatztemperatur des thermischen Schildes von 46 bis 47 K bestimmt werden.

# Contents

<b>Abstract</b> . . . . .	<b>I</b>
<b>Abstract - German Version</b> . . . . .	<b>II</b>
<b>Symbols and Abbreviations</b> . . . . .	<b>V</b>
<b>1 Introduction</b> . . . . .	<b>1</b>
1.1 CERN . . . . .	1
1.2 Future Circular Collider Project . . . . .	2
1.2.1 Particle Detector Solenoid Insulation . . . . .	3
1.2.2 Cryogel <sup>®</sup> Z - Insulator . . . . .	5
<b>2 Objective</b> . . . . .	<b>8</b>
<b>3 Theoretical Background</b> . . . . .	<b>9</b>
3.1 Cooling Principle . . . . .	9
3.2 Finite Element Method . . . . .	15
3.3 Instrumentation . . . . .	17
3.3.1 Joule Heating . . . . .	17
3.3.2 Resistance Thermometers . . . . .	18
3.3.3 Heat Meters . . . . .	20
3.3.4 Four-Terminal Sensing . . . . .	22
3.3.5 Measurement Uncertainty Evaluation Methods . . . . .	23
<b>4 Test Setup Development</b> . . . . .	<b>26</b>
4.1 Mechanical Pressure Application on Cryogel <sup>®</sup> Z . . . . .	26
4.2 Cryocooler Capacity Determination . . . . .	29
4.2.1 Measurement Setup and Methodology . . . . .	30
4.2.2 Cryocooler Performance . . . . .	32
4.3 Numerical Simulations . . . . .	33
4.3.1 Model Geometry . . . . .	33
4.3.2 Defined Model Setup Conditions . . . . .	35
4.3.3 Simulation Results . . . . .	37
4.4 Final Experimental Setup . . . . .	39
4.4.1 3D Test Stand Model . . . . .	40
4.4.2 Key Setup Parts and Measurement Device Placement . . . . .	41
<b>5 Heat Transfer Experiments with Cryogel<sup>®</sup>Z</b> . . . . .	<b>45</b>
5.1 Measurement Methodology . . . . .	45
5.2 Experimental Results . . . . .	48
<b>6 Results Discussion</b> . . . . .	<b>53</b>
6.1 Experimental Results Evaluation . . . . .	53
6.2 Experimental and Numerical Results Comparison . . . . .	54
6.3 Conclusion for Cryogel <sup>®</sup> Z Application . . . . .	56
<b>7 Proposals for Future Research and Development</b> . . . . .	<b>57</b>

---

<b>Bibliography</b> . . . . .	<b>62</b>
<b>List of Figures</b> . . . . .	<b>67</b>
<b>List of Tables</b> . . . . .	<b>68</b>
<b>Appendix</b> . . . . .	<b>69</b>
<b>A Material Specifications</b> . . . . .	<b>69</b>
<b>B Equipment Specifications</b> . . . . .	<b>70</b>
<b>C Soft Calibration</b> . . . . .	<b>72</b>
<b>D Calculation of Measurement Uncertainties</b> . . . . .	<b>74</b>
<b>E Parasitic Heat Load Estimation</b> . . . . .	<b>77</b>
<b>F Tabulated Result Values</b> . . . . .	<b>80</b>

## Symbols and Abbreviations

Abbreviation	Description
ASTM	American Society for Testing and Materials
ATLAS	A Toroidal LHC Apparatus
CERN	European Organisation for Nuclear Research
CG	Cryogel <sup>®</sup> Z
ee <sup>+</sup>	Electron-Positron
EH	Electric Heater
ESPP	European Strategy for Particle Physics
FCC	Future Circular Collider
FEM	Finite Element Method
GM	Gifford-McMahon
GUM	"Guide to the Expression of Uncertainty in Measurements"
hh	Hadron-Hadron
HMC	<i>In-Situ</i> Heat Meter Calibration
HP	High Pressure
HX	Heat Exchanger
LINAC2	"Linear Accelerator 2" (CERN)

<b>Abbreviation</b>	<b>Description</b>
LHC	Large Hadron Collider
LP	Low Pressure
MLI	Multilayer Insulation
NASA	National Aeronautics and Space Administration
OFHC	Oxygen-Free High-Thermal Conductivity
PTR	Pulse Tube Refrigerator
PS	"Proton Synchrotron" (CERN)
RRR	Residual Resistance Ratio
SPS	Super Proton Synchrotron
TT	Temperature Sensor
TVO	Carbon Ceramic Temperature Sensor (from Russian)

<b>Symbol (Latin)</b>	<b>Description</b>	<b>Unit</b>
$a$	Accommodation Coefficient	[ - ]
$A$	Area	[ m <sup>2</sup> ]
$c_p$	Isobaric Heat Capacity	[ $\frac{\text{J}}{\text{kg}\cdot\text{K}}$ ]
$c_v$	Isochoric Heat Capacity	[ $\frac{\text{J}}{\text{kg}\cdot\text{K}}$ ]
$e$	Emissivity	[ - ]
$f$	Rotation Frequency	[ Hz ]
$I$	Electric Current	[ A ]
$l$	Length	[ m ]
$M$	Molar Mass	[ $\frac{\text{kg}}{\text{mol}}$ ]

<b>Symbol (Latin)</b>	<b>Description</b>	<b>Unit</b>
$p$	Pressure	[ Pa ]
$P$	Acoustic Power of a Pressure Oscillator	[ W ]
$q$	Generic Measured Quantity (acc. to [1])	[ respective ]
$\dot{q}$	Heat Flux	[ $\frac{W}{m^2}$ ]
$\dot{Q}$	Heat Flow	[ W ]
$R$	Molar Gas Constant	[ $\frac{J}{K \cdot mol}$ ]
$R_i$	Electrical Resistances	[ $\Omega$ ]
$s$	Standard Uncertainty	[ respective ]
$S$	Entropy	[ $\frac{J}{K}$ ]
$T$	Temperature	[ K ]
$U$	Voltage	[ V ]
$V$	Volume	[ $m^3$ ]
$x$	Spatial Coordinate	[ m ]
$X$	Generic Input Quantity	[ respective ]
$Y$	Generic Output Quantity	[ respective ]

<b>Symbol (Greek)</b>	<b>Description</b>	<b>Unit</b>
$\epsilon$	Dilatation	[ - ]
$\Theta$	Integration Variable	[ K ]
$\kappa$	Isentropic Exponent	[ - ]
$\lambda$	Thermal Conductivity	[ $\frac{W}{mK}$ ]
$\sigma$	Stefan-Boltzmann Constant	[ $\frac{W}{m^2K^4}$ ]
$\phi$	Rotational Angle	[ rad ]

# 1 Introduction

## 1.1 CERN

This thesis' work was conducted at the European Organisation for Nuclear Research (CERN). CERN was founded by the ratification of its first twelve member states as an intergovernmental organisation in 1954 with the mission to provide for collaboration among European states in nuclear and particle physics research. 65 years later, CERN counts 23 member states that all contribute to the capital and operating costs [2]. By now, it is also operating the largest particle accelerator complex in the world whose main components are shown in Fig. 1.1 [3].

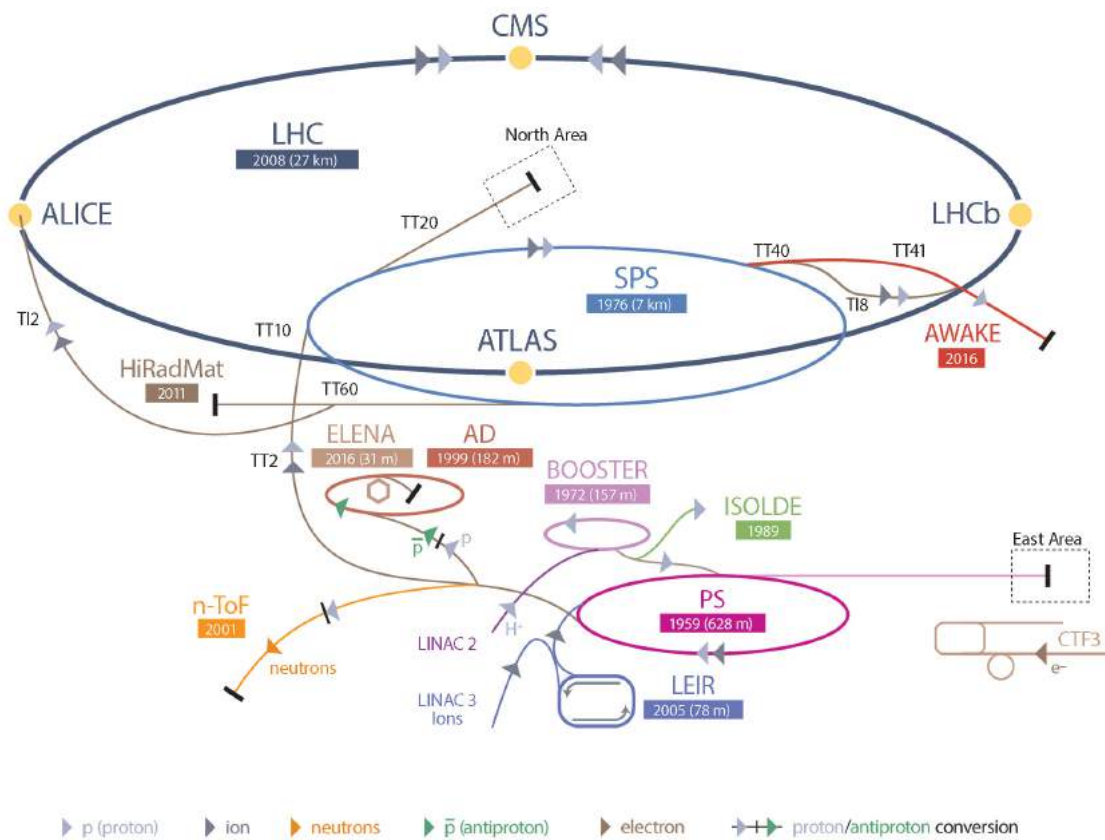


Figure 1.1: Schematic of the CERN accelerator complex [2]. Specifically, the LHC accelerator chain starts with the proton source, followed by LINAC2, the BOOSTER, the PS and the SPS, from where the beams are injected in the LHC. All the accelerators are connected by beam transfer lines (TT).

As seen in Fig. 1.1, the largest particle accelerator at CERN is the circular "Large Hadron Collider" (LHC) with a length of 26.7 km. The LHC allows the acceleration of protons or lead ions to a speed only negligibly lower than the speed of light, creating two beams of the respective particles thinner than a human hair that travel in opposite directions. At four different locations along the beam tubes (ATLAS, CMS, ALICE, LHCb), these two beams cross each other and the particles can collide with extremely high respective energies. These high-energy particle

collisions offer insights into fundamental physics research fields such as the Standard Model, dark matter, dark energy and extra dimensions. To allow for the high particle acceleration but also their deceleration and the required bending of the beams, strong magnetic fields of more than 8 T need to be provided. This requires extremely high electric currents in the electromagnets making the use of superconducting materials imperative. In its superconducting state, a material conducts direct current electricity with practically no electrical resistance [4]. For spatial reasons in the underground-located LHC-tunnel and reasons of energetic efficiency, no practical solution could have been designed using regular electromagnets [5]. The LHC dipole magnets use niobium-titanium (NbTi) cables that become superconducting below a temperature of about 9 K [6]. In fact, the NbTi-cables are cooled down even further to 1.9 K by pumping on a helium bath heat exchanger (HX), forming superfluid helium.

## 1.2 Future Circular Collider Project

The most famous research result from the LHC is arguably the observation of the Higgs boson [7] in 2012 that led to the awarding of the nobel prize in physics to François Englert and Peter W. Higgs for the theoretical prediction of the Higgs boson in 1964 [8]. This observation "completes the matrix of particles and interactions that has constituted the "Standard Model" for several decades." [9]. The so-called "Standard Model" in physics is a consistent and predictive theory that has been continuing to successfully describe all phenomena accessible to collider experiments. Nevertheless, there are several experimental facts that require the extension of the Standard Model and an explanation for observations such as the abundance of matter over antimatter, the striking evidence for dark matter and the non-zero neutrino masses is still lacking [9]. However, the LHC can, for the moment, merely provide a centre-of-mass particle collision energy that is deemed too low to produce new particles that would allow further research beyond the Standard Model [10]. The maximum energy achievable by the particles in the LHC is limited by the maximum bending field generated by the dipole magnets and by the radius of the tunnel arcs [11]. To drive the extension of the Standard Model forward in spite of the restrictions of the current highest-energy particle collider in the world [2], the European Strategy for Particle Physics (ESPP) 2013 update thus stated that "To stay at the forefront of particle physics, Europe needs to be in a position to propose an ambitious post-LHC accelerator project at CERN [...]" [12]. Hence, extensive studies have been conducted on the construction and benefits of a larger particle collider (100 km circumference) or "Future Circular Collider" (FCC, see Fig. 1.2) that would, among other things, offer significantly higher collision energies (e.g. [9], [10], [13]). This work belongs to the range of studies at CERN for the FCC. To allow for a better imagination of the spacial dimensions of the FCC concept, a scale comparison to the existing LHC is given in the following figure.



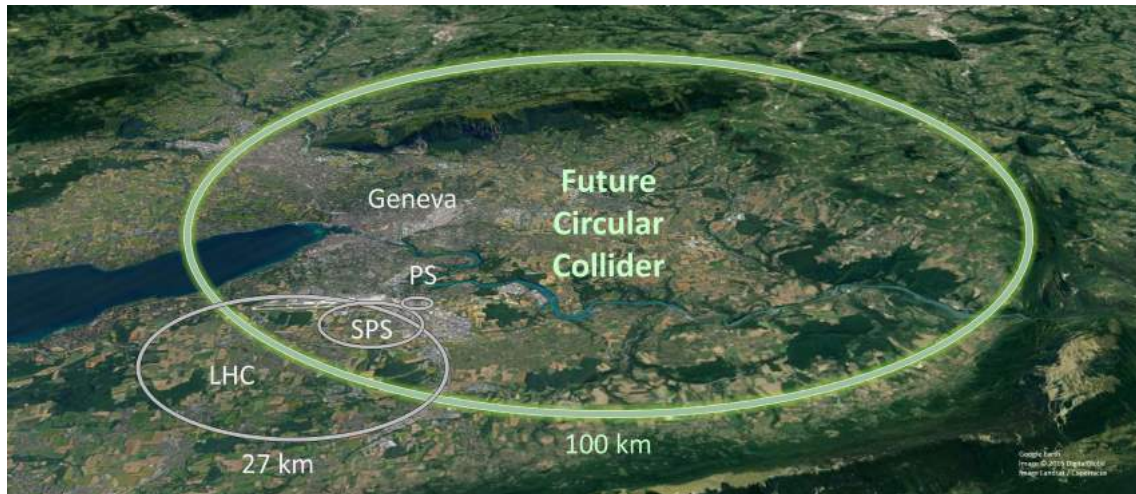


Figure 1.2: Scale comparison of the existing particle collider complex in Geneva and the FCC concept [14].

### 1.2.1 Particle Detector Solenoid Insulation

The Future Circular Collider study includes designs for higher-performance and possibly more cost-effective particle detectors [13]. The baseline concept for FCC hadron-hadron (FCC-hh) detectors can be seen in Fig. 1.3.

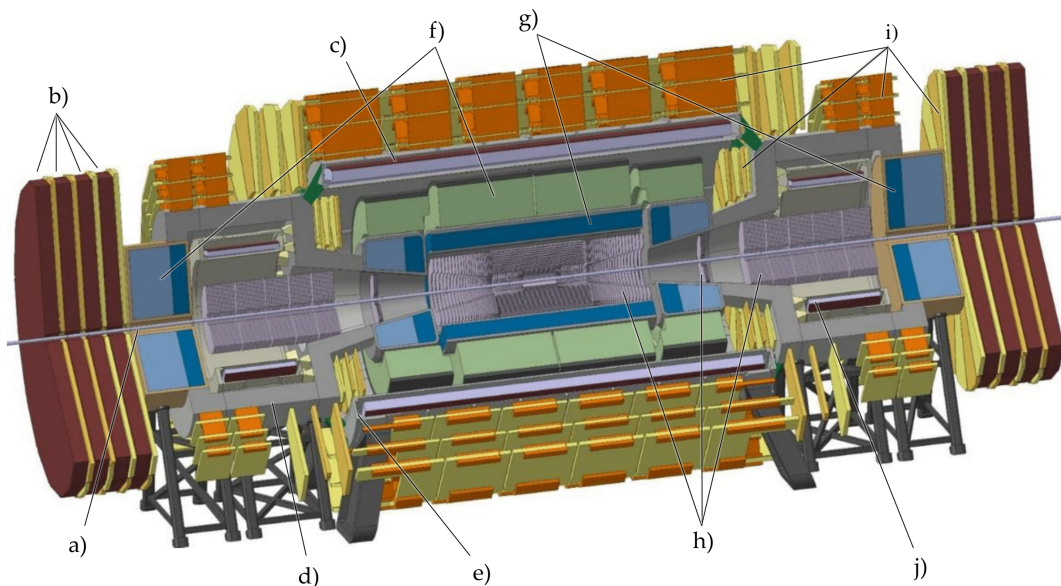


Figure 1.3: Baseline concept for FCC-hh detectors. Main components: a) Beam Tube b) Muon Absorber Disks c) Main Solenoid d) Radiation Shield e) Vacuum Vessel f) Electromagnetic Calorimeters g) Hadronic Calorimeters h) Trackers i) Muon Chambers j) Forward Solenoid. Based on [15].

The complete functional principle of the FCC particle detectors does not lie within the scope of this work. Instead, the focus is on the arrangement of solenoids, (particle) trackers, muon chambers and calorimeters. A disadvantage of the baseline

design from Fig. 1.3 is that the generated magnetic field by the solenoid is not used optimally. Most of the stored magnetic energy is found in the magnetic field over the volume of the calorimeters, although the performance of the calorimeters is not correlated to the magnetic field. If the magnetic field is only applied to the tracker and muon chambers (see Fig. 1.3), then the stored magnetic energy of the system may be reduced without (necessarily) affecting the performance of the detector in a detrimental manner [15]. A solution for this issue could be offered by the concept of the two Tesla ATLAS Solenoid [16]. A different arrangement of the above listed detector parts would lead to a magnetic field generation on the tracker and muon chambers only. This would mean a reduction of stored energy in the detector by around 76 % which would cut the operating costs by around 52 % [17]. The different arrangement is shown in Fig. 1.4.

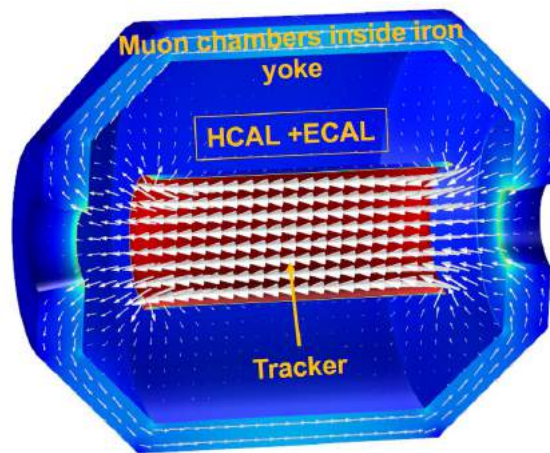


Figure 1.4: Ultrathin solenoid concept with magnetic field lines. Figure based on [18]. The tracker is placed inside the superconducting solenoid, whereas the calorimeters are placed outside of it. An iron yoke is used to return the flux, thus completely shielding the magnetic field and providing the field integral needed to tag muons.

Fig. 1.4 shows the concept of locating the cold, superconducting solenoid and its cryostat directly around the tracker. This imposes new challenges for both the cryostat and the solenoid itself because they are located in between the beam tube and the calorimeters and muon chambers that the particles need to reach after the collision. Therefore, solenoid and cryostat need to have the lowest particle scattering potential possible. Low material thickness and density is essential for the cryostat [19]. To find the most suitable solution, two development routes are being followed at CERN for FCC-electron-positron (FCC- $ee^+$ ) detectors. While Silva et al. [20] are looking into minimizing the wall thickness of a rather classical cryostat around the solenoid, the other approach is to use even thinner vacuum vessel walls supported by a material providing thermal insulation and structural support (see Fig. 1.5). This work is part of the research on that approach.

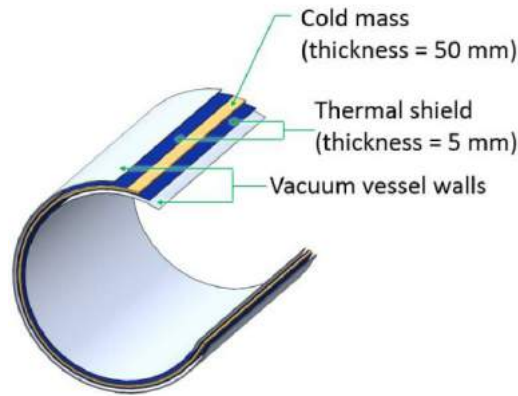


Figure 1.5: Conceptual scheme of the FCC-ee<sup>+</sup> cylindrical cryostat with a 4 m bore and 6 m length [19].

Due to the lack of sufficient rigidity, very thin vacuum vessel walls would collapse to the inside of the cryostat when pumping vacuum on it due to the induced pressure difference. Fig. 1.5 shows that those vessel walls would then be in contact with the insulation material located inside the vessel, applying a mechanical pressure load on it. This insulation material is located on both inside and outside of the thermal shield whose temperature can be varied within feasible limits. Its thickness is low, too which leads to the same mechanical pressure application on the insulation material on the inside. Hence, the insulation must also offer the structural support for the pressure difference of ultra-high vacuum inside the vessel and atmospheric pressure outside.

### 1.2.2 Cryogel<sup>®</sup>Z - Insulator

In advance to this thesis, an insulation material eligible for the ultrathin solenoids (see Fig. 1.5) had to be identified. As can be derived from the preceding chapter, materials of interest need to meet the following requirements:

- sufficient mechanical resistance against a 1 bar equivalent pressure load
- low density
- low thermal conductivity
- thinly applicable in large cylindrical shapes while still providing all of the above

Cryogel Z<sup>®</sup> [21], a flexible silica-based aerogel manufactured by Aspen Aerogels, Inc. in blankets of either 5 mm or 10 mm thickness shows promising properties [22]. In the 1990s, Aspen Systems Inc. developed a manufacturing method that significantly increased production efficiency of the until that time hard-to-handle aerogel with high production costs. In recent years it has been used, for example, by NASA in launch vehicle applications, Space Shuttle upgrades and life support equipment [23]. It was also at NASA that effective thermal conductivity measurements had already been conducted in the past [24]. However, there was no

applied mechanical pressure on the Cryogel Z and no intermediate temperature shield involved.

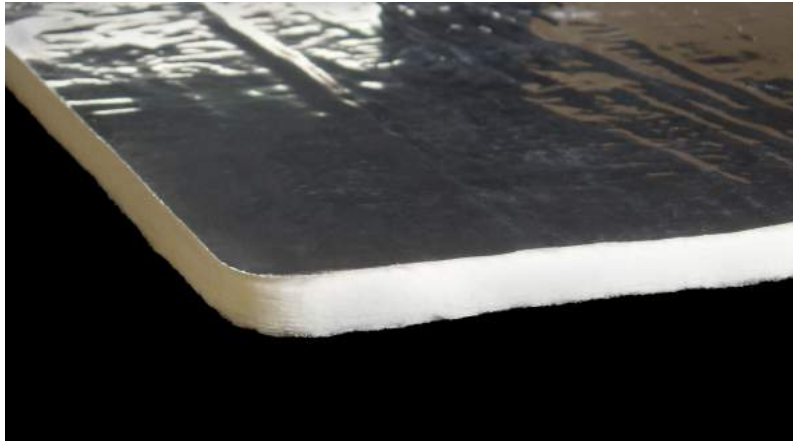


Figure 1.6: Photo of a 10 mm thick Cryogel Z blanket as sold by Aspen Aerogels<sup>®</sup>, Inc. [25]. On the top surface, a layer of glued aluminum foil can be seen. This is intended to prevent gases and humidity from penetrating the otherwise porous aerogel blankets in its application.

Its low density of only  $160 \frac{\text{kg}}{\text{m}^3}$ , applicability in thin layers and durability and flexibility at low temperatures [22] are attractive properties for the previously explained purpose. Additionally, prior to the work on this thesis, small-scale tests were performed at CERN to retrieve additional thermal conductivity data of Cryogel Z to assure its eligibility for the larger-scale test (see section 5). These had to be done at an applied pressure of 1 bar on the Cryogel Z to account for the compression it would have to withstand in the FCC-ee<sup>+</sup> detector design (see section 1.2.1). Amongst other thermal conductivity values for comparison, the results of these tests can be seen in Fig. 1.7.

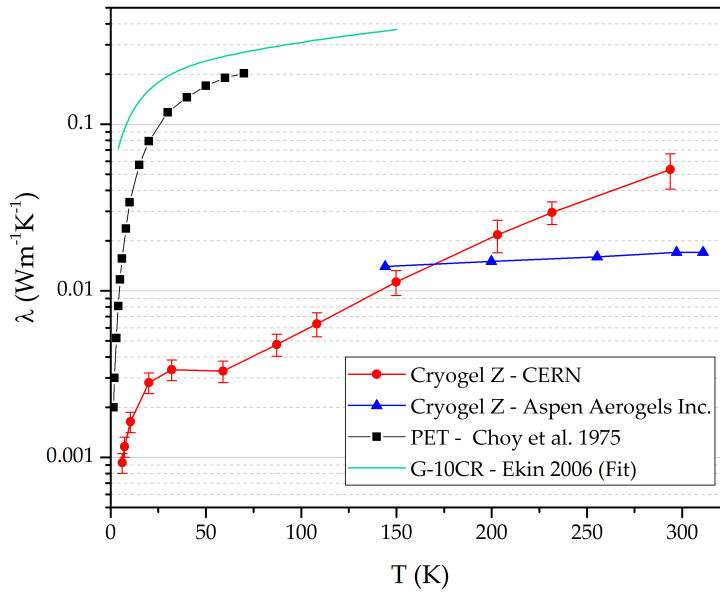


Figure 1.7: Various thermal conductivity data ([6] and [26]). The values provided by Aspen Aerogels Inc. were acquired according to ASTM C177 ([22] and [27]). The data on G-10CR were fitted to experimental values of the author.

There are two major insights to be gained from Fig. 1.7. The first one is how well Cryogel Z thermally insulates in comparison to the commonly used electrical insulator G-10CR in cryogenics, even when compressed with a 1 bar equivalent pressure at CERN. However, Cryogel Z in this state also shows a thermal conductivity that is about an order of magnitude lower at around 25 K than the one of Polyethylene Terephthalate (PET) which is the base material of Multilayer Insulation (MLI), the most common and most efficient commercially available thermal insulation. For the investigated purpose, however, MLI was not found to be eligible due to its lack of structural support (see Fig. 1.5). It also has to be noted that a clear trend of rising thermal conductivity with temperature was determined in the own experiments whereas the supplier data shows a rather constant value between 150 K and 300 K at 140 mbar compression [27].

## 2 Objective

Having previously identified Cryogel<sup>®</sup>Z as a promising thermal insulation material, the contribution of this thesis to the FCC study by CERN is to determine the heat fluxes through Cryogel Z on the cold mass and thermal shield according to Fig. 1.5. It was a given specification by the client within CERN ("FCC Detector Magnets Working Group") that the thermal shield temperature could be varied between 40 and 80 K while the cold mass should be maintained at around 5 K maximum.

While the thermal conductivity measurements on Cryogel Z from Fig. 1.7 were small-scale measurements with merely two different temperature boundaries of the Cryogel, it was the aim of this work to recreate the insulation conditions for the Cryogel Z including an intermediate temperature shield as seen in Fig. 1.5 and conduct the heat flux measurements with the largest Cryogel Z sample sizes possible. The restrictions on these sample sizes were the cooling capacities of both stages of the available "PT420" cryocooler by Cryomech<sup>®</sup> Inc. (see sections 3.1 and 4.2) and the dimensions of the vacuum vessel provided by the client (see sections 4.4 and 4.4.1).

In a first step, a simplified mock-up had to be established that would verify the working principle of the thermal insulation scheme at low temperatures using a cryocooler while compressing the Cryogel Z samples with a 1 bar equivalent mechanical pressure (see section 4.1). To gain detailed knowledge about the cooling capacities of a novel Cryomech<sup>®</sup>PT420 cryocooler, its capacity map was determined using a prepared test setup provided by the Central Cryogenic Laboratory at CERN (see section 4.2). This performance data enabled a preliminary design of the mock-up experiment with the goal to maximize the tested cross section of the Cryogel Z. Based on the mock-up geometries, numerical simulations had to be carried out to determine the maximum Cryogel Z sample sizes that still allowed for reaching the requested temperature levels of the temperature shield and the cold mass (see section 4.3). These results then allowed the exact dimensioning, ordering and installation of all interior parts of the test setup cryostat (see section 4.4). The final part of this work was to conduct the experiments whose outcomes offer a sound basis for the suitability assessment of Cryogel Z for insulating the superconducting magnets within the ultrathin solenoid concept [18].

### 3 Theoretical Background

#### 3.1 Cooling Principle

This work's method of choice to reach the required low temperatures is based on a two-staged pulse tube refrigerator (PTR) due to feasibility reasons of the shifting setup interior (see section 4.4) and the large time constants during measurements (see section 5.2). The general idea of the resulting cryostat structure can be seen in Fig. 3.1.

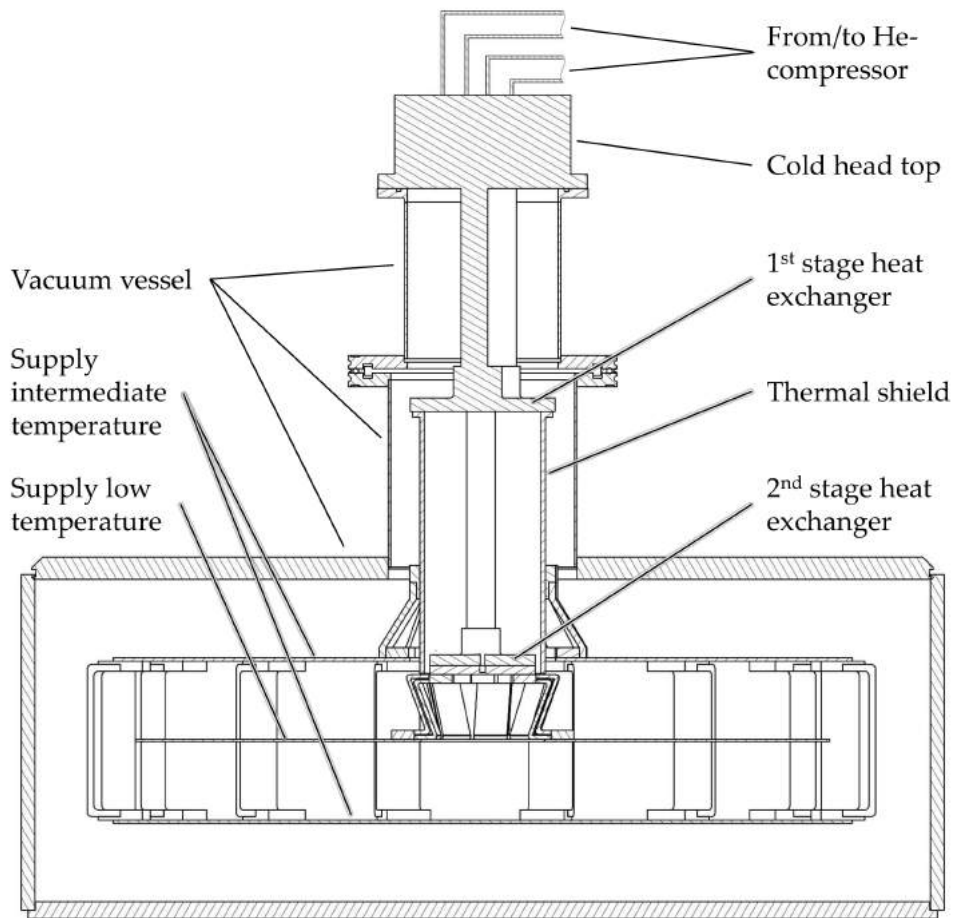


Figure 3.1: Simplified sketch of a basic cryostat with an inserted Pulse Tube refrigerator cold head (own figure). The cold head with two temperature stages is flanged onto the vacuum vessel. To shield the colder second stage against thermal radiation from the vacuum vessel walls, the thermal shield is flanged onto the heat exchanger of the first stage. Both stages enable the required temperature levels on large surfaces for the mock-up experiment (see section 4).

In the following, the different main pieces of equipment (cryocooler, cryostat and insulation) that allowed for the generation and maintenance of low temperatures according to the scheme in Fig. 3.1 will be described in further detail.

### Pulse Tube Cryocoolers

There are various types of cryocoolers available on the market with different working principles. The client's choice for the pulse tube refrigerator was based on its operation simplicity in a relatively wide temperature range when compared to other types and significantly lower mechanical vibrations in the cold finger. These are due to the absence of moving mechanical parts inside the cold head. The structure of a typical PTR consists of the pulse tube itself, a pressure generator, a regenerator matrix and a heat exchanger in the cold head (see Fig. 3.2). All components are directly in contact with helium which serves as the working fluid.

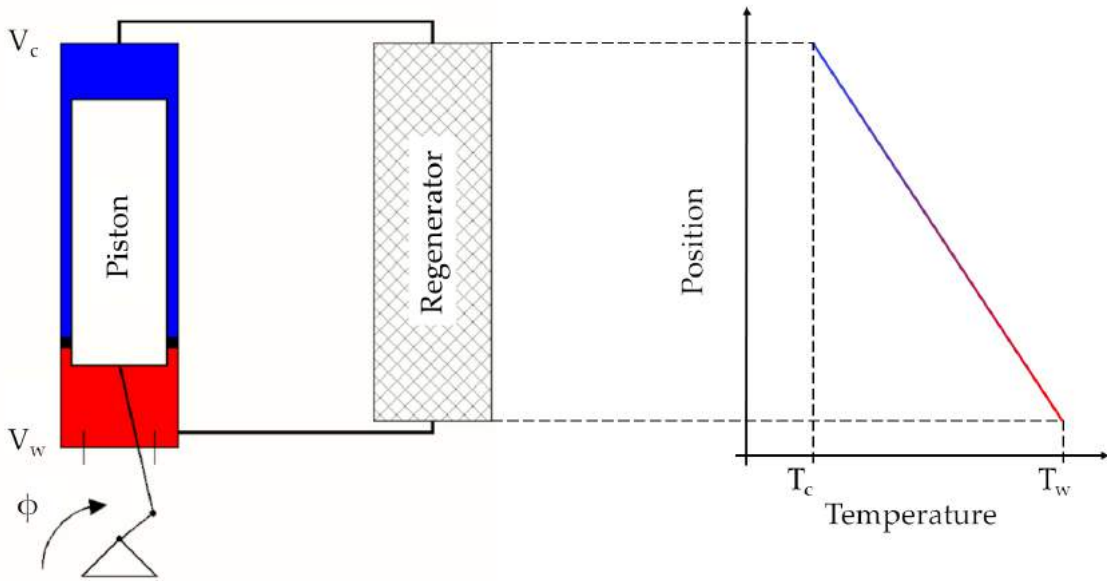


Figure 3.2: Principle of providing cooling power according to the Stirling-process based on [28]. The right side shows the idealized temperature distribution within the regenerator in the steady-state condition with the temperatures  $T_c$  and  $T_w$  of the cold and warm volumes  $V_c$  and  $V_w$ .

To begin describing the working principle of Gifford-McMahon (GM) cryocoolers or PTRs, it is important to acknowledge that the continuous provision of a temperature difference between the cold head and the ambience is enabled by a thermodynamic cycle within the cold head itself. Figure 3.2 is schematically displaying this basic principle. The periodic up and down movement of the piston changes the volumes of the warm and cold part ( $V_w$  and  $V_c$ ) according to the rotational angle  $\phi$  [29]. For the sake of accuracy, it shall be noted at this point that PTRs do not have a mechanical piston which will be further looked into in the following paragraphs. However, to introduce their working principle, Fig. 3.2 is suitable. The dependencies of the depicted  $V_w$  and  $V_c$  on  $\phi$  are stated in the following equation:

$$V_c = V_0 \cdot \frac{(1 + \cos\phi)}{2} \quad \text{and} \quad V_w = V_0 \cdot \frac{(1 - \cos\phi)}{2} \quad (3.1)$$



The entire working volume is  $V_0 = V_c + V_h$ . The piston movement forces the helium to flow through the regenerator where heat is transferred and stored temporarily in its matrix. In the isochoric system of Fig. 3.2 the pressure  $p$  changes periodically around a mean pressure  $p_m$  in the whole system [29].

$$p = p_m \cdot (1 - e \cdot \cos\phi) \quad (3.2)$$

The definition of factor  $e$  depends on the applied gas model. For an ideal gas, it calculates to  $e = \frac{T_w - T_c}{T_c - T_w}$ . Thus, if the piston moves downwards towards the warm volume, helium with high temperature is pushed through the regenerator to the cold volume. During this process, the helium releases a specific amount of heat to the matrix. The pressure  $p$  decreases according to Eq. 3.2 [30]. During the following upward movement of the piston, the described process is reversed. With the rotation frequency  $f$  of  $\phi$ , the provided cooling power at the cold volume can be calculated via a cyclic integral as shown in Eq. 3.3 since it is a closed-cycle process [29].

$$\dot{Q}_c = f \oint_0^{2\pi} p \, dV_c \quad (3.3)$$

When combining equations (3.1) and 3.2, this yields zero cooling power  $\dot{Q}_c = 0$  because  $V_c$  and  $p$  change antiphasically. Therefore, to achieve a non-zero cooling power, a phase shift between pressure and cold volume (respective piston position)  $\phi \neq 0, \pi$  has to be induced [29]. This is established variously in the different regenerative cooling processes ([31], [32] and [33]). Since the cryocooler used during this work was a Gifford-McMahon (GM) type PTR, in the following, exclusively the GM principle will be considered. In this type of cryocooler, instead of a piston, a continuously working compressor is used whose high pressure (HP) and low pressure (LP) line are connected to the same rotary valve. This valve's rotation causes a periodically changing connection of the cold head to either the HP or the LP side. This results in pressure waves in the cold head volume that are phase-shifted against the displacing piston shown in Fig. 3.2. In PTRs the mechanical displacing piston is replaced with an adiabatic gas piston [34]. This way, there are no moving mechanical parts inside the cold head. To control the effective phase shift between  $p$  and  $V_c$  in PTRs there are different principles in existence ([35], [31]). Cryomech's "PT420" PTR [36] uses passive phase shifting via an inertance tube with downstream helium reservoir at the warm end of the pulse tube. Using this principle, with single-stage PTRs currently 10.6 K can be reached at the cold end of the pulse tube [37]. In general, cryocoolers reach their minimal temperature  $T_{min}$  when the heat load on the cold part of the pulse tube is zero ( $\dot{Q}_c = 0$ ). This becomes obvious when considering Clausius expression  $dS = \frac{dQ_c}{T_0}$ . It yields that also in an ideal cryocooler, with a decreasing cold end temperature  $T_0$ , the Entropy generation in the cold head system due to  $\dot{Q}_c$  increases. This entropy increase must be depleted by dissipation of heat to the ambience ( $\dot{Q}_h$  at warm end of the pulse tube), since entropy depletion by adiabatic compression or expansion is impossible [38]. By applying the first law of thermodynamics to the system of the cold head, it can be observed that with a specific provided acoustic power  $P$  of the pressure oscillator,  $T_0$  reaches its lower

limit when  $\dot{Q}_c$  is zero. Lower temperature limits of about 2.3 K can be reached when adding another pulse tube and regenerator to create a two-stage cryocooler (e.g. [39]). The Helium entering the second stage is pre-cooled by the first stage system [35]. Another major advantage of adding a second stage to the process is that the surplus cooling power made available by the first stage can be used to thermally shield any applications connected to the colder second stage (as indicated in Fig. 3.1). Both variants can be seen in the following figure.

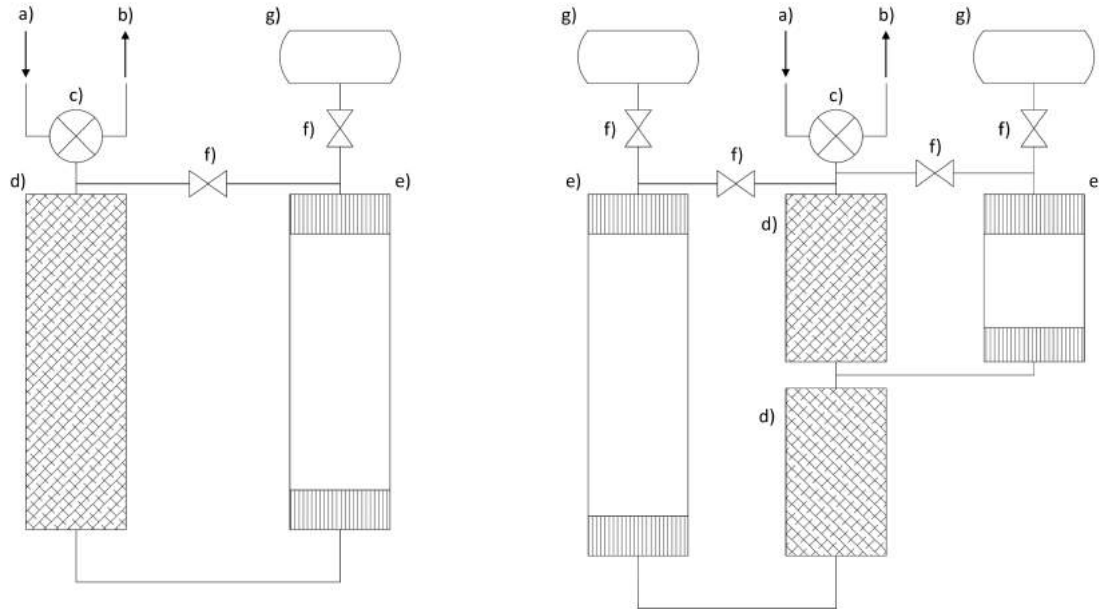


Figure 3.3: Left: Single-stage PTR; Right: Two-Stage PTR with pulse tubes connected in parallel

a) HP-line, b) LP-line, c) rotary valves, d) regenerators, e) pulse tubes with two heat exchangers each, one at the warm, one at the cold side, f) orifices, g) buffer volumes (own figure).

It is important to notice that with a parallel connection of the pulse tubes, the warm end of the second stage pulse tube can transfer heat to the environment as well [39]. This represents nowadays the base design of modern PTRs.

### Cryostats

The cooling capacities of cryocoolers in general can only be taken advantage of if the experimental instrumentation that is connected to the cold heat exchangers (see Fig. 3.3) is sufficiently thermally insulated against the environment to reduce the heat leaks contributing to the limited  $\dot{Q}_c$  and therefore decreasing the available cooling power for the experiment. These unwanted contributions are called "parasitic heat loads". To keep them at a minimum, cryostats are used, which refer to the housing of devices or fluids kept at very low temperatures, typically below 120 K. The general design of this work's cryostat can be taken from Fig. 3.1. Accordingly, the cryostat consisted of three major parts:

- a stainless steel vacuum vessel

- an actively cooled thermal shield at intermediate temperature
- superinsulation around the first and second stage parts of the PTRs cold finger.

The outer vacuum vessel allows vacuum pumping to  $10^{-7}$  mbar including cryopumping to reduce parasitic heat load via conduction through the residual gas. The thermal shield at an intermediate temperature level (in this work the PTRs first stage temperature) prevents the even colder second stage from being exposed to the thermal radiation by the inner vacuum vessel walls. The used superinsulation further reduces the heat loads to the respective stage. In total, the heat load on either of the cryocooler stages consists of five terms [29].

$$\dot{Q}_c(T_c) = \dot{Q}_{\text{rad}} + \dot{Q}_{\text{solid}} + \dot{Q}_{\text{cond}} + \dot{Q}_{\text{sorp}} + \dot{Q}_{\text{gas}} \quad (3.4)$$

These terms arise from thermal radiation  $\dot{Q}_{\text{rad}}$ , its conduction through solid bodies  $\dot{Q}_{\text{solid}}$ , condensation  $\dot{Q}_{\text{cond}}$ , cryosorption  $\dot{Q}_{\text{sorp}}$  [40] and heat conduction through the gaseous phase  $\dot{Q}_{\text{gas}}$ . In the following paragraphs, these terms shall be examined briefly in more detail.

When assuming that the cold surface ( $A_1, T_1$ ) is entirely surrounded by the warm surface ( $A_2, T_2$ ) and the respective bodies are grey bodies, the radiation term  $\dot{Q}_{\text{rad}}$  can be calculated using equation (3.5) [41].

$$\dot{Q}_{\text{rad}} = e_r \cdot A_1 \cdot \sigma \cdot (T_2^4 - T_1^4) \quad (3.5)$$

The factor  $e_r$  depends on the emissivity of both surfaces ( $e_1, e_2$ ) and both surface areas.

$$e_r = \left[ e_1^{-1} + A_1 \cdot \frac{(e_2^{-1} - 1)}{A_2} \right]^{-1} \quad (3.6)$$

The steady-state calculation of  $\dot{Q}_{\text{solid}}$  through a solid body is based on Fourier's law, which after integration yields [42]:

$$\dot{Q}_{\text{solid}} = \frac{A_c}{l} \cdot \int_{T_w}^{T_c} \lambda(\Theta) d\Theta \quad (3.7)$$

where  $A_c$  is the solids constant cross section area,  $l$  is its length and  $T_w, T_c$  the warm and cold temperature on either end.  $\Theta$  represents the temperature as an integration variable. This equation applies for a temperature-dependent thermal conductivity.

The term  $\dot{Q}_{\text{cond}}$  refers to the heat transferred via condensation of gas molecules on the cold surfaces. Calculation methods can e.g. be found in [42], however,  $\dot{Q}_{\text{cond}}$  is negligibly small against  $\dot{Q}_{\text{rad}}$  at pressures below  $10^{-5}$  mbar, which is given during

the experimental phase (see section 5.1). Furthermore, the same applies to the heat load due to cryo-adsorption  $\dot{Q}_{sorp}$  [29].

For this work's vessel size, at pressures below  $10^{-5}$  mbar, molecular flow conditions are given [29]. The number of impacts of a particle against walls is very large compared to impacts with other particles. The heat transferred to  $A_1$  is proportional to the residual pressure  $p$ . With the assumption of complete surrounding of  $A_1$  by  $A_2$  one obtains [29]:

$$\dot{Q}_{gas} = A_1 \cdot a \cdot K \cdot p \cdot (T_2 - T_1), \quad (3.8)$$

with

$$K = \left( \frac{R}{8\pi MT} \right), \quad (3.9)$$

and

$$a = \left[ a_1^{-1} + A_1 \cdot \frac{a_2^{-1} - 1}{A_2} \right]^{-1}. \quad (3.10)$$

The term  $T$  represents the temperature of the gas at the pressure  $p$ ,  $\kappa = \frac{c_p}{c_v}$  and  $a_i$  are the accommodation coefficients of the surfaces  $A_i$ .

### Multilayer Insulation

The superinsulation used in this work to reduce parasitic heat load on the first and second stage of the cryocooler was Multilayer Insulation (MLI). In general, superinsulations are composed of a number of highly reflecting layers that act as radiation shields and at the same time are barely in thermal contact with each other [29]. Layer by layer, an increasing part of the initial heat radiation is reflected and kept off the cold surfaces while in between, heat conduction is decreased by the thermally insulating spacer material. This principle is shown in Fig. 3.4.

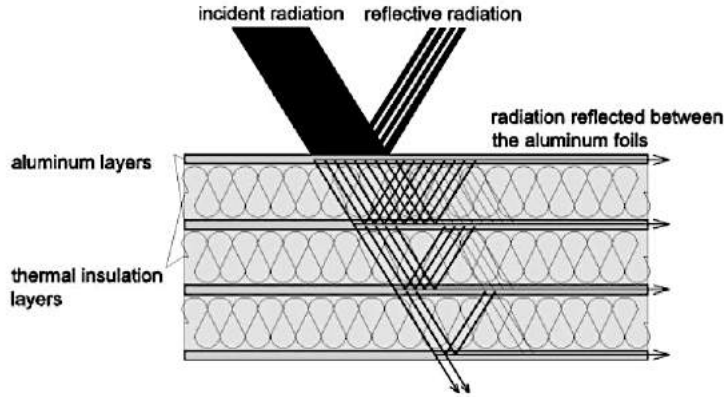


Figure 3.4: Principle draft of MLI's working principle [43]. The amount of reduced arrows represents the thermal radiation at each temperature level.

Specifically, the MLI used for the experiments consisted of two different layer components produced in blankets. The first were polyester films (6  $\mu\text{m}$  thickness each) with 400  $\text{\AA}$  of Aluminum deposited on each side. The films were perforated so that gas is allowed to flow through during vacuum pumping. The second component were thin nets of synthetic material to reduce the thermal contact. Between every 8 layers of aluminized polyester there was one layer of spacer. Thus, the polyester films acted as the thermal insulation layers (see Fig. 3.4) between the extremely thin aluminum depositions that shielded against heat radiation.

To approximate the parasitic heat flow (see Appendix E) through the used MLI according to equations 3.5 and 3.7, the data in Table 3.1 was used.

Table 3.1: Properties of aluminized mylar films for parasitic heat load approximation

Property	Unit	Value
$\lambda_{eff}$ at $10^{-5}$ mbar	$[\frac{\text{W}}{\text{m}\cdot\text{K}}]$	$4 \cdot 10^{-4}$
$e_{MLI}$ at 80 K	$[-]$	0.023

## 3.2 Finite Element Method

Numerous numerical simulation programs are based on the finite element method (FEM), which was also used during this thesis' work. It is a computational technique used to obtain approximate solutions of boundary value problems in engineering [44]. The approximations describe solutions to differential equation systems (e.g. consisting of Fourier's heat equation) that don't yield analytical results. Its most distinctive feature that separates it from other numerical methods is the division of a given domain (e.g. an aircraft wing) into a set of simple subdomains called *finite elements*. Any geometric volume that allows computation of the solution or its approximation or provides necessary relations among the values of the solution at those nodes of the subdomain qualifies as a finite element (commonly cuboids or tetrahedrons are used, see Fig. 3.5). This is a major

advantage over the method of finite differences which becomes unhandy to apply to non-cartesian grids. The elements connect all characteristic points (*nodes*) that lie on their circumference. The FEM emphasizes that the characteristics of the continuous domain may be estimated by assembling the similar properties of discretized elements per node. The node connections are established with ansatz functions that are specific for every element. This way, a system of interconnected ansatz functions is generated which allows a solution approximation of the global problem with detailed information distributed across the domain.

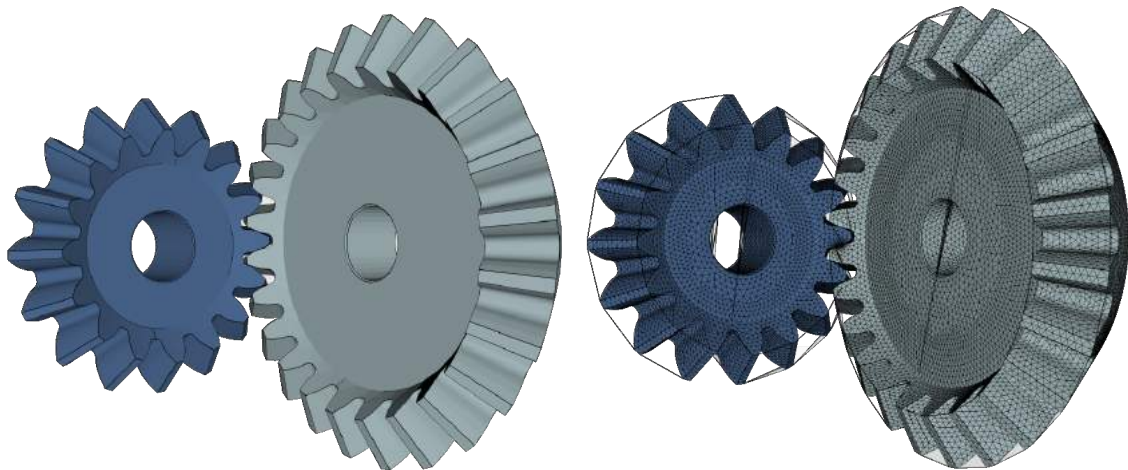


Figure 3.5: Non-uniform tetrahedral meshing (right) of three-dimensional gear models (left) [45]

The numerical solution process of engineering and mathematical physics problems via the FEM can be divided into four major steps [46]:

1. *Finite element discretization*: The collection of elements that makes up the domain is called the finite element mesh. The elements are connected to each other at points called nodes. When all elements are of the same geometry, the mesh is said to be uniform, otherwise it is called a nonuniform mesh. In any case it represents both, the geometry and solution of the problem. The mesh resolution plays an important role when simulation results need to be known in small spatial details as in the parasitic heat load estimation (see Appendix E).
2. *Element equations*: The physical behaviour of the elements themselves can be calculated rather easily due to their simple geometries. State quantities are calculated at the node positions. Ansatz functions are used to describe the interpolation between the nodes along the edges of the finite elements. The choice of ansatz functions does not only depend on the element shape but also on the global physical problem that is to be dealt with. Also, they need to fulfil certain continuity conditions between the nodes which depend on the physical problem as well.
3. *Assembly of element equations and solution*: Over every element, an approximation to the solution as a linear combination of nodal values and ansatz functions is sought. Via the nodes the solution information of one element is given to the adjacent ones for their respective solution calculation. Those

solutions are obtained in an iteration process. In general, however, the assemblage of finite elements is subjected to *boundary* and/or *initial conditions*. This important input also used during this thesis' work will be described in further detail in section 4.3.2. The discrete equations associated with the finite element mesh are solved only after the boundary and/or initial conditions have been imposed.

4. *Convergence and error estimate*: Each successive iteration results in a solution that moves progressively closer to the true solution if the numerical approximations *converge*. To iterate to a converged solution, ANSYS® in particular uses the Newton-Raphson method [47]. A detailed description can e.g. be found in [48]. Regarding the error, there are three sources in a finite element solution: (a) those due to the approximation of the domain, (b) those due to approximation of the solution and (c) those due to numerical computation (e.g. numerical integration and round-off errors in a computer). The estimation of these errors, however, is complex and can only be done under certain conditions for a given element and problem. Reddy [46] explains this more thoroughly.

### 3.3 Instrumentation

This work's experimental part included the planning and operating of a rather complex test setup (see section 4 and 5.1). In the following, background information will be given on the utilized measuring principles and the means of applying them within the setup.

#### 3.3.1 Joule Heating

Joule heating is named after James Prescott Joule who articulated what is now called *Joule's law*. It relates the amount of heat released from an electrical resistor to its resistance  $R_{el}$  and the current  $I$  that is passing through it [49]. Divided by time, Joule's law yields the heat flow  $\dot{Q}_J$  being emitted by the resistor:

$$\dot{Q}_J = I^2 \cdot R_{el} \quad (3.11)$$

This allows other formulations using Ohm's law [50] in which the applied voltage to the resistor  $U$  can come into play as well:

$$\dot{Q}_J = U \cdot I = \frac{U^2}{R_{el}} \quad (3.12)$$

This principle is used to mimic heat loads in the experimental system but also applies to the working principle of resistance thermometers (see below), which show a self-heating behaviour.

### 3.3.2 Resistance Thermometers

Resistance thermometers are based on the fact that the electrical resistance of a metal or metal oxide or carbon sample changes with temperature. Two different types of resistance thermometers were used in this work, which will be described in further detail in the following paragraphs.

#### Platinum Resistance Thermometers

The most reproducible type of sensor is made from platinum because it is an inert metal which can be drawn down to thin wires and deposited in thin layers but remains tough at the same time. Using very pure wires, thermometers can be manufactured with nearly the same electrical resistance characteristics. Furthermore, high reproducibility is obtained this way [51]. In this work's scope, thin film Pt100 platinum resistance thermometers were used, a sketch of which is depicted in Fig. 3.6.

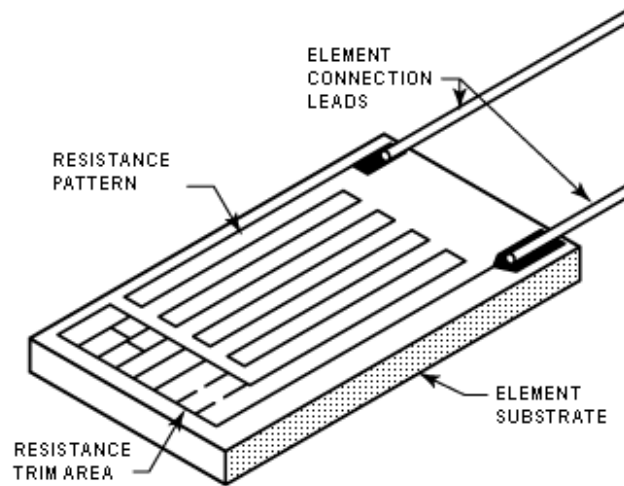
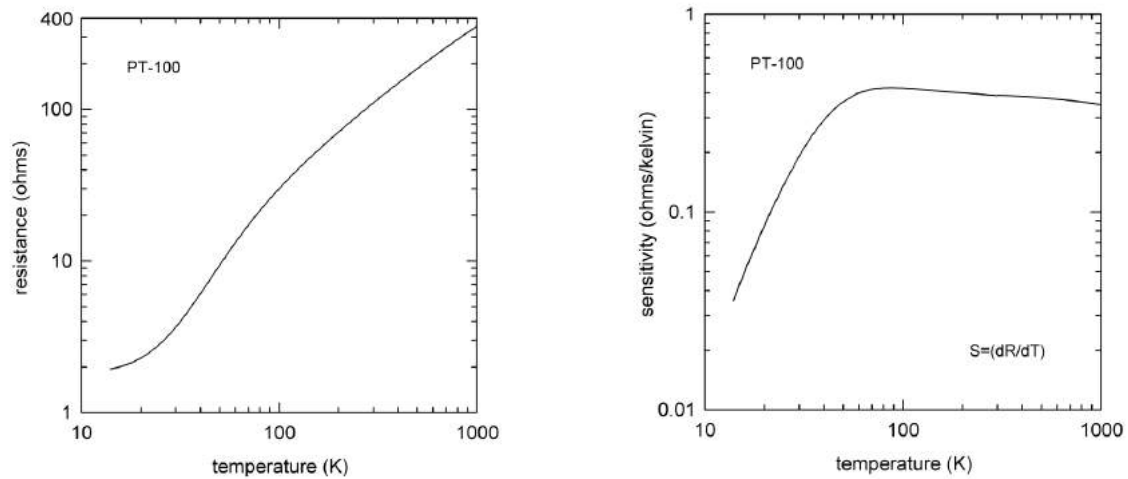


Figure 3.6: Sketch of a thin-film Pt100 sensor. Sensor variations with dimensions down to merely a few mm width and length are available [52].

The small dimensions of the thin film Pt100 heads generally allow for a convenient installation. Figure 3.7 shows both a typical resistance curve (a) and a typical sensitivity curve (b) for Pt100 sensors.





(a) Pt100 Resistance vs Temperature Curve

(b) Pt100 Sensitivity vs Temperature Curve

Figure 3.7: Typical Characteristics of Pt100 sensors [53].

As figure 3.7 highlights, the interchangeability applies to the temperature range between 70 K and 873 K [53] in which the sensitivity remains rather constant. In this temperature range, the resistance response data of Pt00 sensors is tabulated in the DIN IEC 751 standard. Since in this work, temperatures below 70 K had to be measured by the sensors, an in-house measured extension of the resistance curve was taken that describes the electrical resistance response down to 5 K. To improve the accuracy, a method based on the 2-point *SoftCal*<sup>TM</sup> procedure [54] was applied to every used Pt100 sensor. It makes small adjustments to the extended DIN IEC 751 resistance curve so that the resulting curve matches the resistance response characteristics of the individual sensor more closely. Detailed information can be found in Appendix C.

### Carbon Ceramic Thermometers

Below around 30 K, platinum resistance thermometers experience a rapidly decreasing sensitivity (see Fig. 3.7 (b)). Therefore, to measure temperatures on the PTR's second stage as low as 3 K, Carbon Ceramic Temperature Sensors (TVO sensors) were used. They offer an exponentially increasing sensitivity with decreasing temperature (see Fig. 3.8) and can be used at low temperatures, using the manufacturer's calibration data down to typically 1.5 K.

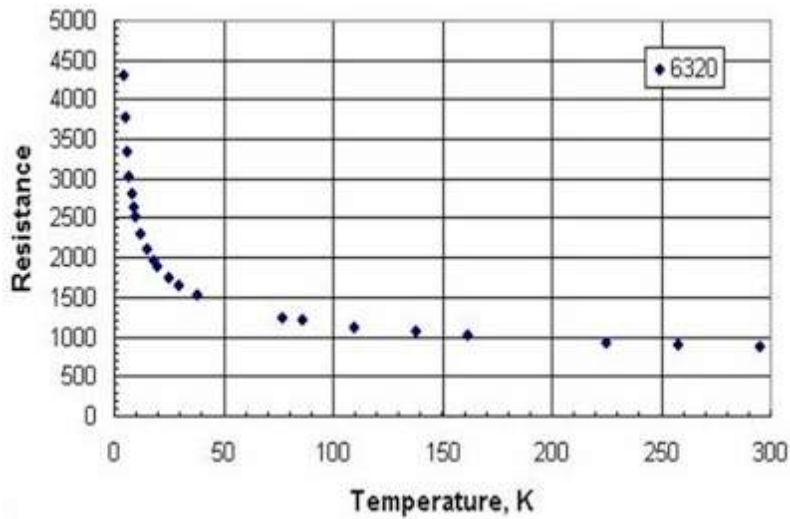


Figure 3.8: Resistance curve of a typical TVO sensor in Ohms (adapted from [55]).

The TVO sensors used in this work came along with a factory-set calibration curve that guaranteed errors in the order of a few mK for  $1.5 \text{ K} < T < 20 \text{ K}$ . Their approximate size and appearance can be seen in Fig. 3.8.

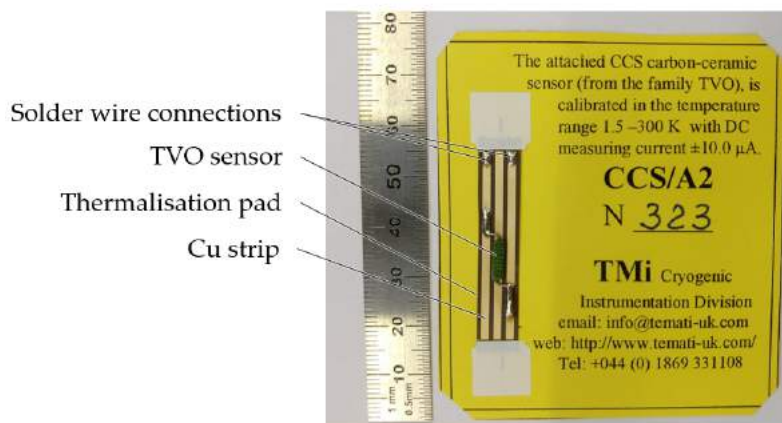


Figure 3.9: Representative photo for all used TVO sensors (own figure).

The TVO sensor itself consists of a carbon-ceramic matrix construction that allows for the opposite behaviour of platinum resistance thermometers (increasing sensitivity with decreasing temperature). The sensor itself sits on a thermally anchoring, yet electrically insulating Kapton sheet. On the sheet, thin copper strips are deposited to conduct the current. The sensor and the cables are connected to these via a soldered connection.

### 3.3.3 Heat Meters

In the context of this work, heat meters were used to determine heat flows (see section 5.1). The functional principle of heat meters is based on Fourier's law describing the dependence of heat flux  $\dot{q}$  on a temperature gradient  $\frac{\delta T}{\delta x}$  along the spatial coordinate  $x$  and the thermal conductivity  $\lambda$  [42]:

$$\dot{q} = -\lambda \cdot \frac{\delta T}{\delta x} \quad (3.13)$$

Thus, a measured temperature difference  $\Delta T$  over a length  $\Delta x$  of a body with the constant cross section  $A$  and a known thermal conductivity  $\lambda$  allows for a calculation of the heat flow  $\dot{Q}$  at the respective conditions. In this work's scope, this principle was taken a step further. *In-situ heat meter calibrations* were performed (see section 5.1) which shall be explained in further detail in the following paragraphs. According to Fourier's law, a heat flow  $\dot{Q}_i$  across a constant length  $\Delta x$  of a body causes a distinct temperature difference  $\Delta T_i$  along  $\Delta x$ . This provides the ability to approximate an unknown heat flow  $\dot{Q}_0$  across  $\Delta x$  by increasing the overall heat flow

$$\dot{Q} = \dot{Q}_0 + \dot{Q}_{add} \quad (3.14)$$

across the same distance and cross section  $A_c$  by a known  $\dot{Q}_{add}$ . The unknown  $\dot{Q}_0$  causes  $\Delta T_0$  whereas  $\dot{Q}$  causes  $\Delta T$ . With the integrated form of Fourier's law, this yields two equations:

$$\dot{Q}_0 = -\lambda_{eff,0} \cdot A_c \cdot \frac{\Delta T_0}{\Delta x} \quad (3.15)$$

and

$$\dot{Q} = -\lambda_{eff} \cdot A_c \cdot \frac{\Delta T}{\Delta x} \quad (3.16)$$

with the effective thermal conductivities  $\lambda_{eff,i}$  which are a result of the integration of the temperature-dependent thermal conductivities of the body analogous to the integral term in equation (3.7). Dividing equation (3.16) by (3.15) and solving for  $\Delta T$  yields

$$\Delta T = \frac{\lambda_{eff,0}}{\lambda_{eff}} \cdot \frac{\Delta T_0}{\dot{Q}_0} \cdot \dot{Q}. \quad (3.17)$$

This leads to the realization that since  $\Delta T_0$ ,  $\dot{Q}_0$  and  $\lambda_{eff,0}$  are constant values, when managing to also keep  $\lambda_{eff}$  constant when adding  $\dot{Q}_{add}$  during the temperature measurements, it is possible to approximate  $\Delta T$  as a function of  $\dot{Q}$  sufficiently well with a linear approach. This is displayed in Fig. 3.11.

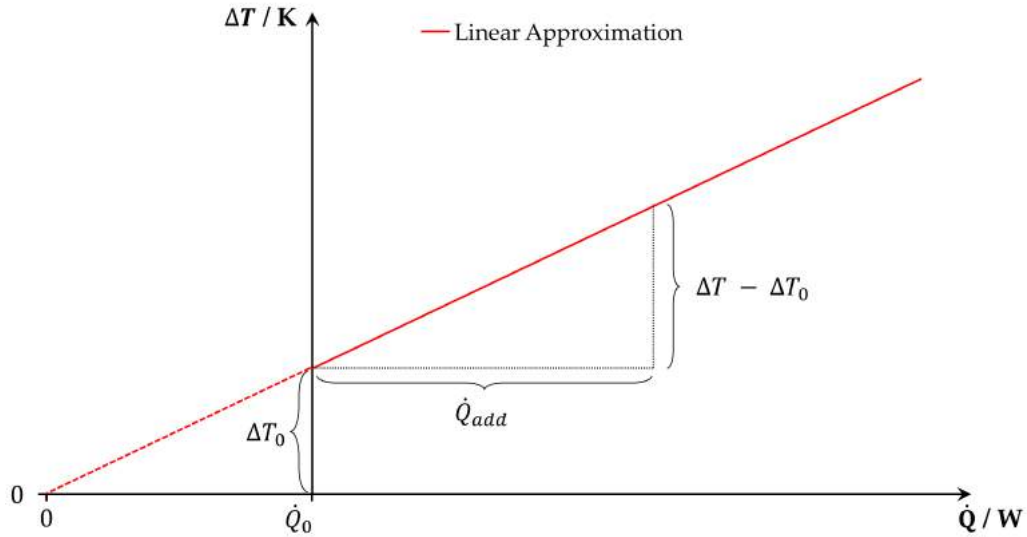


Figure 3.10: Principle depiction of unknown heat load determination via in-situ heat meter calibration (own figure).

After subsequently increasing the heat flow via  $\dot{Q}_{add}$  and measuring the respective  $\Delta T$ , one ends up with a straight line starting at the pre-existing  $\dot{Q}_0$  on the abscissa and  $\Delta T_0$  on the ordinate. To determine  $\dot{Q}_0$ , the abscissa origin has to be found. Considering the linear approximation, the straight line slope calculates to  $\frac{\Delta T - \Delta T_0}{\dot{Q}_{add}}$ . This yields for  $\dot{Q}_0$ :

$$\dot{Q}_0 = \frac{\Delta T_0 \cdot \dot{Q}_{add}}{\Delta T - \Delta T_0} \quad (3.18)$$

where  $\Delta T$  is the temperature difference caused by  $\dot{Q}_0 + \dot{Q}_{add}$ .

### 3.3.4 Four-Terminal Sensing

When measuring small electrical resistances (via voltage  $U$  and current  $I$ ), the parasitic resistances of electrical supply lines and electrical contacts can become significantly large in comparison to the resistance subject to measurement. To eliminate their influence, the four-terminal sensing principle can be applied.

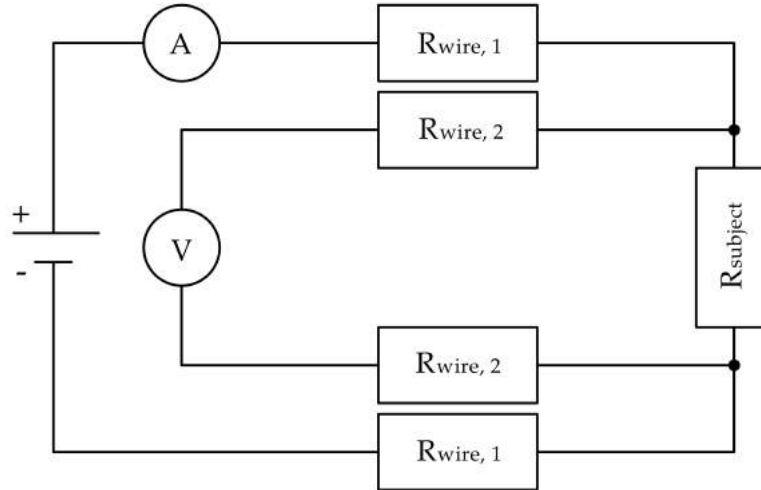


Figure 3.11: Four-terminal sensing wiring diagram for a single resistance to be measured ( $R_{\text{subject}}$ ). The Ammeter is connected to  $R_{\text{subject}}$  via current-providing wires with resistance  $R_{\text{wire},1}$  each. They can differ from the wires connected exclusively to measure the voltage drop across  $R_{\text{subject}}$  and thus may have a different resistance  $R_{\text{wire},2}$  (own figure).

The Voltmeter's wires carry miniscule current due to the inner electrical resistance of the voltmeter. Thus, even with long wiring until  $R_{\text{subject}}$  the resistances  $R_{\text{wire},2}$  will drop insignificant amounts of voltage. This results in a voltmeter indication that is very nearly the same as if it were connected directly across  $R_{\text{subject}}$ . Any voltage dropped across the main current-carrying wires will not be measured by the voltmeter and this way will not factor into the resistance calculation at all [56]. The current flowing through  $R_{\text{subject}}$  is measured in series by an ammeter. The wiring resistances  $R_{\text{wire},1}$  do not affect this measurement at all. With the negligibly falsified measurement values of  $U$  and  $I$ ,  $R_{\text{subject}}$  can be precisely calculated via Ohm's law.

### 3.3.5 Measurement Uncertainty Evaluation Methods

This work's determination method of uncertainties to a certain measurement and derived values follows the "Guide to the expression of uncertainty in measurement" (GUM) [1]. It describes well-recognized procedures to evaluate measurement uncertainties due to statistical errors. Systematic errors are not considered in this evaluation. The GUM defines a measurement as an estimation of the value to be determined ("true value"). Every measurement itself has a specific accuracy inside of which the observed measured value may take random values that scatter around the true value. Therefore, the GUM further argues that the deviations from the true value can be described by a Laplace-Gauss distribution. It is impossible to determine the true value but based on the distribution, a range of confidence can be given in which the true value can be found with a certain probability. There are two ways to express this: (a) The *standard uncertainty* which states the measurement result uncertainty expressed as a standard deviation and (b) the *combined standard uncertainty* which represents a measurement result's standard uncertainty "[...] when that result is obtained from the values of a number

of other quantities [...] [1]. The standard uncertainty  $s$  (see equations (3.19) and (3.20) respectively) states that with 68.27 % probability the true value lies within the respectively given boundaries. The standard uncertainty multiplied by three ("3s" or "3 $\sigma$ ") yields the boundaries covering a range that contains the true value with 99.73 % probability. The error bars and the upper and lower value limits stated throughout this work all represent 3s.

The GUM distinguishes between two types of uncertainty evaluations. *Type A* is a "method of evaluation of uncertainty by the statistical analysis of series of observations" [1] whereas *Type B* is merely defined as a method that uses other means than the statistical analysis of series of observations. All measurements carried out in the scope of this thesis can only be investigated by the procedure for Type B evaluations because they were not repeatedly conducted under the same circumstances. The Type B evaluation of standard uncertainty is based on scientific judgement of all of the available information on the possible variability of  $q$ . In compliance with the GUM, the information considered for this purpose in this work include the following:

- previous measurement data
- experience with or general knowledge of the behaviour and properties of relevant materials and instruments
- manufacturer's specifications
- data provided in calibrations and other certificates
- uncertainties assigned to reference data taken from handbooks

For further information on the used methods to determine  $s_B(\bar{q})$ , at this point shall be referred to [1] (paragraphs 4.3.3 to 4.3.6) in the following cases:

- the estimate  $\bar{q}$  is given and its quoted uncertainty is stated to be a particular multiple of a standard deviation
- the quoted uncertainty of  $\bar{q}$  defines an interval having a 90, 95, or 99 percent level of confidence
- an interval is given in which  $q$  lies within with a 50 % chance
- an interval is given in which  $q$  lies within with a 67 % chance

It is important to note here that due to the nomenclature in the GUM,  $q$  exclusively refers to a generic measured quantity in the context of uncertainty calculations. Elsewhere in this work, it represents heat flux. In other cases, it was possible to state limits for  $q$  according to the accuracy data given by the manufacturers ( $a_+$  and  $a_-$ ) in which  $q$  lies with a probability equal to one (essentially zero probability of  $q$  lying outside of those bounds). Additionally, there was no specific knowledge about the possible values of  $q$  within the limits. In this case, according to [1] it is to be assumed that it is equally probable for  $q$  to lie anywhere within that interval. Then,  $s_B(\bar{q})$  is defined as

$$s_B(\bar{q}) = \frac{a_+ - a_-}{\sqrt{12}} . \quad (3.19)$$

This assumes a symmetrical rectangular distribution of possible values around  $\bar{q}$ . However, it remains to be the simplest approximation of  $s_B(\bar{q})$  even if  $q$  cannot be assumed to be symmetric with respect to its best estimate  $\bar{q}$  if there is not enough information available to choose an appropriate distribution [1].

Often, the final value to be determined is a function of several quantities  $Y = f(X_1, X_2, \dots, X_N)$ . In case the input quantities  $X_i$  each have a standard uncertainty  $s(\bar{X}_i)$  as well, the uncertainty propagation of each of these input quantities has to be considered. With input quantities that are independent from each other, the *combined standard uncertainty*  $s_c(\bar{Y})$  of the best estimate  $\bar{Y}$  can be calculated according to [1], paragraph 5.1:

$$s_c(\bar{Y}) = \sqrt{\sum_{i=1}^N \left( \frac{\delta f}{\delta X_i} \right)^2 \cdot s^2(\bar{X}_i)} \quad (3.20)$$

## 4 Test Setup Development

This section will deal with the test stand design determination. It consists of three major stages whose dependencies and chronological order is visualized in the following scheme.

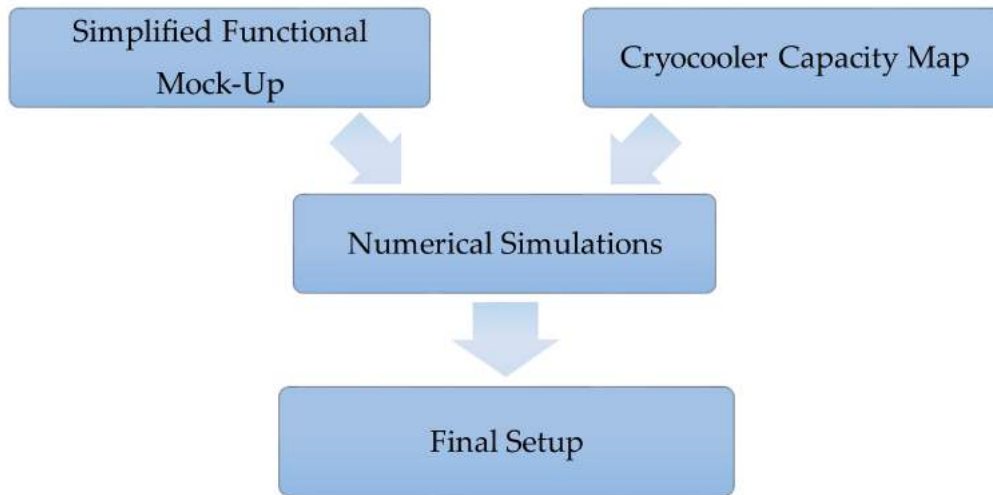


Figure 4.1: This work's test setup development process visualization (own figure). The arrows represent both content dependencies and chronological sequence.

As mentioned in the objective (section 2), the first goal was to develop a test setup with the largest Cryogel<sup>®</sup>Z sample cross section possible while still providing a homogeneous intermediate temperature level of 40 K to 80 K and a low temperature level of 5 K maximum. Naturally, it was essential to first establish a mock-up model that generally offered the functionality of conducting the heat load measurements through the Cryogel Z at these low temperatures while at the same time compressing it with a force equivalent to 1 bar mechanical pressure. This served as the base design of the numerical simulations. The limitation regarding the Cryogel Z sample cross section, however, was introduced by the finite cryocooler cooling capacities. Thus, a detailed capacity map of the cryocooler had to be determined before this limitation could be established within the numerical simulation process. At the end of this process, an approximate maximum Cryogel Z cross section could be determined, which finally made the development of a detailed test setup model possible that allowed commissioning, manufacturing and installation of a real experimental setup.

### 4.1 Mechanical Pressure Application on Cryogel<sup>®</sup>Z

Taking into account the necessity of two different temperature levels that the Cryogel<sup>®</sup>Z needs to be in contact with, the general idea for the setup design was to create a thermally symmetrical setup whose center consists of the low-temperature stage. The Cryogel Z is compressed inside the cryostat against the two different temperature levels (established by large wafers thermally linked to



the PTR heat exchangers) by moving the top panel of the cryostat itself towards the bottom panel with the Cryogel Z layers in between. This also allows for a good thermal contact between the Cryogel Z and the wafers and cryostat panels. The compression principle is presented in the following sketch in Fig. 4.2.

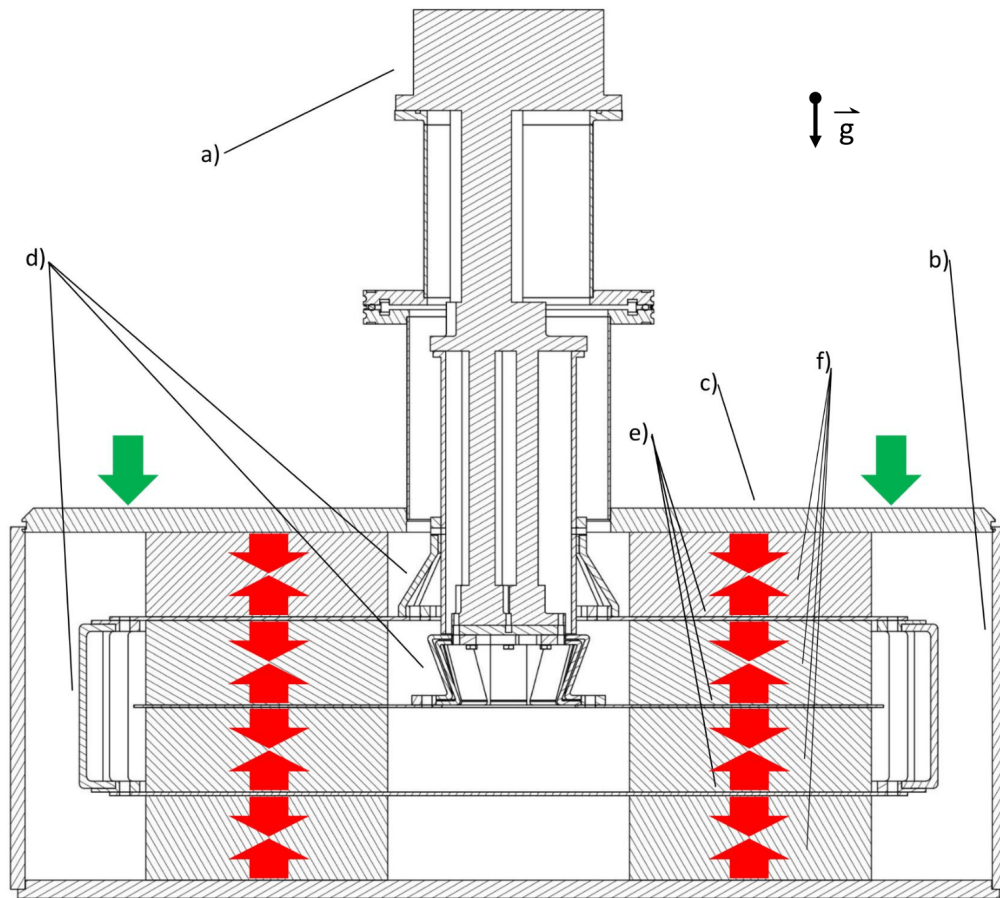


Figure 4.2: Compression principle of Cryogel Z inside the cryostat (own figure). a) cryocooler cold head, b) cryostat wall, c) cryostat top panel, d) flexible thermal links, e) thermalized copper wafers, f) donut-shaped stacks of Cryogel<sup>®</sup> Z. The forced downwards movement of the cryostat's top panel causes the mechanical pressure on the stacks of Cryogel Z in between the cryostat panels and the wafers linked to the first and second stage PTR heat exchangers.

The thermal symmetry was accomplished by placing not one but two first-stage-temperature wafers, one above and one below the center wafer that was linked to the second stage PTR heat exchanger. These two wafers were thermally linked around their circumference, to achieve a homogeneous temperature distribution. This way, the center wafer was thermally insulated symmetrically in vertical direction to the ambience. Around the inner and outer circumference of wafers and Cryogel Z stacks, the application of MLI was planned to minimize parasitic heat load (see section 3.1). In order to allow for the dilatation of the Cryogel Z during compression, a solution for flexible thermal links between the PTR heat exchangers and the wafers in contact with the Cryogel Z had to be found (see section 4.4). It is important to note at this point that the low temperatures to be expected during the experiments make the presence of a high vacuum inside

the cryostat essential (to minimize  $\dot{Q}_{cond}$  and  $\dot{Q}_{gas}$ , see section 3.1). Additionally, due to the necessity for thermal links on the inside and outside of the temperature level-supplying wafers and thermal insulation against the vessel walls, it is inevitable that the cross section of the Cryogel Z stacks  $A_{CG}$  is smaller than the cryostat top/bottom panel surface area  $A_{panel}$ . These two facts lead to the realization that the 1 bar compression of the Cryogel K cannot be provided simply by the difference between the atmospheric pressure  $p_{atm}$  outside and the vacuum inside the cryostat. This way, the mechanical pressure on the Cryogel Z  $p_{CG}$  would be

$$p_{CG} = (p_{atm} - p_{vac}) \cdot \frac{A_{panel}}{A_{CG}} \quad (4.1)$$

with the remaining low pressure inside the vacuum  $p_{vac}$  and  $\frac{A_{panel}}{A_{CG}} > 1$ . This issue can be resolved, however, by calculating the necessary  $p_{vac}$  to obtain  $p_{CG} = 1$  bar. With this knowledge, to compress the Cryogel Z prior to the experiments, in a first step the pressure inside the cryostat could be lowered successively until the calculated intermediate  $p_{vac}$  was reached. Thus in this state, the Cryogel Z was compressed by 1 bar mechanical pressure after letting the top panel move downwards into the cryostat due to the induced pressure difference. After reaching force equilibrium, the top panel could be locked in its position before further lowering of  $p_{vac}$  by vacuum pumping. This method requires that the Cryogel Z's spring force remains constant with lower temperatures and pressures to avoid change of the residual mechanical pressure on it after the panel fixation. The in-house measured relation between applied mechanical pressure and physical dilatation of Cryogel Z at different conditions were evaluated to confirm this. Results are shown in Fig. 4.3.

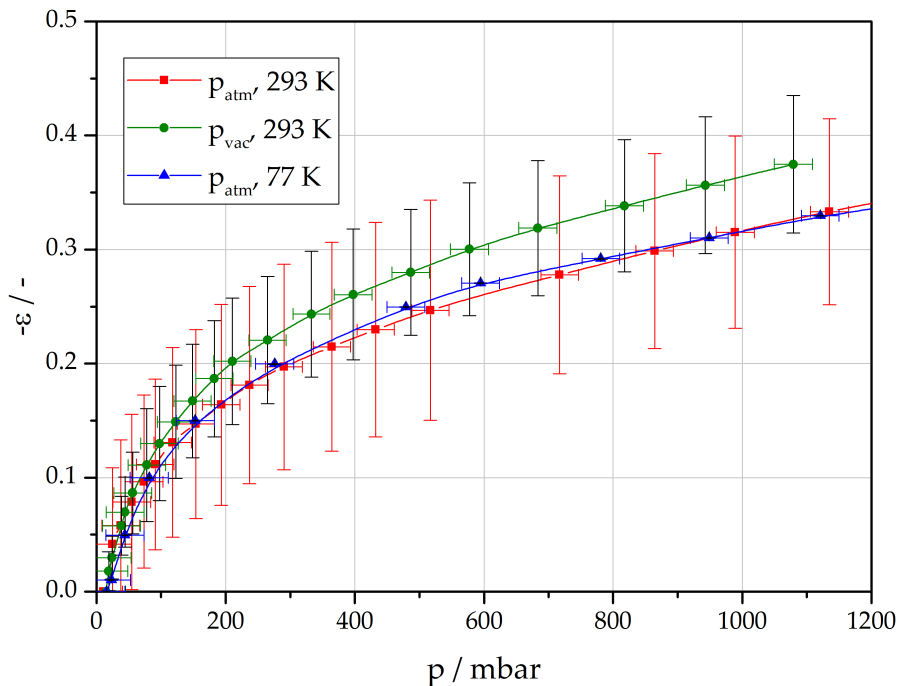


Figure 4.3: Comparison of in-house measurement data on the dilatation  $\epsilon = \frac{\Delta l}{l_0}$  of Cryogel<sup>®</sup>Z under compression at different conditions. Only the measurements at ambient temperature were repeated. Thus, the significantly larger error bars for these conditions reveal the domination of systematic errors due to the inhomogeneous structure of the Cryogel Z-fabric across the blanket (see section 1.2.2) which impedes precise measurements.

Following the curves of the best guesses for all three different conditions, it becomes clear that merely vacuum pressures have a small influence on the spring force of the Cryogel Z. It decreases slightly with lower pressures. For the described pressure application method shown in Fig. 4.2, however, this effect was expected to become insignificantly small due to the established intermediate vacuum pressure before locking the cryostat panel in its final position. Furthermore, the large uncertainties have to be taken into account that further reduce the meaningfulness of the hinted spring force difference at vacuum.

## 4.2 Cryocooler Capacity Determination

As shown in section 3.1, the cooling capacities of cryocooler stages depend on the temperature they are provided at. Thus, for a two-stage cryocooler like the PT420<sup>®</sup> used in this work, it is common procedure to illustrate the cooling capacities of both stages in a *capacity map*. As an example, Fig. B.1 in Appendix B shows the PT420<sup>®</sup>'s capacity map distributed by the manufacturer Cryomech<sup>®</sup>Inc..

This capacity map, however, lacks detail in the covered temperature range and does not give away any information on the cryocooler performances up to the

temperatures of interest for this work (around 5 K on the 2<sup>nd</sup> and 80 K on the 1<sup>st</sup> stage heat exchanger (HX)). Both data are important for the numerical simulations described in section 4.3 and the experimental methodology itself (see section 5). Thus, in an experimental setup provided by the Central Cryogenic Laboratory at CERN provided to this end, a more detailed and more widely-ranged capacity map was experimentally determined. The respective test stand and measurement process are described in the following sections.

#### 4.2.1 Measurement Setup and Methodology

The experimental setup for the Cryomech<sup>®</sup>PT420 capacity map determination is drafted in Fig. 4.4.

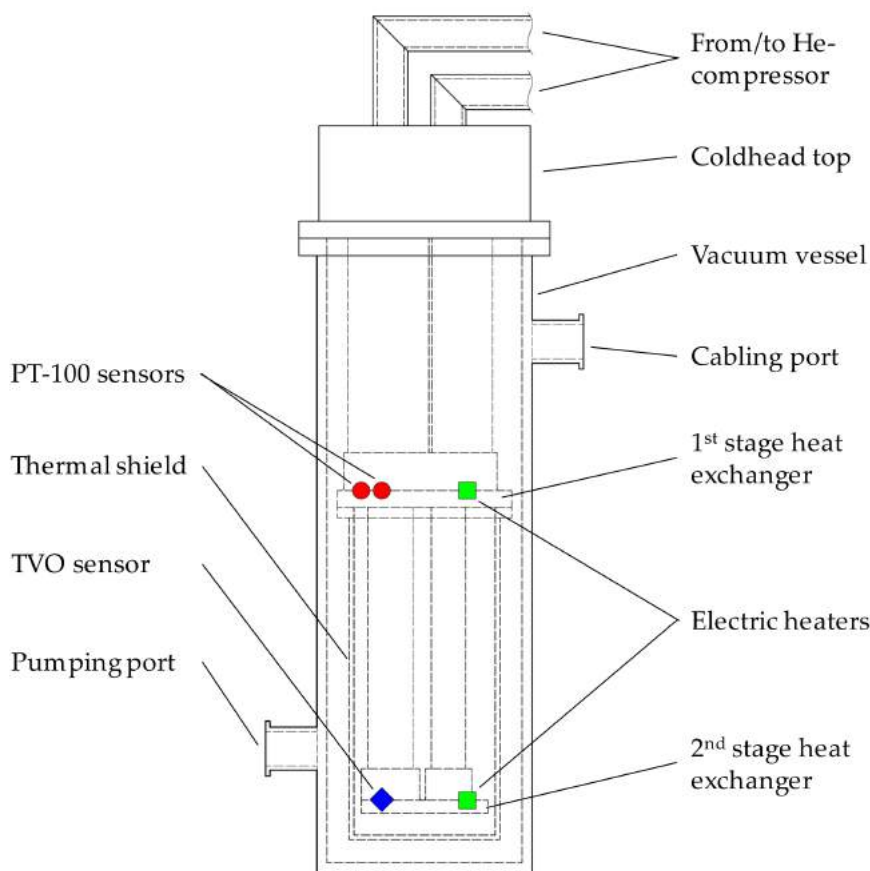


Figure 4.4: Sketch of the cryocooler capacity measurement test stand (own figure). The MLI insulation around the second stage heat exchanger and around the thermal shield is not shown. On both PTR heat exchangers, resistors were installed to allow for Joule heating (see section 3.3.1). Temperatures were measured with two redundant Pt100 sensors on the first stage and a TVO sensor on the second stage.

The general measurement principle to achieve one point in the capacity map was to induce known heat flows on both PTR stages via the electric heaters installed directly on the respective heat exchangers and record the resulting stage temperatures in thermodynamic equilibrium via the resistance thermometers. As heaters one 100  $\Omega$  resistor was used on the 1<sup>st</sup> stage and two 100  $\Omega$  resistors connected

in series (depicted as one single heater in Fig. 4.4) were used on the 2<sup>nd</sup> stage. All measurement devices were connected according to the four-terminal-sensing scheme in Fig. 3.11. The Pt100 and TVO sensors were connected to Lakeshore<sup>®</sup>120 current sources that induced a 1 mA current through the Pt100s and a 10  $\mu$ A current through the TVO sensor. By determination of the respective voltage drop through the sensors, their resistance could be calculated and converted into a temperature value using resistance curves as in Fig. 3.7 and 3.8. As an ammeter for the first PTR stage, to more precisely record the current through the heaters, a Keithley<sup>®</sup>2001 multimeter was used. An R&S<sup>®</sup>HM8143 and an SM 70-22 (manufactured by Delta Elektronika<sup>®</sup>) served as respective DC power supplies to adjust the heat loads according to equation (3.12). With the R&S<sup>®</sup>HM8143 also the current through the second stage heater was measured. All voltages were centrally recorded via a multiplexer switch module connected to a PXI-4071 Multimeter (National Instruments<sup>®</sup>) which allowed the direct display of all converted temperature values simultaneously in LabVIEW<sup>®</sup> on the connected computer.

Before turning on the PTR to cool down both stages to begin the measurements, vacuum had to be pumped inside the cryostat to avoid gas condensation on the cold surfaces of the PTR and thus to minimize  $\dot{Q}_{cond}$  but also  $\dot{Q}_{gas}$  of the parasitic heat load (see section 3.1). To be able to pump the gas inside the thermal shield, it had a perforated bottom. Using an ALCATEL<sup>®</sup>5081 turbomolecular pump backed by an ALCATEL<sup>®</sup>2012A rotary vane vacuum pump, a pressure of  $8 \cdot 10^{-5}$  mbar was reached. Before the next step, the cryocooler was turned on. Without powering the heaters ("zero-load"), the first measured point represented the lowest reachable temperatures on both PTR stages (see section 3.1). The respective temperatures were measured in thermodynamic equilibrium the criterion of which was a mean temperature change of less than  $0.02 \frac{K}{h}$ . The zero-load point was expected to not be of significance. This was due to the fact that it could by nature of the experimental setup according to Fig. 4.2 not be reached because the heat load through the Cryogel<sup>®</sup> to the stages was intrinsic to the setup and subject of measurement (see section 2). In fact, preliminary numerical simulation results using approximated geometries (section 4.3) showed that, without additional heating, heat loads in the order of 70 W on the first and 1.5 W on the second stage had to be expected exclusively by heat conduction through the compressed Cryogel Z.

Thus, measuring the capacity map points was started at around 75 W on the first stage and around 1.5 W on the second stage. The heat load on the first stage was successively increased in steps of 5 W until reaching almost 100 W before the heat load level on the second stage was raised by 0.5 W and the same heat loads were induced to the first stage again. This was done until reaching 4.5 W on the second and 98 W on the first stage which represented the voltage supply limit of the SM 70-22<sup>®</sup> power supply.

### 4.2.2 Cryocooler Performance

The measurements described in section 4.2.1 led to the determination of the capacity map depicted in Fig. 4.5.

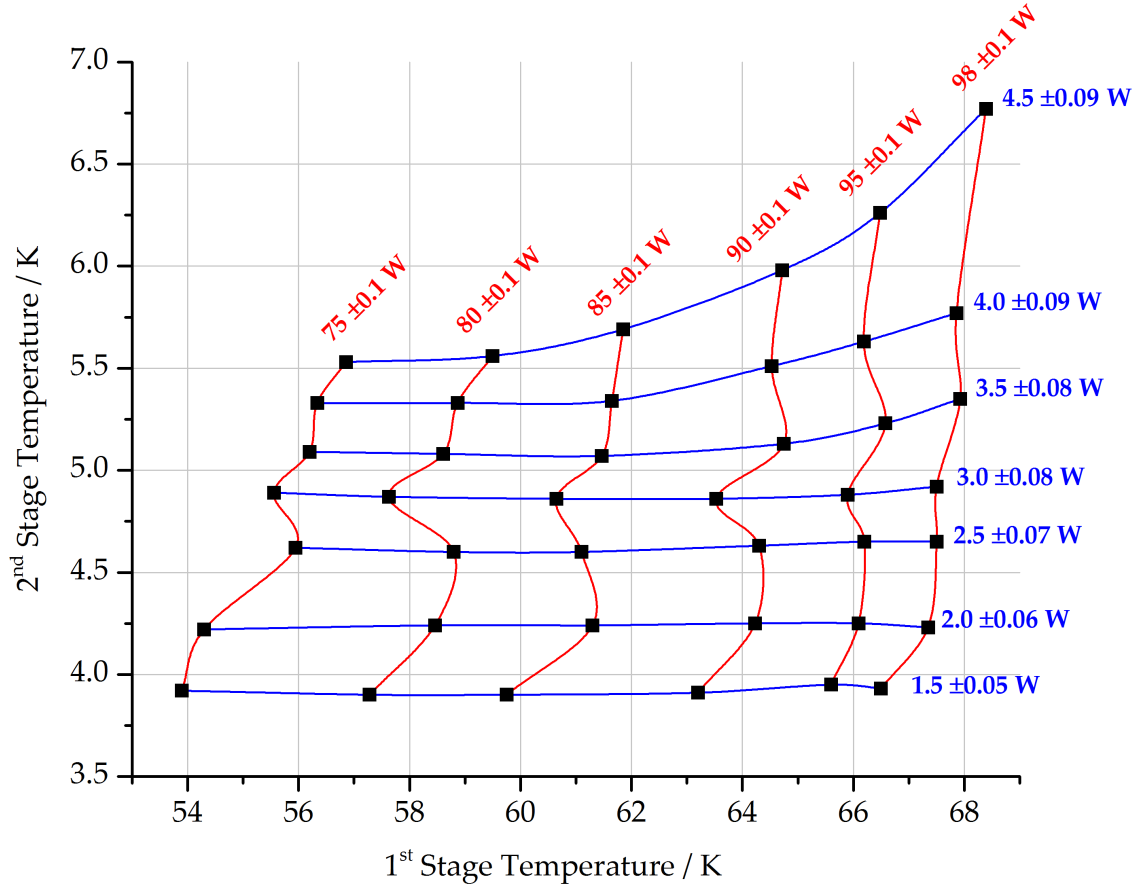


Figure 4.5: Capacity map of this work’s Cryomech®PT420 PTR (own figure). Top/right: 1<sup>st</sup> and 2<sup>nd</sup> stage cooling capacity respectively. For the sake of clarity, the errors which were in the order of  $\pm 0.75$  K for the first stage temperature measurements and  $\pm 0.015$  K for the second stage are not depicted. An exemplary error calculation for the applied heat loads and temperatures can be found in Appendix D. For all tabulated values, please see Appendix F.

Fig. 4.5 shows that in general the first and second stage cold head temperatures rise with applied heat load. This matches the insight described in section 3.1 which states that  $\dot{Q}_c$  decreases with  $T_0$ . Secondly, at second stage heat loads up to 3 W, the heat loads applied to the first stage hardly influence the lower second stage temperature limit. The volume work capacity ( $p dV_c$ , see equation 3.3) to provide for the increasing  $\dot{Q}_c$  of the first stage is still sufficient to pre-cool the helium entering the second stage pulse tube to a constant temperature. This is not given anymore at higher loads applied to the second stages. The second stage exceeds the required volume work capacity to compensate for the rising  $\dot{Q}_c$  at a constant  $T_0$ . The result is that the second stage cold head temperature disproportionately increases with the first stage heat load. Lastly, it is important to note the PT420®’s behaviour at a load of 3 W on the second stage. The first stage’s low tem-

perature level at this load is lower than with 2.5 W load. This indicates the *sweet spot* of this PTR where the internal pressure distribution happens to be ideal and the volume work on the first stage is reflected more efficiently in the provided  $\dot{Q}_c$  so that a lower  $T_0$  is possible. Since each cooler is packed with regenerator material by hand and variations of the helium pressure in the hoses between the cold head and the compressor affect the cooler operating performance on both stages, each cryocooler has its own sweet spot [57].

### 4.3 Numerical Simulations

In this section, this work's numerical simulations in ANSYS® will be explained in further detail. They were used to create and evaluate the thermodynamic design of the experimental setup in section 4.4. As mentioned in section 4.2.1, they also served to narrow down the range of interest regarding cooling power on both stages for the PT420® capacity map determination using a preliminary geometry.

#### 4.3.1 Model Geometry

As mentioned in section 2, the cryostat vacuum vessel was supplied by the client, the dimensions of which already set preliminary restrictions on the maximum outer diameter of the Cryogel®Z blanket stacks depicted for example in Fig. 4.2 and the maximum overall Cryogel Z stack height after compression. To obtain an ideally symmetric geometry of the cryostat interior in vertical direction while still allowing a vacuum sealing of the top panel after compression, stacks of 7 layers of Cryogel Z were chosen for each vertical location:

1. between cryostat top panel and upper copper wafer flexibly thermally linked to the 1<sup>st</sup> stage HX ("upper 1<sup>st</sup> stage wafer"),
2. between the upper 1<sup>st</sup> stage wafer and the copper wafer flexibly thermally linked to the 2<sup>nd</sup> stage HX ("2<sup>nd</sup> stage wafer"),
3. between the 2<sup>nd</sup> stage wafer and the lower 1<sup>st</sup> stage wafer flexibly thermally linked to the upper wafer,
4. between the lower 1<sup>st</sup> stage wafer and the cryostat bottom panel.

Without the wafers in between, these stacks of 28 Cryogel Z layers in total accounted for a height of 280 mm before compression inside the cryostat vessel, which had an inside wall height of 292.5 mm without considering the top panel thickness of 20 mm. To create appropriate model geometries, the resulting stack heights after compression in the experimental state had to be determined. In order to do this, the data from Fig. 4.3 was used, which yielded a mean dilatation of  $\epsilon = -0.324$  when considering the curves from all three different experimental conditions. This meant that in compressed state, each Cryogel stack was expected to have a remaining height of 47 mm (rounded value) from initially 70 mm.

With the given information about the maximum Cryogel Z stack heights and the range of respective maximum outer diameter still fitting inside the vacuum vessel, simplified model geometries were created for use in ANSYS®. For this, the

ANSYS®-internal Design Modeler® and Autodesk Inventor®2016 were used.

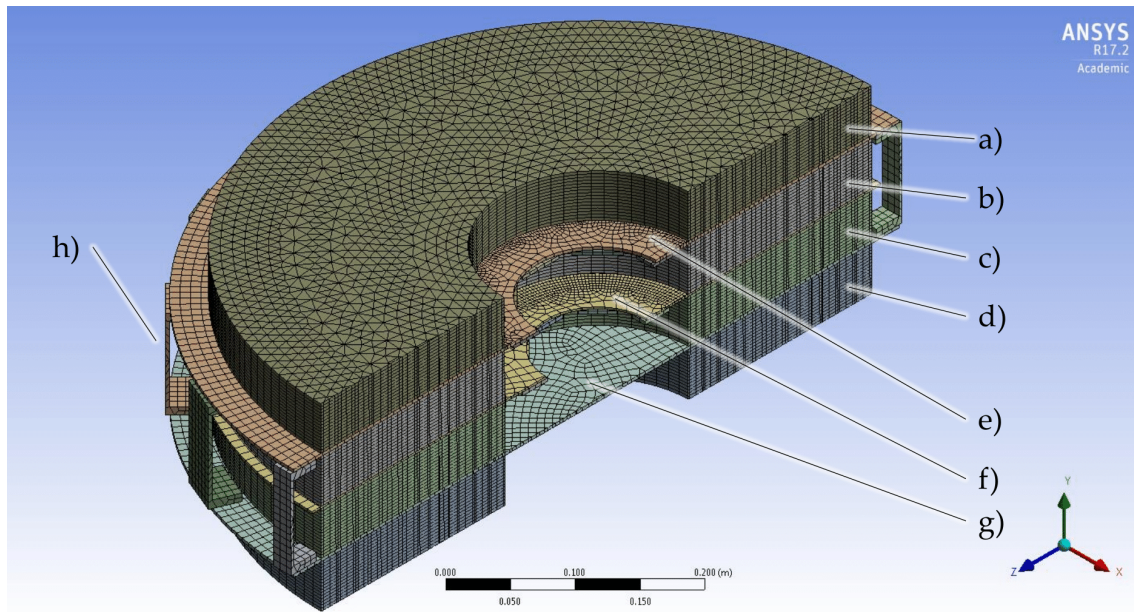


Figure 4.6: Sectional view of the model geometry of the experimental space inside the vacuum vessel with non-uniform meshing (see section 3.2). a) to d): Cryogel®Z stacks 1. to 4. (see above), e) upper 1<sup>st</sup> stage wafer, f) 2<sup>nd</sup> stage wafer, g) lower 1<sup>st</sup> stage wafer, h) flexible thermal links (own figure). The end of the thermal links to both of the PTRs heat exchangers are attached to the bottom of e) and f) towards their center.

A similar geometry to the one depicted in Fig. 4.6 was used for the preliminary estimation of heat loads on both cryocooler stages for a sensible capacity map determination (see section 4.2). The Cryogel Z stack cross sections, adjustable by changing the outer diameter, had to be roughly estimated in this stage before having more precise knowledge about the PT420®'s performance. After its determination, more detailed predictions could be made about heat loads on the PTR stages and resulting temperatures on the wafers (see Fig. 4.6 e) and f)).

In order to allow for this, a second geometry (see Fig. 4.7) had to be created to consider the upper part of the thermal links to the first stage. As Fig. 4.2 shows, the upper 1<sup>st</sup> stage wafer was planned to be thermally linked to the first stage HX via flexible links attached to a rigid thermal shield around the second stage pulse tube and regenerator. All mentioned parts will be described in further detail in section 4.4.



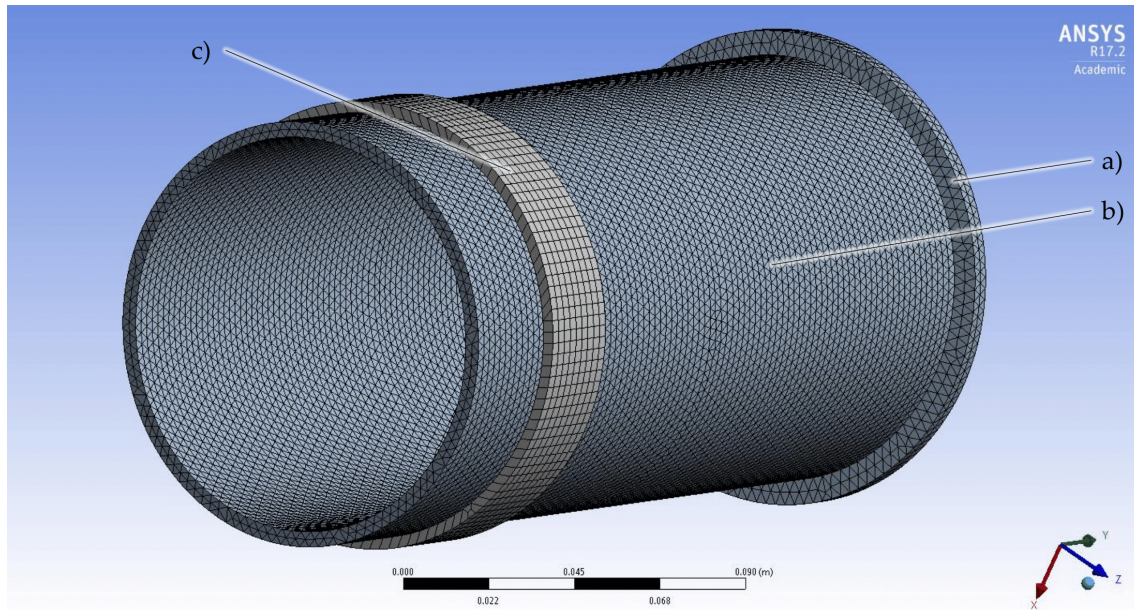


Figure 4.7: Sectional view of the model geometry of the thermal shield connected to the PT420<sup>®</sup>'s first stage HX (own figure). a) mounting flange to bolt to the heat exchanger, b) shield with 4 mm thickness, c) ring for attachment of flexible thermal links.

The use of two separate geometries was chosen over a merged large domain to facilitate alternations of single parts like the thermal links, whose designs underwent several iterations themselves or the Cryogel Z stack diameters without having to adjust the whole model accordingly. Also, the separation into two domains allowed faster simulation runs when merely the independent behaviour of one of the parts was to be examined qualitatively in further detail. Examples are temperature rises along the thermal shield, the influence of the shape of the thermal link ends and the influence of bolts on temperature distributions. It was accepted in this context that, for specific investigations calling for an interaction between both geometries, simulations had to be iterated (see section 4.3.2). The geometric modelling of the vacuum vessel, the cryocooler itself and the MLI insulation was refrained due to simplicity reasons.

### 4.3.2 Defined Model Setup Conditions

In this section, all parameters used to allow for adequate thermodynamic numerical simulation will be described.

#### Material Properties

For the thermal link, wafers and the thermal shield material, oxygen-free high thermal conductivity (OFHC) copper with RRR = 100 was chosen due to its low outgassing rates in vacuum and advantageously high thermal conductivity at the temperature range of interest regarding both PTR stages. Another advantage is that it can relatively easily be subjected to heat treatment and soldering which

was an important factor in the manufacturing process of specific parts (see section 4.4). The only other material occurring in the modelled parts was Cryogel Z<sup>®</sup>. In the scope of this work, exclusively steady-state thermal analyses were conducted. Thus, there was no need for supply of density and specific heat data for either of the two materials. A curve of the used temperature-dependent thermal conductivity data for the Cryogel Z in compressed state ( $\epsilon = -0.324$ ) can be found in Fig. 1.7. This thermal conductivity was measured prior to this thesis' work at the same compression. The thermal conductivity data for OFHC copper with RRR = 100 was taken from [58]. Values for both materials can be found in Appendix A.

## Boundary Conditions

The following kinds of boundary conditions (see section 3.2) were applied throughout all numerical simulations conducted in this work to surfaces of the meshed geometries:

1. *Dirichlet*: homogeneous temperature distributions,
2. *Neumann*: heat fluxes.

At all interfaces between bodies, thermal contact was defined. The thermal conductance determination is described in the following paragraph. An exemplary model view of where the boundary conditions were applied can be seen in Fig. 4.8.

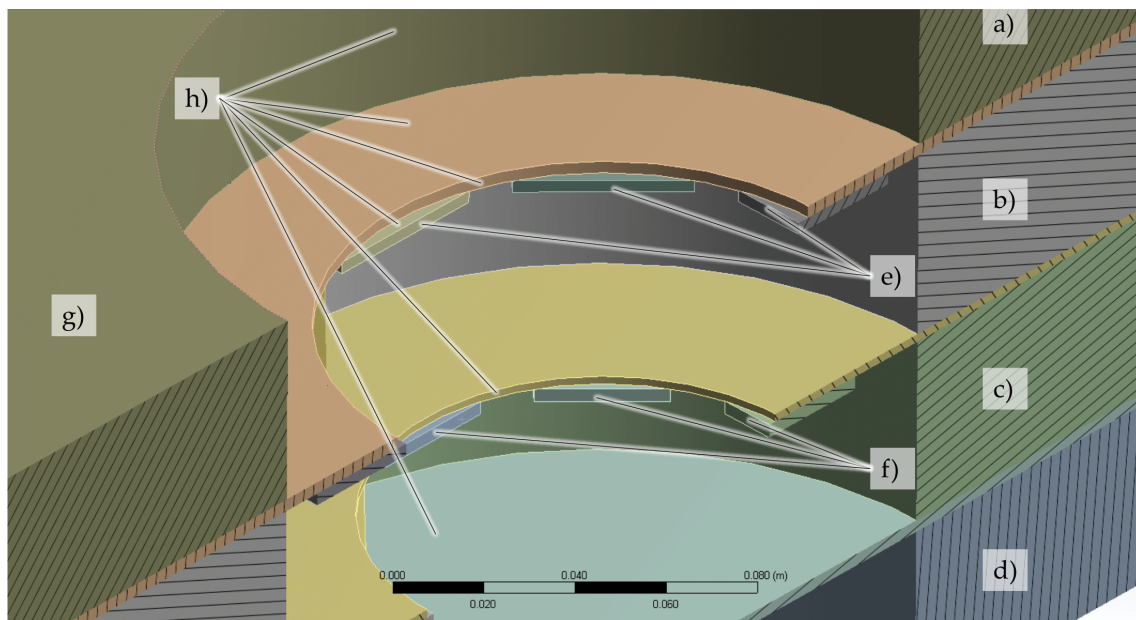


Figure 4.8: Detail of the sectional view depicted in Fig. 4.6 (own figure). a) to d): Cryogel<sup>®</sup>Z stacks 1. to 4., e) exemplary surfaces of specified temperature in contact with its thermal link to the first stage HX, f) exemplary surfaces of specified temperature in contact with the thermal link to the second stage HX, g) one of the two overall surfaces set to room temperature. The other one is at the bottom of d), h) exemplary surfaces of specified zero heat flux (adiabatic).

Adiabatic boundary conditions were applied to all surfaces not thermally connected to another surface or with no specified constant temperature such as g) in Fig. 4.8. The thermal contact conductance between thermally connected surfaces of any material was left for ANSYS® to calculate based on the largest material conductivity defined in the model. It yields a relatively high value and essentially provides perfect conductance between parts. This was deemed to be sufficiently accurate since its influence becomes insignificant for the poorly thermally conducting Cryogel Z which is in addition to that pressed mechanically against the copper surfaces. Furthermore, measures were taken to increase thermal conduction also between all relevant copper parts (see section 4.4). The iteration process between the numerical simulations mentioned in section 4.3.1 was based on the fact that the surfaces e) in Fig. 4.8 were planned to be thermally linked to the first stage HX of the PT420® via the thermal shield (see annotation c) in Fig. 4.7). Thus, the following steps were carried out to determine the cryocooler's operation point with no purposely added heat load to the system (exclusive heat conduction through the Cryogel Z):

1. specification of the same constant temperature on surfaces e) in Fig. 4.8,
2. conduction of numerical simulation on model depicted in Fig. 4.6 and determination of heat flow to thermal links,
3. with the heat flow information from 2., determination of respective first stage HX temperature using Fig. 4.5,
4. application of temperature determined in 3. and heat flow from 2. as boundary conditions for numerical simulation on model depicted in Fig. 4.7,
5. determination of new thermal link temperature from 4. and application of this temperature according to step 1.

During this process, the operational temperature of the 2<sup>nd</sup> stage HX (applied to surfaces f) in Fig. 4.8) was defined to have a constant value below 5 K. This represented a fixpoint in the simulation process. It had to be checked after every complete simulation process, however, if the resulting heat load on the 2<sup>nd</sup> stage HX at this fixed temperature exceeds the respective cooling capacity of the cryocooler. If this case was given, the Cryogel Z stack cross section  $A_{CG}$  had to be decreased before the next simulation run to ensure that the required 5 K could be supplied on the 2<sup>nd</sup> stage wafer with the respectively lower heat load.

### 4.3.3 Simulation Results

The conducted steady-state thermal numerical simulations allowed detailed insight in the thermodynamic behaviour of the planned cryostat interior. As an example for the obtained results, the temperature distribution for the experimental area model (see also Fig. 4.6) without additional Joule heating is depicted Fig. 4.9.

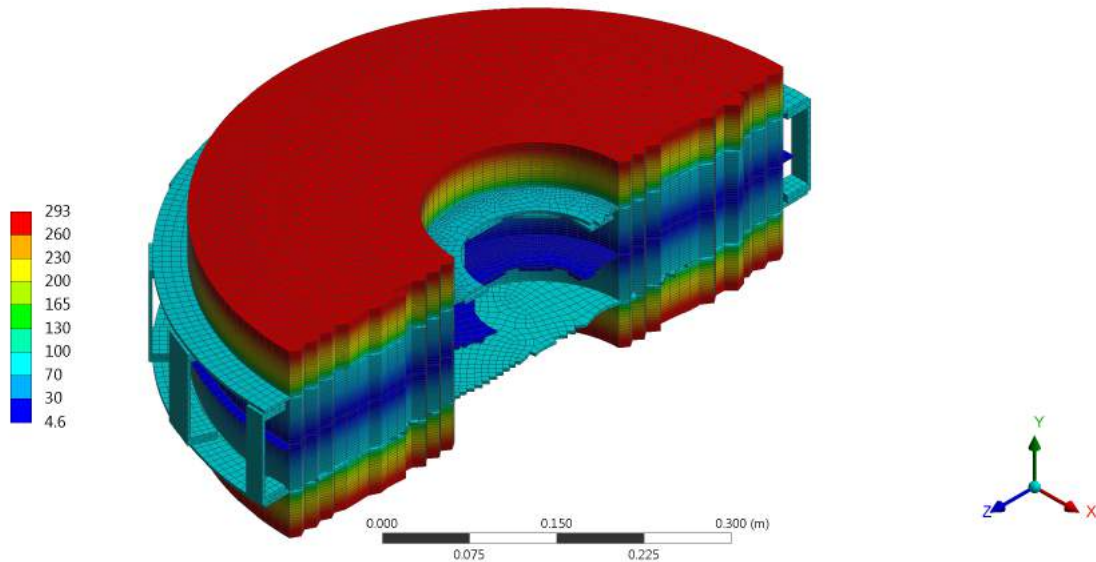


Figure 4.9: ANSYS<sup>®</sup> steady-state thermal simulation result: temperatures in the Cryogel<sup>®</sup>Z stacks, OFHC copper wafers and thermal links without Joule heating in the system (own figure, sectional view) Unit: Kelvin.

Thus, the simulations yielded many pieces of essential information to finalize the experimental setup development on the thermal evaluation of Cryogel Z for the objective stated in chapter 2. Exclusively the major ones are listed below:

- an approximation of the expected heat loads on the cryocooler to provide information for a detailed capacity mapping (see section 4.2.1),
- using the more detailed PT420<sup>®</sup> performance data, determination of the exact maximum Cryogel Z stack cross section  $A_{CG,max}$  still allowing for the required experimental temperatures on the OFHC copper wafers,
- first and second stage wafer temperatures without additional Joule heating with  $A_{CG,max}$  applied,
- the respective operation point of the cryocooler (provided cooling capacities and respective HX temperatures),
- the required thermal link cross sections for the heat removal from the wafers towards the HXs of the PTR at the above listed condition,
- the general wafer and thermal link design to additionally achieve a sufficiently homogeneous temperature distribution across the wafers .

All the obtained quantities are shown in Table 4.1 with their respective values.

Table 4.1: Major numerical simulation results quantities.

Quantity	Value
$A_{CG,max}$	0.251 m <sup>2</sup> (0.6 m outer and 0.2 m inner stack diameter)
Mean 1 <sup>st</sup> stage wafer temperature $\bar{T}_{1w}$	+0.72 K 64.6 -0.56 K
Mean 2 <sup>nd</sup> stage wafer temperature $\bar{T}_{2w}$	+0.017 K 4.73 -0.024 K
Heat load on 1 <sup>st</sup> stage HX $\dot{Q}_{1c}$	+13.40 W 76.9 -10.62 W
Heat load on 2 <sup>nd</sup> stage HX $\dot{Q}_{2c}$	+0.461 W 2.43 -0.419 W
Operational temperature 1 <sup>st</sup> stage HX $T_{0,1}$	+6.99 K 57.1 -4.73 K
Operational temperature 2 <sup>nd</sup> stage HX $T_{0,2}$	4.6 ±0 K (fixed)

The resulting 1<sup>st</sup> stage wafer temperature corresponding to the chosen  $A_{CG,max}$  lies closer to the warmer end of the interval of 40...80 K for the wanted intermediate temperature level stated in the objective (chapter 2). This is a result of the fact that during the manufacturing process of the cryostat-internal parts, it became clear that due to technical production reasons, the cryostat wall (Fig. 4.2 b)) was resulting lower than initially planned. Thus, with the thermal links and wafers already in production according to  $A_{CG,max}$ , the simulations had to be run again with stacks of 7 layers of Cryogel Z instead of the initially simulated larger number of layers which yielded the value of  $A_{CG,max}$  seen in Table 4.1. All other values in this table are, however, numerical simulation results for 7-layer-stacks. It was agreed on with the client, that, given these results the setup installation could be continued. The overwhelming share of the errors stated in Table 4.1 was caused by the thermal conductivity value uncertainties (see Fig. 1.7) supplied to ANSYS®.

#### 4.4 Final Experimental Setup

With the results of the PT420®'s performance determination and the partly in parallel conducted numerical simulations, a detailed 3D-model could be created in Autodesk Inventor®, which served as the basis for the manufacturing and installation of all mechanical and electrical parts and measurement devices. The purpose of this section is to give detailed insight into the construction of the final experimental setup which constitutes a large part of the work done.

#### 4.4.1 3D Test Stand Model

Figure 4.10 shows the Autodesk Inventor® 3D-Model of the experimental test stand setup prior to its operational state (Cryogel®Z stacks are not compressed).

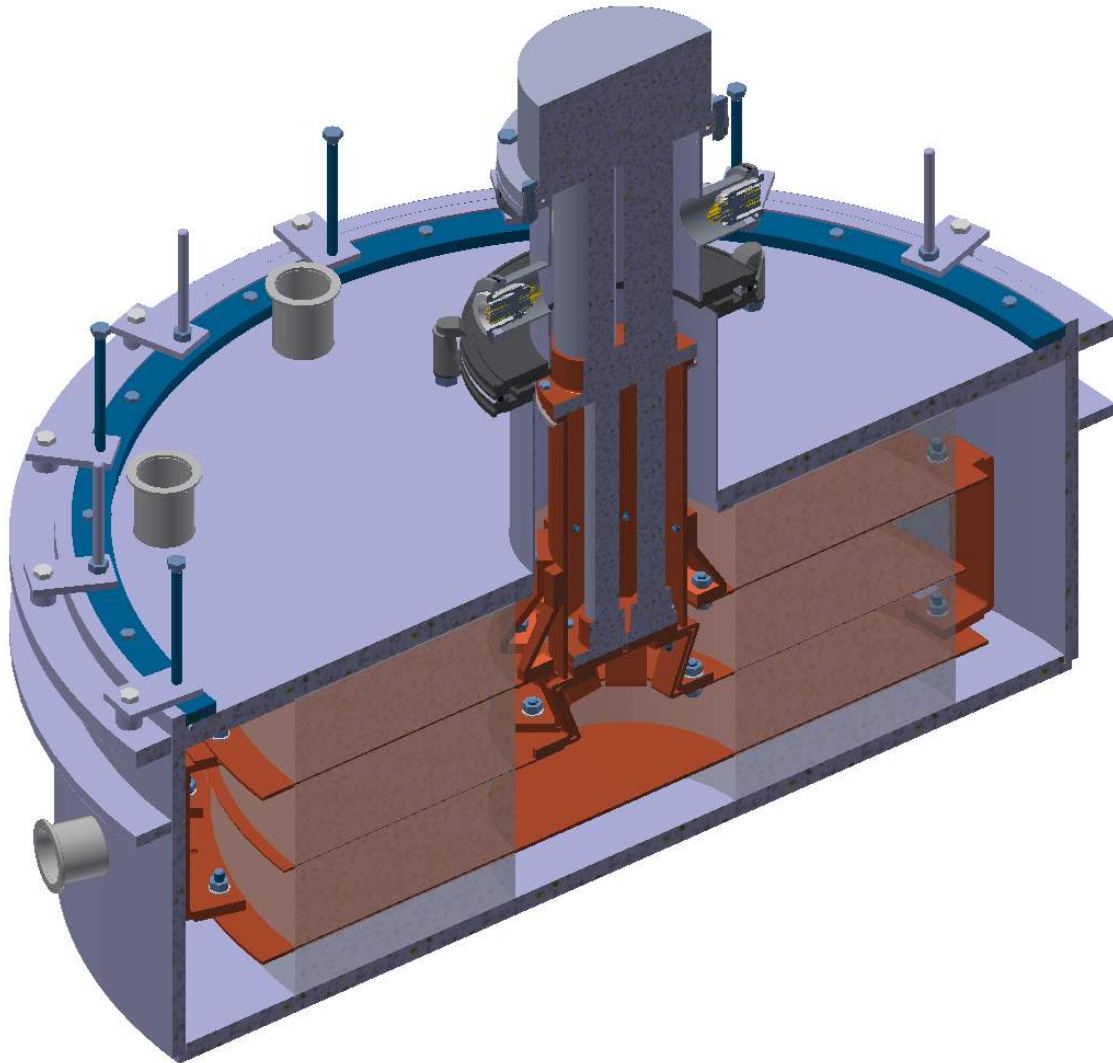


Figure 4.10: Half-sectional view of the experimental setup in before-operational, uncompressed state (Autodesk Inventor®2016). The inner vacuum vessel diameter is ca. 800 mm. The Cryogel®Z stacks are indicated with transparent appearance for improved overall clarity. The bottom stack was thinned artificially in this figure only to fit the top panel inside the cryostat with the uncompressed Cryogel Z geometries. Vacuum vessel assembly by courtesy of H. Silva.

The above shown model was created in uncompressed state to allow a more precise determination of the required thermal link lengths. The long bolts seen in Fig. 4.10 along the top rim of the cryostat vessel served for adjustment and fixation of the top panel, which applied the mechanical pressure on the Cryogel Z inside (see also Fig. 4.2). The thermal link slopes and shapes after compression were estimates. Their deformation functionality (no blocking of wafer movement, no creation of thermal shortcuts between OFHC copper parts in contact with differ-

ent PTR stages or the vacuum vessel wall) had to be experimentally verified. For final design examples, see section 4.4.2.

#### 4.4.2 Key Setup Parts and Measurement Device Placement

As mentioned in the previous sections, the flexible thermal links played a major role in the functionality provision of the experimental setup regarding an efficient heat removal from the OFHC copper wafers through the Cryogel<sup>®</sup>Z stacks and movement of the wafers and both top and bottom panel against each other while compressing the Cryogel Z. The chosen solution for this were OFHC copper braids consisting of many fine interwoven wires. They offered the same, high thermal conductivity at low temperatures while showing a sufficient flexibility without having large dimensions. The latter was also an important criterion considering the limited space inside the cryostat. Another advantage was that their shape in operational state was able to be pre-formed up to a certain degree by exclusively mechanical strain. At their ends, which had to be attached to the respective parts to be flexibly thermally linked, different installation solutions had to be found, depending on the given geometric conditions. These solutions included soldering rigid fitting pieces of OFHC copper to their ends for bolting and/or pressing them to the respective surfaces with no further attachments to the braids themselves. Both can be seen in the photo of exemplary pieces below (Fig. 4.11).

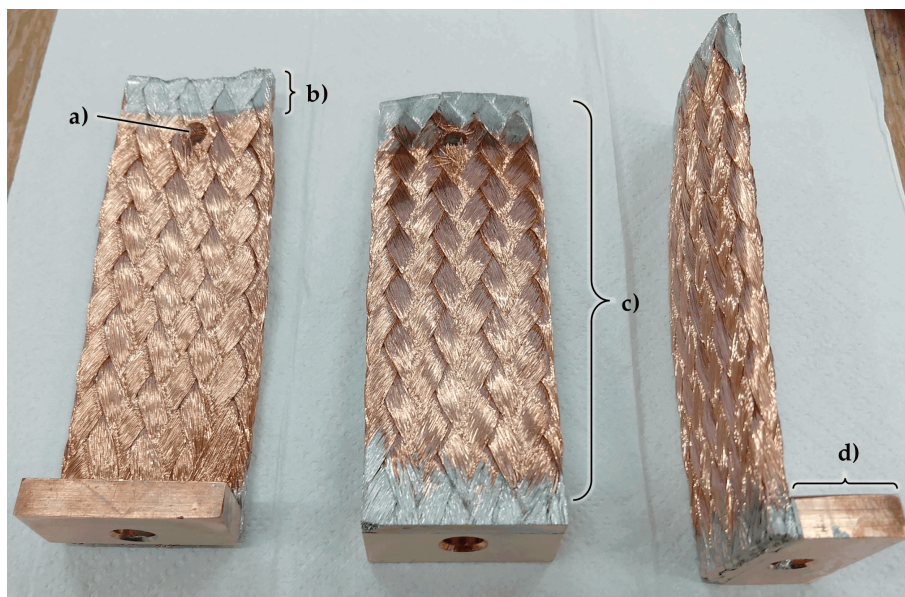


Figure 4.11: Photo of OFHC copper braids used to connect the upper 1<sup>st</sup> stage wafer to the thermal shield (Fig. 4.7). a) bolting hole, b) soldered braid cap to prevent unravelling of the wires, c) braided length (120 mm, flexible in the unsoldered middle part, d) rigid OFHC copper end piece for bolting on the wafer (own figure).

Similar parts as seen in Fig. 4.11 were used to interconnect both 1<sup>st</sup> stage wafers. Their installation is shown in the following photo in Fig. 4.12.

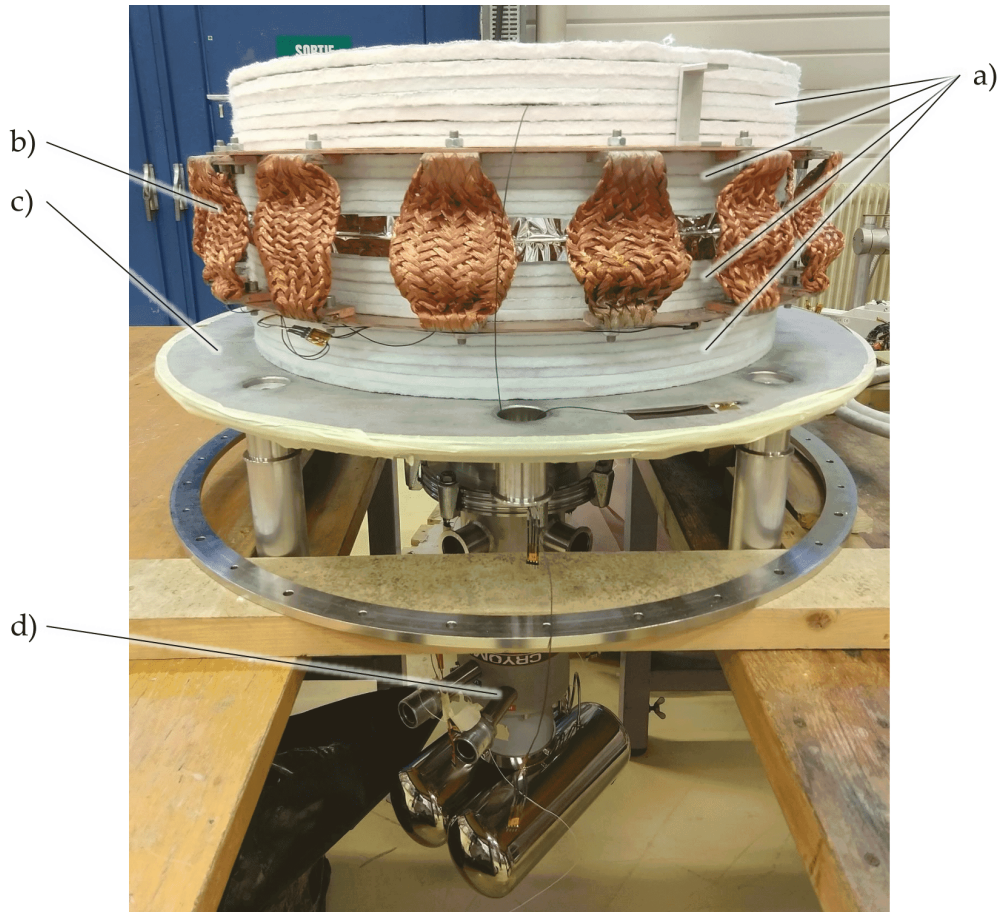


Figure 4.12: Photo of the cryostat interior with mounted PT420<sup>®</sup> during the installation process. a) Cryogel<sup>®</sup> Z stacks of 7 layers each, b) OFHC copper braid, c) Cryostat Z top panel, d) Cryomech<sup>®</sup> PT420 cold head top (own figure).

To improve the thermal contact between the OFHC copper braids and the wafers, the rigid end fittings were bolted through belleville washers that provide a constant compression of the bolt connection if the contraction of the connected parts during the cooling to lower temperatures is larger than the bolt contraction. Additionally, Apiezon<sup>®</sup> N vacuum grease with favourable thermal coupling properties was applied to the OFHC copper contact surfaces of the connections. These measures were taken for all part connections that required good thermal contact during operation. Figure 4.12 also shows hints of cabling and sensing devices (e.g. on the cryostat top panel). Their exact placement was crucial to obtain measurement possibilities of heat loads on both cryocooler stages according to the principle explained in section 3.3.3. To provide a better understanding of this, Fig. 4.13 shows the placement of temperature sensors and electric heaters inside the cryostat.



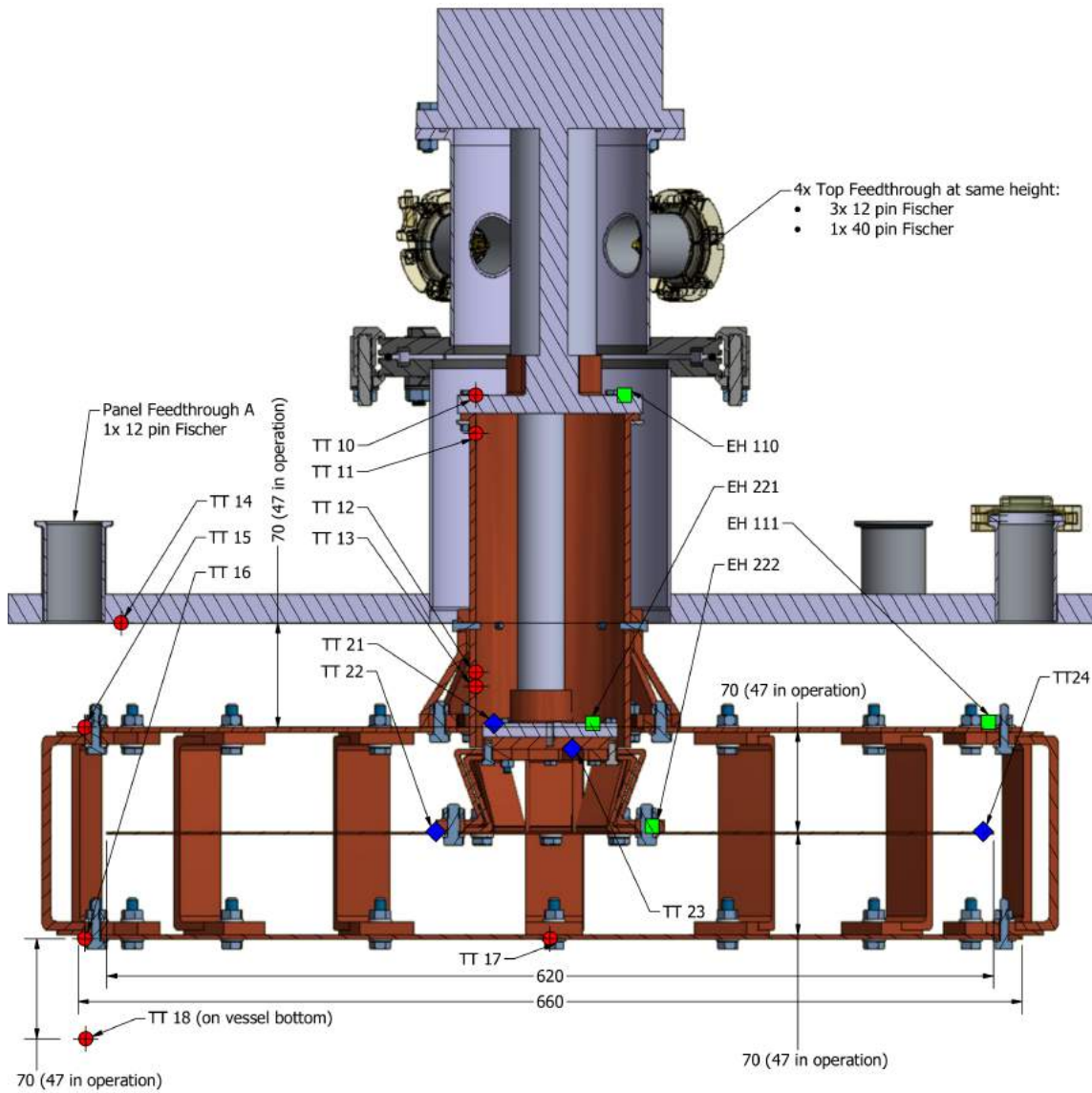
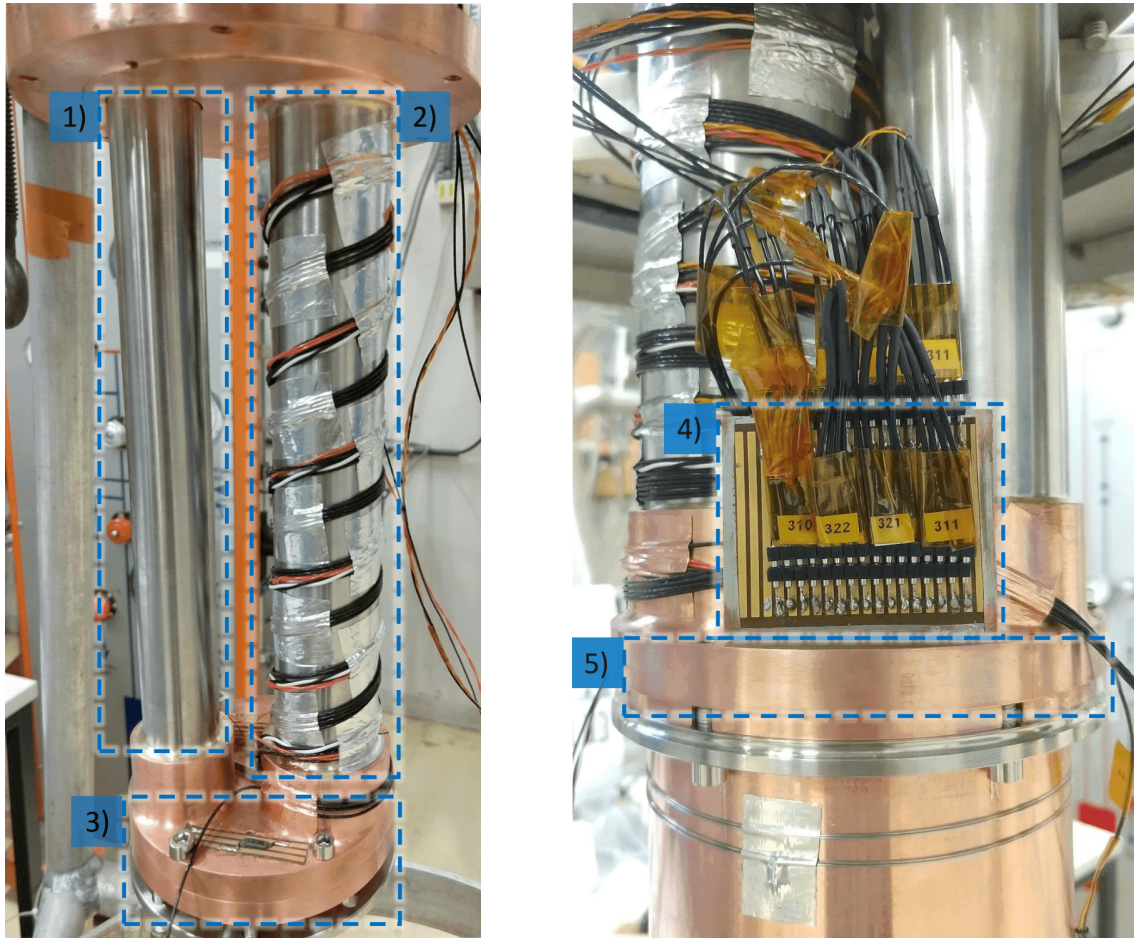


Figure 4.13: Sectional view of the test setup model without Cryogel<sup>®</sup>Z and cryostat bottom panel including measurement device locations. For simplicity reasons, the bottom panel is not shown. The scale is approximately 1:5.  
squares: electrical heaters (8 in total), stage 1: EH110 and EH111 (3x 50Ω in series), stage 2: EH221 and EH222 (3x 50Ω in series)  
circles: Pt100 sensors (9 in total), TT10 to TT18  
diamonds: TVO sensors (4 in total), TT21 to TT24 (own figure).

The installation of the above listed temperature sensors and electric heaters inside the cryostat included four wires for each device to allow for measurements according to the four-terminal sensing principle described in section 3.3.4. Depending on the exact device location and cabling port to the outside, these wires had lengths between 0.5 m and 1.5 m for devices on the first stage and between 1.5 m and 2.5 m on the second stage. To reduce the parasitic heat load due to  $\dot{Q}_{solid}$  (see section 3.1), all device cables thermally linked to the PT420<sup>®</sup>'s HXs were thermalized at an intermediate temperature. This was applied in two different ways described with the help of Fig. 4.14.



(a) Cable thermalization along the second stage regenerator tube. 1) second stage pulse tube, 2) second stage regenerator tube, 3) second stage HX.

(b) Cable thermalization on first stage HX. 4) Thermalization pad with soldered pin ports, 5) first stage HX.

Figure 4.14: Used cabling thermalization techniques (own figure).

The cable thermalization according to Fig. 4.14 b) was used exclusively for the wiring of the TVO sensors installed on the second stage vicinity (see Fig. 4.13) for two reasons. Firstly, only the sensors and heaters installed on second stage-connected parts were in contact with surfaces of lower temperature than the first stage HX to which the thermalization pad was attached and thus were the only candidates for thermalization at this location. Secondly, the thermalization of heater wiring can be given a lower priority since their purpose is adding heat load to the second stage in the first place. Due to the significantly higher currents running through their wiring, a thermalization according to Fig. 4.14 b) would cause a non-negligible amount of Joule heating on the thermalization pad because the current is running through its copper strips. Thermalization by winding the cables around the regenerator tubes, however, was done for all heaters and sensors. It is a commonly used technique since the outer regenerator wall temperatures decrease successively with the distance from the coldhead top part [30].

## 5 Heat Transfer Experiments with Cryogel<sup>®</sup>Z

With the test setup commissioned and installed, the experiments on the eligibility of Cryogel<sup>®</sup>Z for use as insulation material in ultrathin solenoids (see section 1.2.1) could be initiated. These experiments and their outcomes shall be described in the following sections.

### 5.1 Measurement Methodology

As mentioned in chapter 2, the aim of the experiments was to vary the temperature of the 1<sup>st</sup> stage wafers (see e.g. Fig. 4.6) according to the clients requests between 40 K and 80 K while keeping the 2<sup>nd</sup> stage wafer around 5 K maximum. At each temperature combination, the heat loads through the Cryogel<sup>®</sup>Z on either of the wafers ( $\dot{Q}_{1,CG}$  and  $\dot{Q}_{2,CG}$  respectively) were to be determined. In order to do this, the concept of *in-situ heat meter calibrations* described in section 3.3.3 was used. In this context, the fact was exploited that the heat arriving on either of the stages' wafers was forced to travel through all thermally linked parts towards the PT420<sup>®</sup>'s heat exchangers which represented the heat sinks for both stages. Since all of those parts were covered with MLI to the outside and the experiments were conducted in high vacuum, a sufficient insulation was given and thus the heat flow to both PTR heat exchangers had to be nearly the same as the heat flow through the Cryogel Z stacks. For an estimation of parasitic heat loads, please see Appendix E.

Considering the working principle of the *in-situ* heat meter calibrations (from here on called HMCs), several sets of heat meters were used on either stage. Since it is essential for the functionality of the heat meters to have  $\dot{Q}_{add}$  flow across their whole length to induce the complete respective  $\Delta T - \Delta T_0$ , not all installed temperature sensors were eligible for this purpose. To allow for a more detailed understanding of this measurement principle which is based on the heat flow domains and directions, please see Fig. 5.1.

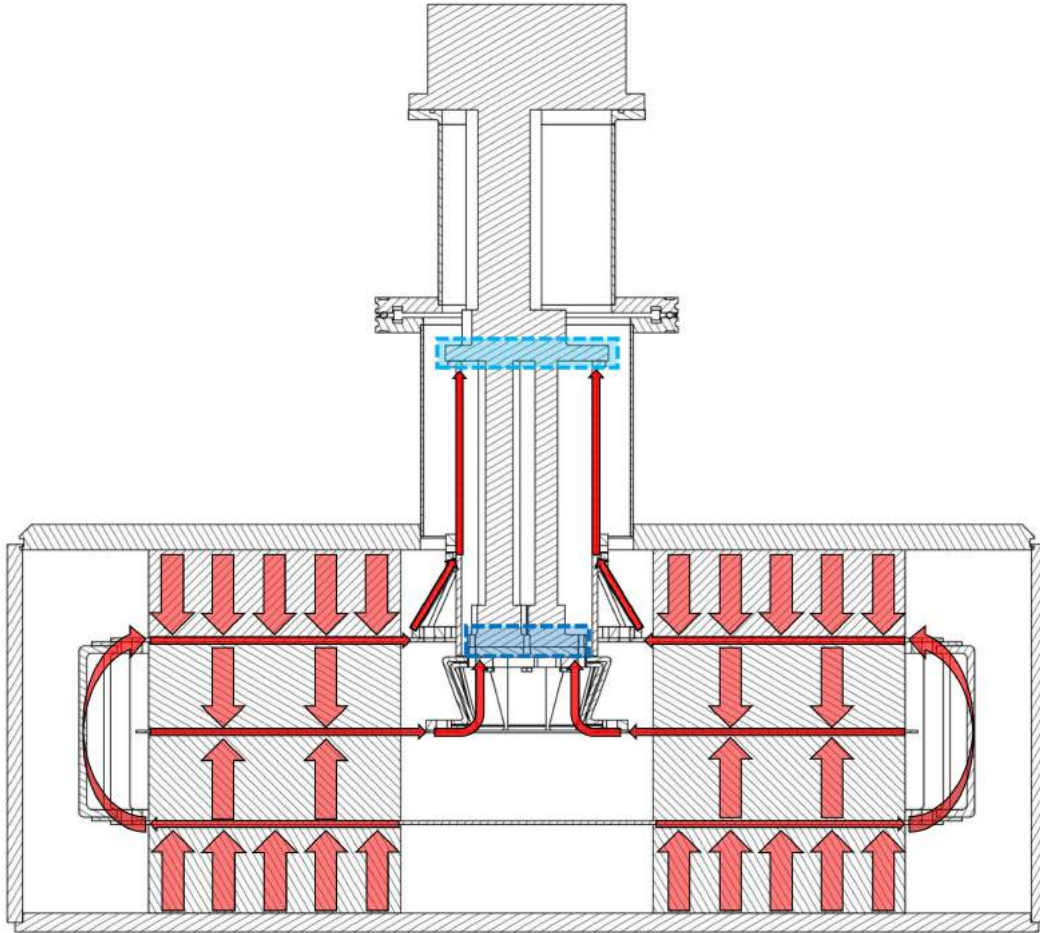


Figure 5.1: Qualitative visualization of non-parasitic heat flows through the Cryogel<sup>®</sup>Z stacks and inside the cold mass and thermal shield to the PTR's heat exchangers (own figure).

Below, the used temperature sensor combinations are listed. For their position inside the setup, please see Fig. 4.13.

- heat meters for determination of  $\dot{Q}_{1,CG}$ 
  - TT10/11 and TT12/13
  - TT10/11 and TT15
  - TT12/13 and TT15
- heat meters for determination of  $\dot{Q}_{2,CG}$ 
  - TT21 and TT23
  - TT21 and TT22
  - TT23 and TT22

As described in section 4.1, the first step in the experimental phase was the Cryogel Z compression via intermediate vacuum pumping to a specific value of  $p_{vac}$  that yields a 1 bar equivalent pressure  $p_{CG}$  on all Cryogel Z stacks. When additionally considering the overall weight of the cryostat top panel and its attach-

ments that increases the force on the Cryogel Z (approximately 110 kg) and the influence of O-ring sealings around the panel, the intermediate  $p_{vac}$  calculated to 490 mbar rounded. This pressure was set by adjusting the gas flow out of the system to an ALCATEL<sup>®</sup> A2012 rotary vane pump with a needle valve. Subsequently during this pumping process, the top panel was led down into the cryostat, following the created pressure difference by loosening the nut connections on the bolts screwed into the top panel (see Fig.4.10). Via these nuts, a counterforce against the one induced by the vacuum inside the cryostat could be applied to fix the top panel vertically in position.

Due to the large cold mass of the setup, large time constants were anticipated during the experimental phase. Thus, due to environmental reasons, the He-compressor was operated on a closed cooling water cycle with a dedicated chiller. Prior to switching on the compressor and thus starting the cool-down-phase of the PT420<sup>®</sup>, further vacuum had to be pumped on the system with a TURBOVAC<sup>®</sup> SL 700 turbo pump backed by a rotary vane vacuum pump with the top panel fixed in its position. This way, a pressure of  $9 \cdot 10^{-4}$  mbar was reached before starting the compressor. The resulting pressure at cold remained between  $3..4 \cdot 10^{-7}$  mbar throughout the measurements. It was measured and recorded via a Pfeiffer<sup>®</sup>PKR-251 full range vacuum gauge mounted to a flange in the cryostat's top panel.

During the whole measurement process, the necessary data for temperature and heat output determination via four-terminal sensing (see section 3.3.4) was recorded. All voltage drops were measured using an Astro-Med<sup>®</sup>Dash 18X data logger whereas the currents through the electrical heaters were determined by Keithley 2001<sup>®</sup>multimeters. Depending on the voltage needed, various power supplies were used. After having reached thermal equilibrium with only the PT420<sup>®</sup> switched on, the below listed steps were conducted repeatedly to determine  $\dot{Q}_{i,CG}$  for every set temperature combination of the OFHC copper wafers.

1. Raising of the temperature level on the 1<sup>st</sup> stage wafers approximately to the desired value by adding heat load via EH110  $\dot{Q}_{EH110}$  and waiting for thermal equilibrium.
2. Conducting the *in-situ* heat meter calibration for the 2<sup>nd</sup> stage by subsequently increasing the added heat load via EH222 in steps of 0.25 W or 0.5 W up to an added heat load of  $\dot{Q}_{EH222} = 2.5$  W or lower. This was limited by the caused increase of the 2<sup>nd</sup> stage wafer temperature. At each step, thermal equilibrium was awaited.
3. Setting  $\dot{Q}_{EH222} = 0$  and starting the in-situ heat meter calibration for the 1<sup>st</sup> stage by adding heat load via EH111  $\dot{Q}_{EH111}$  in steps of 2.5 W or 5 W up to  $\dot{Q}_{EH111} = 20$  W. As a measure to try to keep  $\lambda_{eff}$  (see equation (3.17)) constant by stagnating the absolute temperature level across the heat meter, every time  $\dot{Q}_{EH111}$  was increased,  $\dot{Q}_{EH110}$  was decreased by the same amount. Again, for each step thermal equilibrium was awaited.
4. Setting  $\dot{Q}_{EH111} = 0$  and starting from step 1 for a different temperature level.

The time until stabilization of the measured temperature values after changing the added heat load took between a few hours up to more than one day, depend-

ing on the amount by which the heat loads were changed. As a consequence of the course of action described in step 3, the lowest temperature level set in accordance with step 1 was the 1<sup>st</sup> stage wafer equilibrium temperature with  $\dot{Q}_{EH110} = 20 \text{ W}$  to be able to successively compensate the increase of  $\dot{Q}_{EH111}$  up to 20 W. Thus, at  $\dot{Q}_{EH110} = 0 \text{ W}$ , only an HMC for the second stage could be conducted.

## 5.2 Experimental Results

Following the measurement methodology, the very first result was obtained already in the process of compressing the Cryogel<sup>®</sup>Z stacks. When reaching a pressure of  $p_{vac} = 490 \text{ mbar}$  inside the cryostat equivalent to 1 bar pressure on the CryogelZ, the respective dilatation of the CryogelZ layers calculated to  $\epsilon = -0.263$  instead of the expected  $\epsilon = -0.324$  from the curves in Fig. 4.3. Since the stacks of CryogelZ in the experimental setup, however, represented a significantly larger sample size than the ones used to obtain those curves and because of their large uncertainties,  $\epsilon = -0.263$  was considered to be a more reliable value and the experimental procedure was continued.

From the further execution of the experimental heat load determination process, the below depicted HMC results were obtained (Figs. 5.2 to 5.4). Their tabulated values can be found in Appendix F. For every two HMCs conducted at a specific temperature combination of 1<sup>st</sup> and 2<sup>nd</sup> stage wafer temperature, this combination is given by the mean measurement values of TT15 and TT16 ( $\bar{T}_{1st}$ ) and TT22 and TT24 ( $\bar{T}_{2nd}$ ).

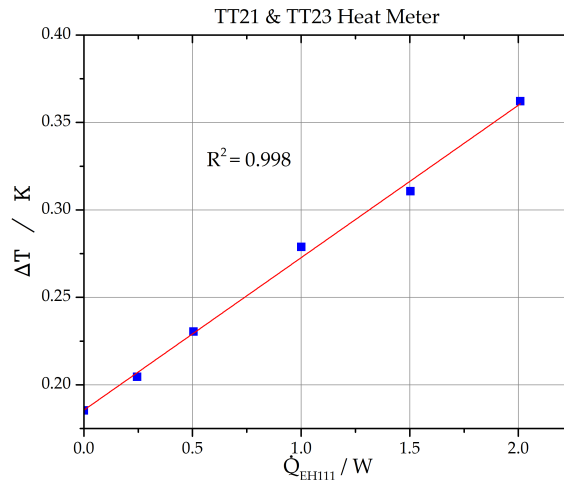


Figure 5.2: Plot of the 2<sup>nd</sup> stage HMC for  $\bar{T}_{1st} = 35.3 \pm 1.04 \text{ K}$  and  $\bar{T}_{2nd} = 5.45 \pm 0.070 \text{ K}$ .

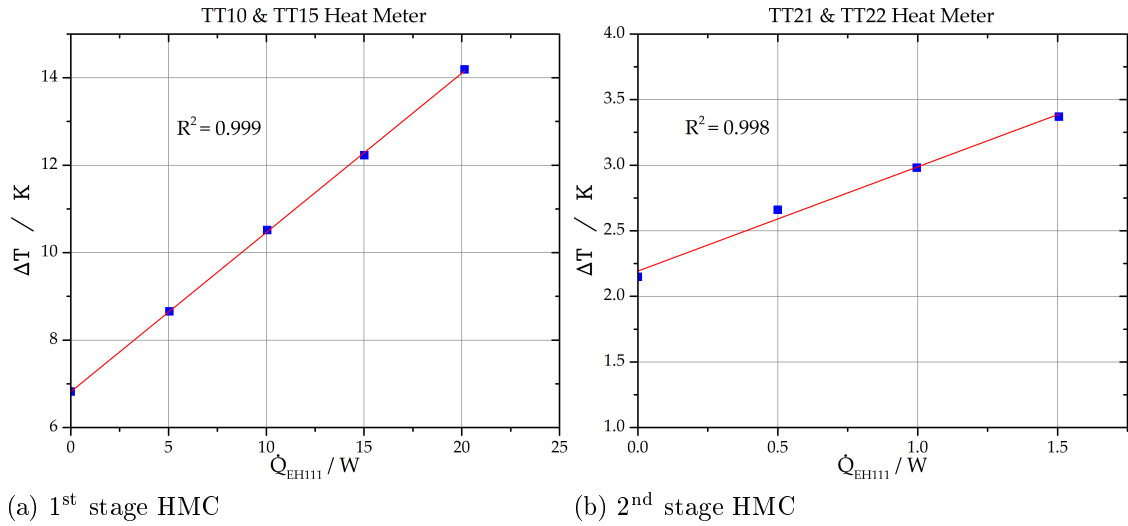


Figure 5.3: Plots of the HMCs for  $\bar{T}_{1st} = 40.3 \pm 1.00$  K and  $\bar{T}_{2nd} = 5.83 \pm 0.085$  K.

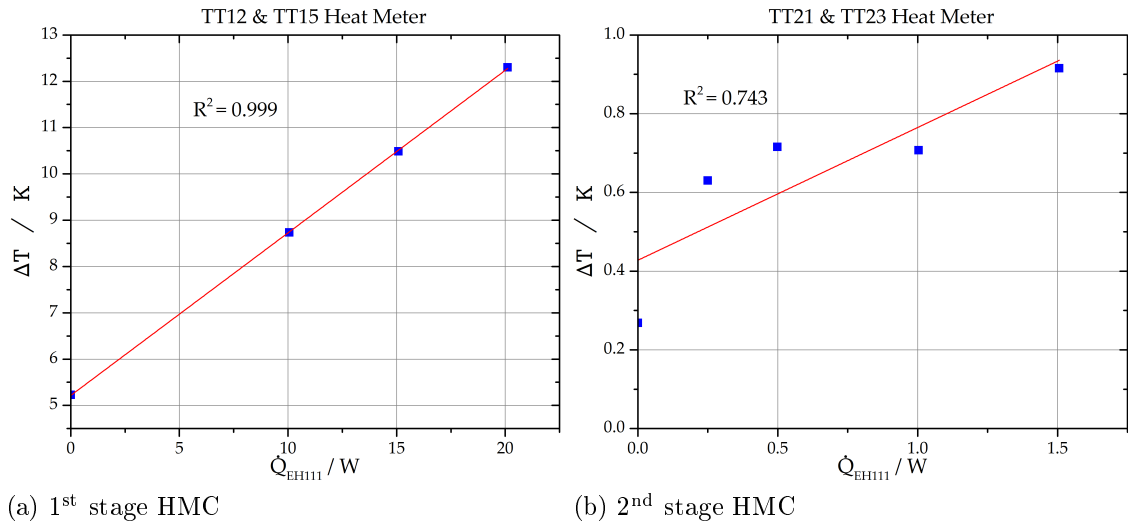


Figure 5.4: Plots of the HMCs for  $\bar{T}_{1st} = 52.7 \pm 0.94$  K and  $\bar{T}_{2nd} = 6.80 \pm 0.130$  K.

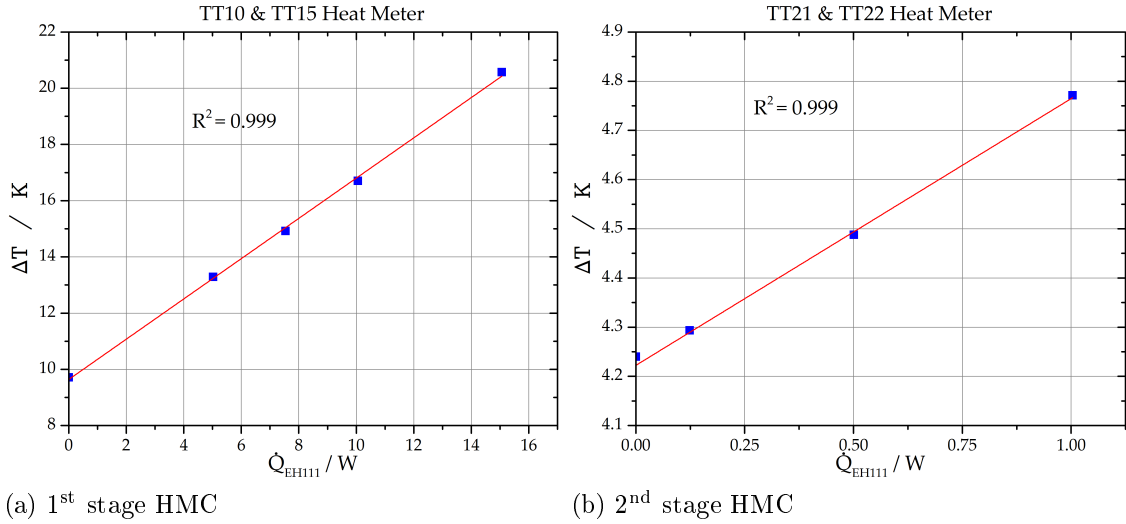


Figure 5.5: Plots of the HMCs for  $\bar{T}_{1^{st}} = 80.3 \pm 0.85 \text{ K}$  and  $\bar{T}_{2^{nd}} = 15.91 \pm 0.462 \text{ K}$ .

These heat meters were chosen to conduct a linear regression and its extrapolation to  $\Delta T = 0$  to determine  $\dot{Q}_{i,CG}$  (heat load on either PTR stage through the Cryogel Z) according to the principle described in section 3.3.3. The figures above show that the coefficient of determination  $R^2$  for the chosen heat meters was always  $>0.998$  which represents an important indicator for the error propagation described in Appendix D. An exception to this is the 2<sup>nd</sup> stage HMC in Fig. 5.4. The experimental results obtained within the scope of this work did not yield sufficiently linear correlations for any of the available heat meters on the 2<sup>nd</sup> stage at this temperature combination. Additionally, for conducting a sufficiently precise fit of any other function type that would allow confident extrapolation to  $\Delta T = 0$ , not enough measurement points were able to be taken during the limited time of this thesis.

From every conducted HMC shown in Figs. 5.2 to 5.5, one value for  $\dot{Q}_{i,CG}$  was obtained. This yielded four result values for  $\dot{Q}_{2,CG}$  and three values for  $\dot{Q}_{1,CG}$  at the four different measured temperature combinations of  $\bar{T}_{1^{st}}$  and  $\bar{T}_{2^{nd}}$ . To obtain a value for  $\dot{Q}_{2,CG}$  for the configuration shown in Fig. 5.4 (b), the measured  $\Delta T_0$  from TT21 and TT22 was substituted into the more precise linear regression of the same heat meter at the lower shield temperature (see Fig. 5.3 (b)). This can be considered as a sufficiently precise alternative method of determining  $\dot{Q}_{2,CG}$  as long as the cryocooler's 2<sup>nd</sup> stage performance change regarding an increase or decrease of the 1<sup>st</sup> stage cooling capacity does not differ between both analysed temperature configurations. Hence, the respective heat meter reacts in the same way to an increased heat flow across it. This could be confirmed by checking the PT420<sup>®</sup>'s capacity map in Fig. 4.5.



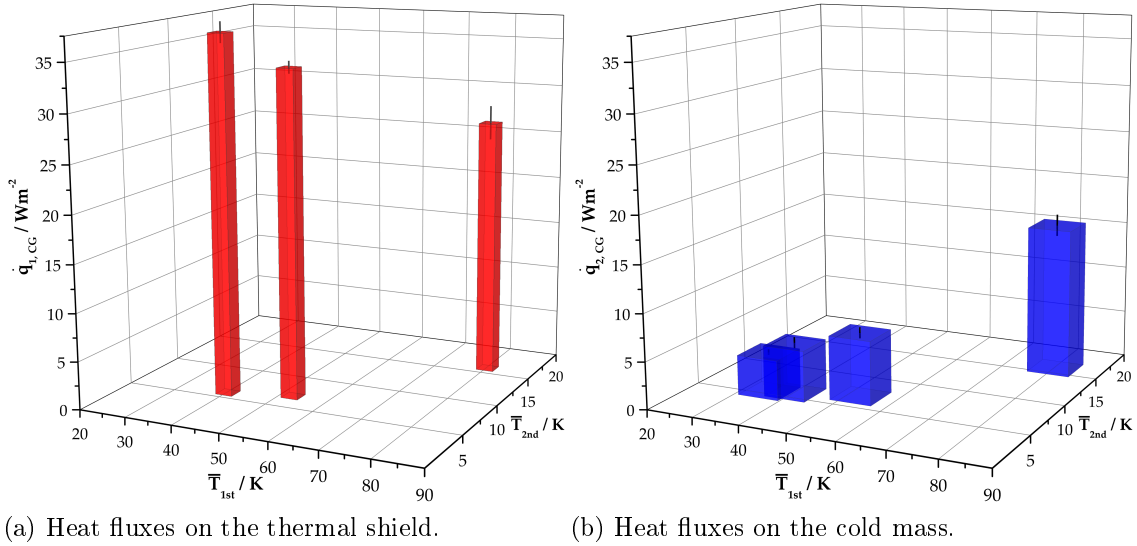


Figure 5.6: Experimental heat load results plotted against thermal shield temperature  $\bar{T}_{1st}$  and cold mass temperature  $\bar{T}_{2nd}$  (own figure). The heat load values obtained from the HMCs were scaled up to heat fluxes per  $\text{m}^2$  of 7-layer Cryogel<sup>®</sup>Z insulation. The respective heat flux errors are indicated at the top of each bar.

The heat flux trends through the Cryogel Z are clearly visible in Fig. 5.6. For a rising shield temperature  $\bar{T}_{1st}$ ,  $\dot{q}_{1,CG}$  successively decreases while  $\dot{q}_{2,CG}$  behaves contrarily and increases. Considering the decreasing thermal conductivity of Cryogel Z in the respective temperature range, it can be assumed qualitatively that  $\dot{q}_{2,CG}$  for  $\bar{T}_{1st} = 80.3 \text{ K}$  would not differ significantly for a cold mass temperature closer to 5 K, even when taking into account that  $\Delta T$  is around 10 K higher in that case. In connection with that, an energy balance around the thermal shield yields the same assumption for  $\dot{q}_{1,CG}$  in this context when  $\bar{T}_{1st}$  is not changed. Apart from this temperature configuration, it can be seen in Fig. 5.6 that the cold mass temperature  $\bar{T}_{2nd}$  could be kept fairly constant just above 5 K while raising the shield temperature  $\bar{T}_{1st}$ . For further quantitative result evaluation, the values from Fig. 5.6 are tabulated below in Table 5.1.

Table 5.1: Scaled up experimental heat flux result values of all analysed thermal shield temperature  $\bar{T}_{1st}$  and cold mass temperature  $\bar{T}_{2nd}$  combinations.

$\bar{T}_{1st} / \text{K}$	$\bar{T}_{2nd} / \text{K}$	$\dot{q}_{1,CG} / \frac{\text{W}}{\text{m}^2}$	$\dot{q}_{2,CG} / \frac{\text{W}}{\text{m}^2}$
$35.3 \pm 1.04$	$5.45 \pm 0.070$	-	$4.22 \pm 0.308$
$40.3 \pm 1.00$	$5.83 \pm 0.085$	$37.2 \pm 1.08$	$5.37 \pm 0.592$
$52.7 \pm 0.94$	$6.80 \pm 0.130$	$33.9 \pm 0.64$	$6.76 \pm 0.592$
$80.3 \pm 0.85$	$15.91 \pm 0.462$	$26.8 \pm 1.76$	$15.80 \pm 1.159$

The estimation in Appendix E shows that the share of parasitic heat loads of the above tabulated values for  $\dot{q}_{2,CG}$  is negligibly small and their share of  $\dot{q}_{1,CG}$  is below 8% for all of the investigated temperature combinations. To give a clearer,

direct comparison of the results in Table 5.1, they are plotted in one single diagram in Fig. 5.7.

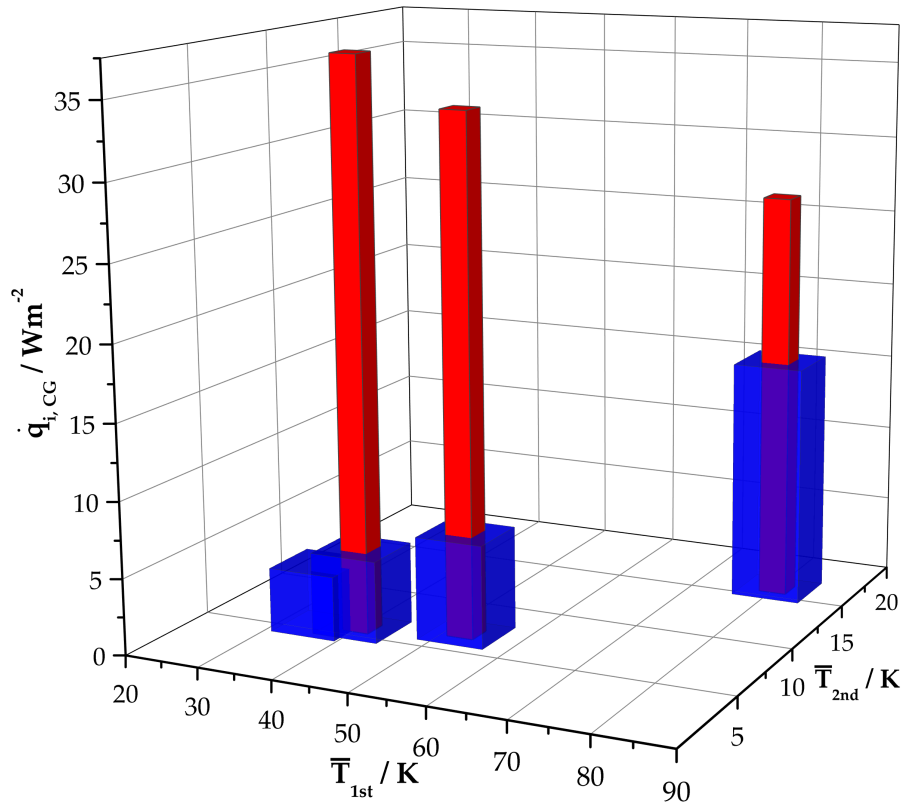


Figure 5.7: Experimental heat flux results plotted against thermal shield temperature  $\bar{T}_{1st}$  and cold mass temperature  $\bar{T}_{2nd}$  (own figure). The thicker, blue bars indicate heat fluxes through the Cryogel<sup>®</sup>Z insulation on the cold mass  $\dot{q}_{2,CG}$  while the thinner, red bars represent the heat fluxes on the thermal shield  $\dot{q}_{1,CG}$ . In this graph, the use of error bars was refrained for the sake of clarity. Their values can be found in Table 5.1.

## 6 Results Discussion

The purpose of this section is to evaluate all results obtained during this thesis. The experimental results shall first be discussed separately and afterwards compared to the conducted numerical simulations.

### 6.1 Experimental Results Evaluation

A general test setup development according to Fig. 4.1 was successfully executed during this thesis' work. The combination of the cryocooler performance determination and numerical simulations allowed for a complete commissioning and installation of a new, functional experimental setup. The flexible thermal links provided sufficiently small temperature differences between the upper and lower 1<sup>st</sup> stage wafer that did not exceed 1 K throughout all investigated shield temperature levels. Only between the PT420®'s 2<sup>nd</sup> stage HX and the cold mass, the flexible thermal links were responsible for a  $\Delta T$  in the range of 2 K, which explains the higher experimental values for the 2<sup>nd</sup> stage wafer temperature in comparison with the numerical results. For three out of the four measured temperature levels on the cold mass, however, it was still in an acceptable range. Reaching  $\bar{T}_{2nd} = 15.91$  K when raising  $\bar{T}_{1st}$  to 80.3 K couldn't be avoided because of the PTR's internal performance characteristics when adding the heat load of  $\dot{Q}_{EH110} = 85$  W to reach this temperature. In combination with the higher-than-expected values of  $\dot{q}_{2,CG}$  (see Table 6.1), the cryocooler was operating at a higher  $T_0$  to provide the necessary cooling capacity for the cold mass. In the following paragraphs, the results from all investigated temperature levels shall be evaluated with further detail.

The amount of installed temperature sensors on the thermal shield and the cold mass provided a good overview of temperature gradients and heat meters for the heat load determinations. These applied heat meters show a satisfying linear fit quality for nearly every value in Table 5.1. Mostly, heat meters consisting of temperature sensors located far from each other (e.g. TT10 TT15 or TT21 TT22) showed the best fit qualities. This is due to the fact that with larger  $\Delta x$  of the heat meter,  $\Delta T$  increases for the same heat flow (see equation 3.16) and inaccuracies of measurement values for  $\Delta T$  are reduced.

The method of determining  $\dot{Q}_{i,CG}$  via *in-situ* heat meter calibrations in general, although showing long time constants for reaching thermal equilibria for every measurement point shown in figures 5.2 to 5.5 has a major advantage. When taking the mean value of the measured heat meter temperatures during a long timespan and subsequently using the obtained values to conduct a new calibration for every shield and cold mass-temperature combination, the noise of the individual temperature sensors can be neglected against the error resulting from the linear fit quality. This is why the relative errors for all heat loads only exceeded 9% in one case (11%), which was due to the fact that fewer points were measured for the linear regression (see Fig. 5.4 (a)) which increased the standard error for slope and intercept of the linear fit. Clearly, this advantage only comes

into play when a sufficiently precise linear fit can be conducted. As mentioned already in section 5.2, this was not given for any of the heat meters available on the cold mass for the temperature combination of  $\bar{T}_{1st} = 52.7$  K and  $\bar{T}_{2nd} = 6.80$  K (see Fig. 5.4 (b)). The most self-evident assumption is that this was caused by instabilities of the cryocooler performance at this temperature combination since the second stage's low temperature level  $T_0$  is especially sensitive regarding its cooling capacity  $\dot{Q}_c$  (see Fig. 4.5). These instabilities can be responsible for significantly increasing time constants and sensitivity in reacting to the added heat via EH222 in the scope of the HMCs. In favour of this explanation is also the fact that this particular HMC was conducted a second time without yielding better linear fit possibilities at the same temperature combination. Furthermore, the HMC depicted in Fig. 5.5 (b) which was conducted afterwards at a different temperature combination, a significantly more precise linear fit could be achieved again. However, also in that case, the increasing performance instabilities were experienced and only one of the three available heat meters on the second stage yielded a sufficiently precise fit. Another explanation can be offered by the limited accuracy of the Astro-Med Dash 18X<sup>®</sup> data logger (see Appendix B) that was provided to measure and record differential voltages. At the respective temperature level of 6.80 K it only allowed for an absolute temperature measurement precision of  $\pm 0.130$  K. The data logger's accuracy was in general the main reason for the relatively large uncertainties of the otherwise precisely factory-calibrated TVO sensors' absolute temperature measurements.

The two-point soft calibration method (see Appendix C) for the used Pt100 sensors, however, allowed for precise HMCs for every temperature combination. Thus, it successfully compensated the inaccuracies of the Pt100 sensors which were, for the most part, operated below their official operational temperature range that starts at 73.15 K. Although the highest-accuracy-class (1/10 DIN) Pt100 sensors were used, it was still their inaccuracy at these low temperatures that contributed the most to the relatively high uncertainties in absolute temperature measurements.

In summary, however, the provided and installed equipment allowed inherently conclusive experimental results that already provide further elaboration possibilities of the Cryogel<sup>®</sup>'s eligibility for the ultrathin solenoid concept (see section 1.2.1) in section 6.3.

## 6.2 Experimental and Numerical Results Comparison

Significant discrepancies between measured and expected temperatures according to the numerical simulation results were determined already during the execution of the experiments. For example, the thermal shield temperature at cold was observed to be far lower than what the numerical simulations had shown in Table 4.1. Since this way heat load determinations through the Cryogel<sup>®</sup>Z could be conducted at significantly lower thermal shield temperatures than expected, all the obtained experimental results for the heat fluxes  $\dot{q}_{i,CG}$  were cross-checked by conducting new numerical simulations on the existing model (see section 4.3) using the experimentally determined temperature values. The respective comparison is given in Table 6.1.

Table 6.1: Comparison of experimental and numerical results for  $\dot{q}_{i,CG}$  for measured shield and cold mass temperatures  $\bar{T}_{1st}$  and  $\bar{T}_{2nd}$ .

$\bar{T}_{1st,exp}$ /K	$\bar{T}_{2nd,exp}$ /K	$\dot{q}_{1,CG,exp}$ / $\frac{W}{m^2}$	$\dot{q}_{1,CG,num}$ / $\frac{W}{m^2}$	$\dot{q}_{2,CG,exp}$ / $\frac{W}{m^2}$	$\dot{q}_{2,CG,num}$ / $\frac{W}{m^2}$
35.3 $\pm 1.04$	5.45 $\pm 0.070$	-	-	4.22 $\pm 0.308$	2.29 $\pm 0.352$
40.3 $\pm 1.00$	5.83 $\pm 0.085$	37.2 $\pm 1.08$	158 $\pm 25.3$	5.37 $\pm 0.592$	2.84 $\pm 0.415$
52.7 $\pm 0.94$	6.80 $\pm 0.130$	33.9 $\pm 0.64$	155 $\pm 25.2$	6.76 $\pm 0.592$	4.20 $\pm 0.653$
80.3 $\pm 0.85$	15.91 $\pm 0.462$	26.8 $\pm 1.76$	144 $\pm 25.4$	15.80 $\pm 1.159$	7.00 $\pm 1.119$

There are two major insights to be gained from the above table. Firstly, the experimental and numerical results for  $\dot{q}_{2,CG}$  are similar throughout all tested conditions, especially when considering the uncertainties. The experimentally obtained values consistently exceed the numerical results for the 2<sup>nd</sup> stage/cold mass. A further explanation can be given by the consideration of parasitic heat loads, estimated values of which can be found in Appendix E. More attention, however, needs to be drawn towards the fact that the expected values for  $\dot{q}_{1,CG}$  exceed the experimentally determined ones by nearly a fourfold for every temperature. This can not exclusively be explained by the larger errors of the thermal conductivity measurements for Cryogel Z at higher temperatures (see Fig. 1.7) as those only cause uncertainties in the range of  $\pm 25 \frac{W}{m^2}$ . This calls for the search for systematic errors in the experimental execution. The self-evident explanation is that the contact pressure of the Cryogel Z layers insulating the thermal shield (see e.g. Fig. 4.12) against the cryostat top and/or bottom panel during the experimental phase was lower than the intended 1 bar and thus the thermal link to the environment was significantly weaker. The given measurements, however, do not provide an indication of such behaviour of the Cryogel Z (Fig. 4.3). Nevertheless it has to be pointed out that their reliability was questioned already when compressing the Cryogel Z stacks merely to a lower dilatation value ( $\epsilon = -0.263$ ) before the experiments than what should have been reached ( $\epsilon = -0.324$ ) according to the given curves.

Furthermore, one might also be drawn to the conclusion that a part of the thermal links that is responsible for allowing the movement of the upper 1<sup>st</sup> stage wafer towards the cryostat top panel could be too sturdy and thus lower the compression force on the upper Cryogel Z stack. However, none of the deformation tests conducted on the flexible links within their development phase supports this reasoning. In the end, naturally, there is also the possibility left that the effective thermal conductivity between thermal shield and ambient temperature is significantly better than the given measurements on compressed Cryogel Z allow to perceive. Based on this, in the following section, the Cryogel Z's application eligibility in the ultrathin solenoid concept is evaluated.

### 6.3 Conclusion for Cryogel<sup>®</sup>Z Application

The experimentally determined values for  $\dot{q}_{i,CG}$  can be used to estimate a total coefficient of performance (COP) for the whole cooling system of the ultrathin solenoid concept using carnot factors for the cooling capacity provision at the cold mass and thermal shield temperatures and the COP of an LHC-like cryoplant.

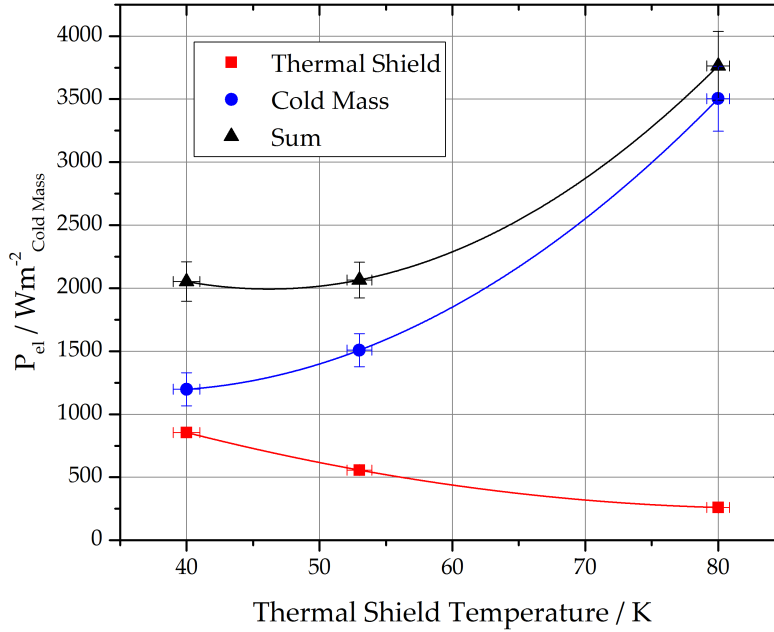


Figure 6.1: Estimation of required electrical powers  $P_{el}$  for cooling one square meter of cold mass surface at a temperature of 5 K using a thermal shield of the same surface area (own figure). Both the cold mass and the thermal shield were insulated with 7 layers of Cryogel<sup>®</sup>Z compressed by a 1 bar mechanical pressure load. The depicted error bars are exclusively based on this work's results. The errors of the cryoplant COPs were not considered.

Figure 6.1 depicts the estimation of required electrical energy of a cryoplant to provide the necessary cooling power for the thermal shield and the cold mass itself when both insulated with Cryogel<sup>®</sup>Z compressed by a 1 bar pressure load. These results were based firstly on the values for  $\dot{q}_{i,CG}$  obtained in the scope of this work that were taken over unchanged for the assumption of a constant thermal shield temperature of 5 K, Secondly, estimated data was used for the COP of the LHC cryoplants, which are operating at around 0.27 times the carnot factor for the provision of cooling power at the respective low temperature level. Thus, the summary curve of both required  $P_{el}$  yields with a second-grade polynomial fit the estimation that the minimum electrical power input is required for a thermal shield temperature of around 46...47 K. The respective value estimates to  $1750...2250 \frac{\text{W}_{el}}{\text{m}^2_{\text{Cold Mass}}}$  considering the uncertainties of the calculated points.

## 7 Proposals for Future Research and Development

As the results discussion has shown, there are multiple aspects worth looking into in further detail. The major remaining question is to what extent the low experimentally determined heat loads on the thermal shield one can trust. Thus, it would be important to first gain confidence about the contact pressures of the Cryogel<sup>®</sup>Z stacks insulating the thermal shield to the outside against the cryostat top and bottom panels. This could be achieved by the conduction of further dilatation tests that follow the same procedure of Cryogel Z compression with subsequent temperature decrease. Measurements could be either if the Cryogel Z further contracts when lowering the temperature while keeping the compression force constant or directly measuring the remaining contact pressure via strain gauges. Since the flexible Cryogel Z is expected to deform around said strain gauges when pressed against them, measures would need to be taken to avoid measurement distortions. The method via strain gauges could then also be applied directly to this work's setup, allowing for a contact pressure surveillance during the experiments.

Once that more expertise has been gained about the contact pressures, more detailed issues can be addressed. One would be to take measures to keep the cold mass temperature constant at 5 K maximum. Significant effort has already been put into the optimization of the thermal links during this thesis' work and there are only strongly limited options left to apply changes to lower the  $\Delta T$  between the PT420<sup>®</sup>'s second stage heat exchanger surface and its flexibly thermally linked wafer. Since it can additionally be said with confidence that the parasitic heat loads are low in comparison to  $\dot{Q}_{i,CG}$ , the remaining leverage is the Cryogel Z stack cross section which would need to be decreased to lower both  $\dot{Q}_{i,CG}$  to the cryocooler.

Lastly, the usage of a more accurate differential voltage measurement device (e.g. the Agilent<sup>®</sup>34401A Multimeter) is to be strongly suggested to allow for easier, more reliable determination of temperature difference values for the *in-situ* heat meter calibrations. This way, it should be more likely to obtain measurement data that provide a good linear fit quality throughout all measured temperature levels. Another option to enhance the heat load measurement result reception would be to run the test stand without any Cryogel Z but as well thermally insulated with MLI as possible and steer the wafer temperatures to the same values as when analysing the Cryogel Z. If the thermal shield and cold mass are left to stabilize in thermal equilibrium, for every chosen temperature combination the offsets between all sensors that should be at the same temperature can be determined precisely. These can then be used to improve the soft calibration method by adjusting the resistance curves for every measurement condition separately. Furthermore, the added heat via EH111 and EH222 could be increased successively by small discrete steps at every temperature level while keeping it constant on the respective stage by decreasing the added heat via EH110 or EH221 accordingly.  $\dot{Q}_{EH111}$ ,  $\dot{Q}_{EH222}$  and the respective temperature differences they cause need to be recorded just as described in this work. So, when reaching the same temperatures on the thermal shield and cold mass with the Cryogel Z installed, the temperature differences across the heat meters merely need to be compared to the values from the empty cryostat to determine the heat loads through the Cryogel<sup>®</sup>Z.

## Bibliography

- [1] BIPM, IEC, IFCC, ISO, IUPAC, IUPAP, OIML. Jcgm 100:2008 evaluation of measurement data – guide to the expression of uncertainty in measurement. [https://www.bipm.org/utils/common/documents/jcgm/JCGM\\_100\\_2008\\_E.pdf](https://www.bipm.org/utils/common/documents/jcgm/JCGM_100_2008_E.pdf), 2008. retrieved on 06/06/2019.
- [2] Cinzia De Melis. The CERN accelerator complex. Complexe des accélérateurs du CERN. Jan 2016. General Photo.
- [3] Ursula Bassler. CERN-Convention. <http://council.web.cern.ch/en/council/en/EuropeanStrategy/ESConvention.html>, 2019. retrieved 04/30/2019.
- [4] J. Bardeen, L. N. Cooper, and J. R. Schrieffer. Theory of superconductivity. *Phys. Rev.*, 108:1175–1204, Dec 1957.
- [5] Education , Communications and Outreach Group CERN. *LHC the guide*, 2017. retrieved 04/30/2019.
- [6] Jack W. Ekin. *Experimental Techniques for Low Temperature Measurements*. Oxford University Press, 2006.
- [7] G. Aad and T. Abajyan et al. Observation of a new particle in the search for the standard model higgs boson with the atlas detector at the lhc. *Physics Letters B*, 716(1):1 – 29, 2012.
- [8] The Royal Swedish Academy of Sciences. The Nobel Prize in Physics 2013 - Press Release. <https://www.nobelprize.org/uploads/2018/06/press-21.pdf>, October 2013. retrieved 06/05/2019.
- [9] Michael Benedikt, Mar Capeans Garrido, Francesco Cerutti, Brennan Goddard, Johannes Gutleber, Jose Miguel Jimenez, Michelangelo Mangano, Volker Mertens, John Andrew Osborne, Thomas Otto, John Poole, Werner Riegler, Daniel Schulte, Laurent Jean Taviani, Davide Tommasini, and Frank Zimmermann. Future Circular Collider. Technical Report CERN-ACC-2018-0058, CERN, Geneva, Dec 2018. Submitted for publication to Eur. Phys. J. ST.
- [10] Michelangelo Mangano, Patrizia Azzi, Michael Benedikt, Alain Blondel, Daniel Andreas Britzger, Andrea Dainese, Mogens Dam, Jorge de Blas, David Enterría, Oliver Fischer, Christophe Grojean, Johannes Gutleber, Claire Gwenlan, Clement Hulsens, Patrick Janot, Max Klein, Uta Klein, Matthew Philip Mccullough, Stephane Monteil, John Poole, Michael Ramsey-Musolf, Christian Schwanenberger, Michele Selvaggi, Frank Zimmermann, and Tevong You. Future Circular Collider. Technical Report CERN-ACC-2018-0056, CERN, Geneva, Dec 2018. Submitted for publication to Eur. Phys. J. C.
- [11] César Octavio Domínguez Sánchez de la Blanca, Leonid Rivkin, and Frank Zimmermann. Electron cloud studies for the LHC and future proton colliders, Jan 2014. Presented 13 Jan 2014.
- [12] CERN. The European Strategy for Particle Physics Update 2013. La stratégie



- européenne pour la physique des particules Mise à jour 2013. 16th Session of European Strategy Council. <https://cds.cern.ch/record/1567258>, May 2013. retrieved 06/05/2019.
- [13] Michael Benedikt, Alain Blondel, Olivier Brunner, Mar Capeans Garrido, Francesco Cerutti, Johannes Gutleber, Patrick Janot, Jose Miguel Jimenez, Volker Mertens, Attilio Milanese, Katsunobu Oide, John Andrew Osborne, Thomas Otto, Yannis Papaphilippou, John Poole, Laurent Jean Taviani, and Frank Zimmermann. Future Circular Collider. Technical Report CERN-ACC-2018-0057, CERN, Geneva, Dec 2018. Submitted for publication to Eur. Phys. J. ST.
- [14] CERN. Future Circular Collider. <https://home.cern/science/accelerators/future-circular-collider>, 2019. retrieved 06/05/2019.
- [15] Herman ten Kate, A. Dudarev, M. Mentink, E. Bielert, B. Cure, A. Gaddi, V. Klyukhin, H. Gerwig, C. Berriaud, U. Wagner, and H. Silva. Detector Magnets for the Future Circular Collider. [https://indico.cern.ch/event/763185/contributions/3166987/attachments/1727938/2791790/C4OrB-02-TenKate-FCChh\\_Detector\\_Magnets.pdf](https://indico.cern.ch/event/763185/contributions/3166987/attachments/1727938/2791790/C4OrB-02-TenKate-FCChh_Detector_Magnets.pdf), July 2017.
- [16] J P Badiou, J Beltramelli, J M Baze, and J Belorgey. *ATLAS barrel toroid: Technical Design Report*. Technical Design Report ATLAS. CERN, Geneva, 1997. Electronic version not available.
- [17] Herman ten Kate. Detector Magnets for the Future Circular Collider. [https://indico.cern.ch/event/656491/contributions/2939122/attachments/1629705/2597192/20180409-TenKate\\_-\\_FCCee\\_IDEA\\_thin\\_2T\\_Solenoid.pdf](https://indico.cern.ch/event/656491/contributions/2939122/attachments/1629705/2597192/20180409-TenKate_-_FCCee_IDEA_thin_2T_Solenoid.pdf), April 2018.
- [18] Matthias Mentink, Helder Silva, Alexey Dudarev, Erwin Bielert, Vyacheslav Klyukhin, Benoit Cure, Hubert Gerwig, Andrea Gaddi, Christophe Berriaud, Udo Wagner, and Herman ten Kate. Evolution of the conceptual fcc-hh baseline detector magnet design. *IEEE Transactions on Applied Superconductivity*, 12 2017.
- [19] V. Ilardi, H. Silva, A. Dudarev, T. Koettig, P. Borges de Sousa, L. N. Busch, T. Kulenkampff, E. R. Bielert, and H. H J. ten Kate. Development of light and highly radiation transparent cryostats for FCC detector magnets: first analyses of insulation materials. *IOP Conf. Ser. Mater. Sci. Eng.*, 502(1):012083, 2019.
- [20] H F P Silva, V Ilardi, T Kulenkampff, A Dudarev, and H H J ten Kate. Design of an ultra-thin, radiation thickness minimized, metallic cryostat for a 2t/4m free bore detector solenoid. *IOP Conference Series: Materials Science and Engineering*, 502:012084, apr 2019.
- [21] Aspen Aerogels, Inc. Safety Data Sheet: Cryogel Z<sup>®</sup>. <https://www.aerogel.com/products-and-solutions/product-documents/>. retrieved 08/05/2019.
- [22] Aspen Aerogels, Inc. Data Sheet: Cryogel Z<sup>®</sup>.

- <https://www.aerogel.com/products-and-solutions/product-documents/>.  
retrieved 08/05/2019.
- [23] NASA. Aerogel: From aerospace to apparel. Technical report, Kennedy Space Center; Cocoa Beach, FL United States, 2001.
- [24] B. E. Coffman, J. E. Fesmire, S. White, G. Gould, and S. Augustynowicz. Aerogel blanket insulation materials for cryogenic applications. *AIP Conference Proceedings*, 1218(1):913–920, 2010.
- [25] Aspen Aerogels, Inc. Cryogel z<sup>®</sup> product website. <https://de.aerogel.com/produkte-und-losungen/cryogel-z/>. retrieved 08/05/2019.
- [26] C L Choy and D Greig. The low-temperature thermal conductivity of a semi-crystalline polymer, polyethylene terephthalate. *Journal of Physics C: Solid State Physics*, 8(19):3121–3130, oct 1975.
- [27] American Society for Testing and Materials. ASTM Standard C177, 2019.
- [28] W. M. Kays and A. L London. *Compact heat exchangers*. Malabar, Fla Krieger Pub. Co, repr. ed. 1998 with corrections edition, 1998. Includes bibliographical references and index. Reprint. Originally published: New York :McGraw-Hill, 1984.
- [29] Hartmut Frey, Franz Xaver Eder, and René A Haefer. *Tieftemperaturtechnologie*. VDI, Düsseldorf, 1981.
- [30] Torsten Koettig. *Dünnschichtsysteme für die effektive Tieftemperaturregeneration*. PhD thesis, 2008.
- [31] E. I. Mikulin, A. A. Tarasov, and M. P. Shkrebyonock. *Low-Temperature Expansion Pulse Tubes*. Springer US, Boston, MA, 1984.
- [32] Ray Radebaugh, James Zimmerman, David R. Smith, and Beverly Louie. *A Comparison of Three Types of Pulse Tube Refrigerators: New Methods for Reaching 60K*, pages 779–789. Springer US, Boston, MA, 1986.
- [33] H. Pan, A. Hofmann, and L. Oellrich. Single-stage 4-valve and active buffer pulse tube refrigerators. *Cryogenics*, 41(4):281 – 284, 2001.
- [34] W E. Gifford and R C. Longworth. Pulse-tube refrigeration. *Journal of Engineering for Industry*, 86:264–268, 01 1964.
- [35] Graham Walker. *Cryocoolers*. Plenum Press, 1983.
- [36] Cryomech Inc. *PT420 CPA1114 CRYOREFRIGERATOR*, 2017.
- [37] Z.H. Gan, W.Q. Dong, L.M. Qiu, X.B. Zhang, H. Sun, Y.L. He, and R. Radebaugh. A single-stage gm-type pulse tube cryocooler operating at 10.6k. *Cryogenics*, 49(5):198 – 201, 2009.
- [38] Steffen Grohmann. Physical foundations of cryogenics. Lecture at the Institute for Technical Thermodynamics and Refrigeration, Karlsruhe Institute of Technology, 2017.

- [39] Y. Matsubara and J.L. Gao. Novel configuration of three-stage pulse tube refrigerator for temperatures below 4 k. *Cryogenics*, 34(4):259 – 262, 1994.
- [40] PJ Gareis and Gr F Hagenbach. Cryosorption. *Industrial & Engineering Chemistry*, 57(5):27–32, 1965.
- [41] Heinrich Gröber, Siegmund Erk, and Ulrich Grigull. *Die Grundgesetze der Wärmeübertragung*. Springer-Verlag, 2013.
- [42] Verein Deutscher Ingenieure. *VDI-Wärmeatlas*. Springer Berlin Heidelberg, 2013.
- [43] Marian Pruteanu, Adrian Radu, Adrian Ciobanu, and Adrian Iacob. A closer examination of the thermal performance of multifoil insulations. 06 2011.
- [44] David V Hutton and Jianhua Wu. *Fundamentals of finite element analysis*, volume 1. McGraw-hill New York, 2004.
- [45] Ajay Harish. Meshing of gears in contact. <https://www.simscale.com/blog/2016/10/what-is-finite-element-method/>, 2019. retrieved 05/30/2019.
- [46] J. N. Reddy. *An Introduction to the Finite Element Method*. McGraw-Hill, Inc., 1993.
- [47] Ray Browell. Accelerating to convergence. *ANSYS Advantage*, 1(3), 2007.
- [48] Adi Ben-Israel. A newton-raphson method for the solution of systems of equations. *Journal of Mathematical analysis and applications*, 15(2):243–252, 1966.
- [49] H. Crew. *General Physics: An Elementary Text-book for Colleges*. Macmillan, 1910.
- [50] Mosca Gene Tipler, Paul A. *Physik*. Springer Sepktrum, 2019.
- [51] National Physical Laboratory. Questions and answers. <https://www.npl.co.uk/resources/q-a/platinum-resistance-thermometer>, 2019. retrieved on 02/06/2019.
- [52] RdF Corporation. Platinum rtd probe construction. [http://www.rdfcorp.com/anotes/pa-r/pa-r\\_01.shtml](http://www.rdfcorp.com/anotes/pa-r/pa-r_01.shtml), 2019. retrieved on 02/06/2019.
- [53] Lakeshore Cryotronics, Inc. Pt-100 platinum rtds. <http://irtfweb.ifa.hawaii.edu/iqup/domeenv/PDF/pt100plat.pdf>, 2002. retrieved on 01/06/2019.
- [54] Lakeshore Cryotronics, Inc. Appendix d: Sensor calibration accuracies. [https://www.lakeshore.com/docs/default-source/temperature-catalog/lstc\\_appendixd\\_1.pdf?sfvrsn=51250de\\_2](https://www.lakeshore.com/docs/default-source/temperature-catalog/lstc_appendixd_1.pdf?sfvrsn=51250de_2), 2019. retrieved on 02/06/2019.
- [55] Temati UK Ltd. Carbon ceramic cryogenic sensors performance. <https://www.temati-uk.com/html/performance.html>, 2019. retrieved on 02/06/2019.

- [56] Tony R. Kuphaldt. *Lessons In Electric Circuits, Volume I - DC*. 5 edition, 2006. published on: <http://www.ibiblio.org/kuphaldt/electricCircuits/> ; retrieved on 06/06/2019.
- [57] M A Green, S S Chouhan, C Wang, and A F Zeller. Second stage cooling from a cryomech PT415 cooler at second stage temperatures up to 300 k with cooling on the first-stage from 0 to 250 w. *IOP Conference Series: Materials Science and Engineering*, 101:012002, dec 2015.
- [58] National Institute of Standards and Technology. Material properties: Ofhc copper. <https://trc.nist.gov/cryogenics/materials/OFHC2019>. retrieved on 12/02/2019.
- [59] Cryomech Inc. Pt420 cryocoolers. <https://www.cryomech.com/products/pt420/>, 2019. retrieved on 11/06/2019.
- [60] Temperature Controls Pty Ltd. RTD accuracy – Class A, Class B, 1/3 DIN, 1/10 DIN. <https://www.temperature.com.au/Support/RTDSensors/RTDaccuracyClassAclassB13DIN110DIN.aspx>, 2019. retrieved on 14/03/2019.
- [61] Ing Jostein Mårdalen, Ing Merete Hallenstvet, Ing Helene Bolm, Ing Volker Rekowski, Ing Bjørn Steinar Tanem, and John Erik Lein. Wärmereflektierende beschichtungen für aluminiumoberflächen.

## List of Figures

Figure1.1	Schematic of the CERN accelerator complex [2]. Specifically, the LHC accelerator chain starts with the proton source, followed by LINAC2, the BOOSTER, the PS and the SPS, from where the beams are injected in the LHC. All the accelerators are connected by beam transfer lines (TT). . . . .	1
Figure1.2	Scale comparison of the existing particle collider complex in Geneva and the FCC concept [14]. . . . .	3
Figure1.3	Baseline concept for FCC-hh detectors. Main components: a) Beam Tube b) Muon Absorber Disks c) Main Solenoid d) Radiation Shield e) Vacuum Vessel f) Electromagnetic Calorimeters g) Hadronic Calorimeters h) Trackers i) Muon Chambers j) Forward Solenoid. Based on [15]. . . . .	3
Figure1.4	Ultrathin solenoid concept with magnetic field lines. Figure based on [18]. The tracker is placed inside the superconducting solenoid, whereas the calorimeters are placed outside of it. An iron yoke is used to return the flux, thus completely shielding the magnetic field and providing the field integral needed to tag muons. . . . .	4
Figure1.5	Conceptual scheme of the FCC- $ee^+$ cylindrical cryostat with a 4 m bore and 6 m length [19]. . . . .	5
Figure1.6	Photo of a 10 mm thick Cryogel Z blanket as sold by Aspen Aerogels <sup>®</sup> , Inc. [25]. On the top surface, a layer of glued aluminum foil can be seen. This is intended to prevent gases and humidity from penetrating the otherwise porous aerogel blankets in its application. . . . .	6
Figure1.7	Various thermal conductivity data ([6] and [26]). The values provided by Aspen Aerogels Inc. were acquired according to ASTM C177 ([22] and [27]). The data on G-10CR were fitted to experimental values of the author. . . . .	7
Figure3.1	Simplified sketch of a basic cryostat with an inserted Pulse Tube refrigerator cold head (own figure). The cold head with two temperature stages is flanged onto the vacuum vessel. To shield the colder second stage against thermal radiation from the vacuum vessel walls, the thermal shield is flanged onto the heat exchanger of the first stage. Both stages enable the required temperature levels on large surfaces for the mock-up experiment (see section 4). . . . .	9
Figure3.2	Principle of providing cooling power according to the Stirling-process based on [28]. The right side shows the idealized temperature distribution within the regenerator in the steady-state condition with the temperatures $T_c$ and $T_w$ of the cold and warm volumes $V_c$ and $V_w$ . . . . .	10

Figure3.3	Left: Single-stage PTR; Right: Two-Stage PTR with pulse tubes connected in parallel a) HP-line, b) LP-line, c) rotary valves, d) regenerators, e) pulse tubes with two heat exchangers each, one at the warm, one at the cold side, f) orifices, g) buffer volumes (own figure).	12
Figure3.4	Principle draft of MLI's working principle [43]. The amount of reduced arrows represents the thermal radiation at each temperature level. . . . .	15
Figure3.5	Non-uniform tetrahedral meshing (right) of three-dimensional gear models (left) [45] . . . . .	16
Figure3.6	Sketch of a thin-film Pt100 sensor. Sensor variations with dimensions down to merely a few mm width and length are available [52]. . . . .	18
Figure3.7	Typical Characteristics of Pt100 sensors [53]. . . . .	19
Figure3.8	Resistance curve of a typical TVO sensor in Ohms (adapted from [55]). . . . .	20
Figure3.9	Representative photo for all used TVO sensors (own figure). . .	20
Figure3.10	Principle depiction of unknown heat load determination via in-situ heat meter calibration (own figure). . . . .	22
Figure3.11	Four-terminal sensing wiring diagram for a single resistance to be measured ( $R_{\text{subject}}$ ). The Ammeter is connected to $R_{\text{subject}}$ via current-providing wires with resistance $R_{\text{wire}, 1}$ each. They can differ from the wires connected exclusively to measure the voltage drop across $R_{\text{subject}}$ and thus may have a different resistance $R_{\text{wire}, 2}$ (own figure). . . . .	23
Figure4.1	This work's test setup development process visualization (own figure). The arrows represent both content dependencies and chronological sequence. . . . .	26
Figure4.2	Compression principle of Cryogel Z inside the cryostat (own figure). a) cryocooler cold head, b) cryostat wall, c) cryostat top panel, d) flexible thermal links, e) thermalized copper wafers, f) donut-shaped stacks of Cryogel <sup>®</sup> Z . The forced downwards movement of the cryostat's top panel causes the mechanical pressure on the stacks of Cryogel Z in between the cryostat panels and the wafers linked to the first and second stage PTR heat exchangers. . . . .	27
Figure4.3	Comparison of in-house measurement data on the dilatation $\epsilon = \frac{\Delta l}{l_0}$ of Cryogel <sup>®</sup> Z under compression at different conditions. Only the measurements at ambient temperature were repeated. Thus, the significantly larger error bars for these conditions reveal the domination of systematic errors due to the inhomogeneous structure of the Cryogel Z-fabric across the blanket (see section 1.2.2) which impedes precise measurements.	29

Figure4.4	Sketch of the cryocooler capacity measurement test stand (own figure). The MLI insulation around the second stage heat exchanger and around the thermal shield is not shown. On both PTR heat exchangers, resistors were installed to allow for Joule heating (see section 3.3.1). Temperatures were measured with two redundant Pt100 sensors on the first stage and a TVO sensor on the second stage. . . . .	30
Figure4.5	Capacity map of this work's Cryomech <sup>®</sup> PT420 PTR (own figure). Top/right: 1 <sup>st</sup> and 2 <sup>nd</sup> stage cooling capacity respectively. For the sake of clarity, the errors which were in the order of $\pm 0.75$ K for the first stage temperature measurements and $\pm 0.015$ K for the second stage are not depicted. An exemplary error calculation for the applied heat loads and temperatures can be found in Appendix D. For all tabulated values, please see Appendix F. . . . .	32
Figure4.6	Sectional view of the model geometry of the experimental space inside the vacuum vessel with non-uniform meshing (see section 3.2). a) to d): Cryogel <sup>®</sup> Z stacks 1. to 4. (see above), e) upper 1 <sup>st</sup> stage wafer, f) 2 <sup>nd</sup> stage wafer, g) lower 1 <sup>st</sup> stage wafer, h) flexible thermal links (own figure). The end of the thermal links to both of the PTRs heat exchangers are attached to the bottom of e) and f) towards their center. . . . .	34
Figure4.7	Sectional view of the model geometry of the thermal shield connected to the PT420 <sup>®</sup> 's first stage HX (own figure). a) mounting flange to bolt to the heat exchanger, b) shield with 4 mm thickness, c) ring for attachment of flexible thermal links. . . . .	35
Figure4.8	Detail of the sectional view depicted in Fig. 4.6 (own figure). a) to d): Cryogel <sup>®</sup> Z stacks 1. to 4., e) exemplary surfaces of specified temperature in contact with its thermal link to the first stage HX, f) exemplary surfaces of specified temperature in contact with the thermal link to the second stage HX, g) one of the two overall surfaces set to room temperature. The other one is at the bottom of d), h) exemplary surfaces of specified zero heat flux (adiabatic). . . . .	36
Figure4.9	ANSYS <sup>®</sup> steady-state thermal simulation result: temperatures in the Cryogel <sup>®</sup> Z stacks, OFHC copper wafers and thermal links without Joule heating in the system (own figure, sectional view) Unit: Kelvin. . . . .	38
Figure4.10	Half-sectional view of the experimental setup in before-operational, uncompressed state (Autodesk Inventor <sup>®</sup> 2016). The inner vacuum vessel diameter is ca. 800 mm. The Cryogel <sup>®</sup> Z stacks are indicated with transparent appearance for improved overall clarity. The bottom stack was thinned artificially in this figure only to fit the top panel inside the cryostat with the uncompressed Cryogel Z geometries. Vacuum vessel assembly by courtesy of H. Silva. . . . .	40

Figure4.11	Photo of OFHC copper braids used to connect the upper 1 <sup>st</sup> stage wafer to the thermal shield (Fig. 4.7). a) bolting hole, b) soldered braid cap to prevent unravelling of the wires, c) braided length (120 mm, flexible in the unsoldered middle part, d) rigid OFHC copper end piece for bolting on the wafer (own figure). . . . .	41
Figure4.12	Photo of the cryostat interior with mounted PT420 <sup>®</sup> during the installation process. a) Cryogel <sup>®</sup> Z stacks of 7 layers each, b) OFHC copper braid, c) Cryostat Z top panel, d)Cryomech <sup>®</sup> PT420 cold head top (own figure). . . . .	42
Figure4.13	Sectional view of the test setup model without Cryogel <sup>®</sup> Z and cryostat bottom panel including measurement device locations. For simplicity reasons, the bottom panel is not shown. The scale is approximately 1:5. <u>squares</u> : electrical heaters (8 in total), stage 1: EH110 and EH111 (3x 50 $\Omega$ in series), stage 2: EH221 and EH222 (3x 50 $\Omega$ in series) <u>circles</u> : Pt100 sensors (9 in total), TT10 to TT18 <u>diamonds</u> : TVO sensors (4 in total), TT21 to TT24 (own figure). . . . .	43
Figure4.14	Used cabling thermalization techniques (own figure). . . . .	44
Figure5.1	Qualitative visualization of non-parasitic heat flows through the Cryogel <sup>®</sup> Z stacks and inside the cold mass and thermal shield to the PTR's heat exchangers (own figure). . . . .	46
Figure5.2	Plot of the 2 <sup>nd</sup> stage HMC for $\bar{T}_{1st} = 35.3 \pm 1.04$ K . . . . .	48
Figure5.3	Plots of the HMCs for $\bar{T}_{1st} = 40.3 \pm 1.00$ K and $\bar{T}_{2nd} = 5.83 \pm 0.085$ K. . . . .	49
Figure5.4	Plots of the HMCs for $\bar{T}_{1st} = 52.7 \pm 0.94$ K and $\bar{T}_{2nd} = 6.80 \pm 0.130$ K. . . . .	49
Figure5.5	Plots of the HMCs for $\bar{T}_{1st} = 80.3 \pm 0.85$ K and $\bar{T}_{2nd} = 15.91 \pm 0.462$ K. . . . .	50
Figure5.6	Experimental heat load results plotted against thermal shield temperature $\bar{T}_{1st}$ and cold mass temperature $\bar{T}_{2nd}$ (own figure). The heat load values obtained from the HMCs were scaled up to heat fluxes per m <sup>2</sup> of 7-layer Cryogel <sup>®</sup> Z insulation. The respective heat flux errors are indicated at the top of each bar. . . . .	51
Figure5.7	Experimental heat flux results plotted against thermal shield temperature $\bar{T}_{1st}$ and cold mass temperature $\bar{T}_{2nd}$ (own figure). The thicker, blue bars indicate heat fluxes through the Cryogel <sup>®</sup> Z insulation on the cold mass $\dot{q}_{2,CG}$ while the thinner, red bars represent the heat fluxes on the thermal shield $\dot{q}_{1,CG}$ . In this graph, the use of error bars was refrained for the sake of clarity. Their values can be found in Table 5.1. . . . .	52
Figure6.1	Estimation of required electrical powers $P_{el}$ for cooling one square meter of cold mass surface at a temperature of 5 K using a thermal shield of the same surface area (own figure). Both the cold mass and the thermal shield were insulated with 7 layers of Cryogel <sup>®</sup> Z compressed by a 1 bar mechanical pressure load. The depicted error bars are exclusively based on this work's results. The errors of the cryoplant COPs were not considered. . . . .	56



---

FigureA.1	Used thermal conductivity values of OFHC with RRR = 100. Values are based on a fit function taken from [58]. . . . .	69
FigureB.1	Cryomech <sup>®</sup> 's capacity map for the PT420 pulse tube refrigerator. Merely the following values are given: "0 W ≤ 2.8 K, 2.0 W @ 4.2 K with 55 W @ 45 K" [59]. . . . .	70
FigureC.1	Maximum deviations from real temperature according to the 1/10 DIN standard for Pt100 thin film sensors [60]. The continuous curve represents a 5 <sup>th</sup> grade polynomial fit that also covers the newly rising deviations for temperatures exceeding 0 °C . . . . .	72
FigureE.1	MLI insulation of the experimental area against thermal radiation from the cryostat vessel walls (Photo by courtesy of V. Ilardi). a) nearly free-floating 20-layer MLI blanket, b) uncovered layers of Cryogel <sup>®</sup> Z. . . . .	78

## List of Tables

Table3.1	Properties of aluminized mylar films for parasitic heat load approximation . . . . .	15
Table4.1	Major numerical simulation results quantities. . . . .	39
Table5.1	Scaled up experimental heat flux result values of all analysed thermal shield temperature $\bar{T}_{1st}$ and cold mass temperature $\bar{T}_{2nd}$ combinations. . . . .	51
Table6.1	Comparison of experimental and numerical results for $\dot{q}_{i,CG}$ for measured shield and cold mass temperatures $\bar{T}_{1st}$ and $\bar{T}_{2nd}$ . . . . .	55
TableA.1	Used thermal conductivity values of Cryogel <sup>®</sup> Z at a 1 bar compression. . . . .	69
TableB.1	Tabulation of all devices used and their respective measurement parameter accuracies in the ranges of interest for this work. . . . .	71
TableE.1	Approximated parasitic heat loads for $\bar{T}_{1st} = 35.3$ K and $\bar{T}_{2nd} = 5.45$ K. $\dot{Q}_{1,CG}$ was not measured at these temperatures. . . . .	77
TableE.2	Approximated parasitic heat loads for $\bar{T}_{1st} = 40.3$ K and $\bar{T}_{2nd} = 5.83$ K . . . . .	77
TableE.3	Approximated parasitic heat loads for $\bar{T}_{1st} = 52.7$ K and $\bar{T}_{2nd} = 6.80$ K . . . . .	77
TableE.4	Approximated parasitic heat loads for $\bar{T}_{1st} = 80.3$ K and $\bar{T}_{2nd} = 15.91$ K . . . . .	78
TableF.1	Tabulated values for the HMC in Fig. 5.2. . . . .	80
TableF.2	Tabulated values for the HMC in Fig. 5.3 (a). . . . .	80
TableF.3	Tabulated values for the HMC in Fig. 5.3 (b). . . . .	80
TableF.4	Tabulated values for the HMC in Fig. 5.4 (a). . . . .	80
TableF.5	Tabulated values for the HMC in Fig. 5.4 (b). . . . .	80
TableF.6	Tabulated values for the HMC in Fig. 5.5 (a). . . . .	81
TableF.7	Tabulated values for the HMC in Fig. 5.5 (b). . . . .	81
TableF.8	Cooling capacity and temperature values of Fig. 4.5 with their respective errors. . . . .	81

## Appendix

### A Material Specifications

#### Cryogel<sup>®</sup>Z

Table A.1: Used thermal conductivity values of Cryogel<sup>®</sup>Z at a 1 bar compression.

T / K	$\lambda(T) / 10^{-3} \frac{\text{W}}{\text{m}\cdot\text{K}}$	Error / $10^{-3} \frac{\text{W}}{\text{m}\cdot\text{K}}$
6.1	0.93	$\pm 0.126$
7.3	1.16	$\pm 0.159$
10.4	1.63	$\pm 0.228$
20.1	2.81	$\pm 0.393$
32.0	3.36	$\pm 0.482$
59.1	3.29	$\pm 0.488$
87.1	4.76	$\pm 0.727$
108.2	6.33	$\pm 1.040$
149.8	11.27	$\pm 1.910$
203.1	21.69	$\pm 4.820$
231.7	29.56	$\pm 4.570$
293.7	53.48	$\pm 12.770$

#### OFHC Copper (RRR = 100)

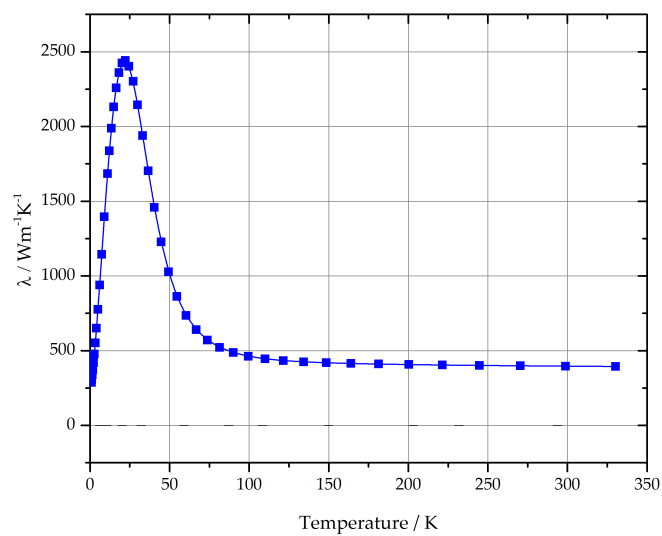


Figure A.1: Used thermal conductivity values of OFHC with RRR = 100. Values are based on a fit function taken from [58].

## B Equipment Specifications

### Cryomech<sup>®</sup>PT420 Capacity Map

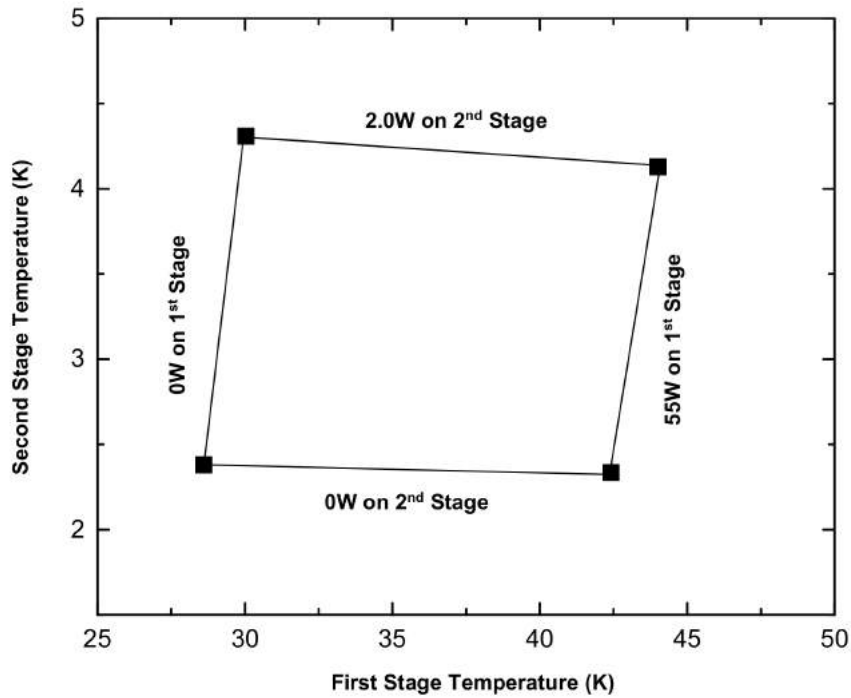


Figure B.1: Cryomech<sup>®</sup>'s capacity map for the PT420 pulse tube refrigerator. Merely the following values are given: "0 W  $\leq$  2.8 K, 2.0 W @ 4.2 K with 55 W @ 45 K" [59].

## Used Data Acquisition Devices

Table B.1: Tabulation of all devices used and their respective measurement parameter accuracies in the ranges of interest for this work.

Device	Parameter	Accuracy	Range & Unit
Aim <sup>®</sup> TTi PLH120 Multimeter	$I$	$0.003 \cdot I + 0.0003$	0.7500 A
Agilent <sup>®</sup> 34401A Multimeter	$I$	$0.001 \cdot I + 0.0001$	1.0000 A
Astro-Med <sup>®</sup> Dash 18X Data Acquisition Recorder	$U$	$0.005 \cdot U$	100.0000 V
Delta Elektronika <sup>®</sup> SM70-22 DC Power Supply	$U$	$0.005 \cdot U + 0.2$	70.0 V
Delta Elektronika <sup>®</sup> SM120-13 DC Power Supply	$U$	$0.005 \cdot U + 0.2$	120.0 V
Keithley <sup>®</sup> 2001 Multimeter	$I$	$0.00135 \cdot I + 0.00004$	2.0000 A
Lakeshore <sup>®</sup> 120 Current Source	$I$	$0.001 \cdot I$ $0.0005 \cdot I$	1 mA 10 $\mu$ A
National Instruments <sup>®</sup> PXI-4071 Multimeter	$U$	$0.00002 \cdot U + 0.0002$ $0.000005 \cdot U + 0.00008$	100.0000 V 100.00000 mV
R&S <sup>®</sup> HM8143 Multimeter	$I$	$0.0002 \cdot I + 0.001$	1.0000 A

## C Soft Calibration

It shall be stated at the beginning of this section with emphasis that the described procedure in the following paragraphs exclusively improved the sensors' uncertainties against each other. Their detection precision of absolute temperatures values can not be assumed to have increased this way.

For the heat transfer experiments in this work, thin film Pt100 sensors (as depicted in Fig. 3.6) of 1/10 DIN accuracy class were used. This class guarantees the following maximum deviations from the real temperature value when following the standardized resistance curve (see Fig. 3.7 (a)):

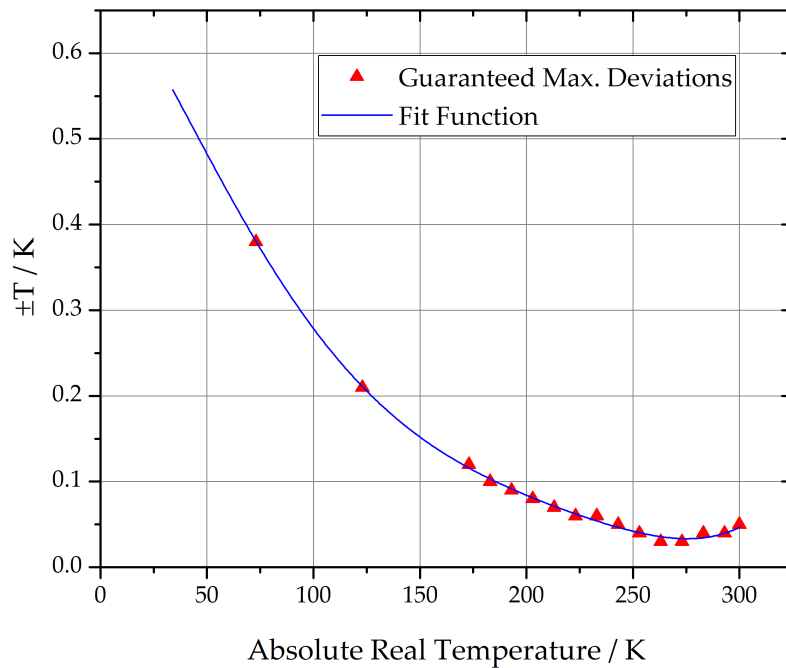


Figure C.1: Maximum deviations from real temperature according to the 1/10 DIN standard for Pt100 thin film sensors [60]. The continuous curve represents a 5<sup>th</sup> grade polynomial fit that also covers the newly rising deviations for temperatures exceeding 0 °C .

The fit curve in Fig. C.1 shows the large possible deviations in the temperature range of interest in the experiments (30...90 K). These deviations would significantly impede the in-situ heat meter calibrations with the used Pt100 sensors since temperature differences of a few Kelvin need to be determined between them more precisely to allow for a sufficiently reliable detection of the correlations between  $\dot{Q}_{add}$  and the resulting  $\Delta T$  across the heat meters (see section 3.3.3).

The source of the above depicted deviations are deviations in the behaviour of every individual sensor's resistance from the standardized curve. Thus, it was at this point where the measures described in the following were taken to improve the sensitivity of the used Pt100 sensors against each other. Prior to the installation in the experimental setup, every Pt100 sensor was taken with its cabling

already attached and its resistance was measured at two temperatures:

- 273.15 K using iced distilled water
- 76.90 K using the boiling point of nitrogen at a measured  $p_{atm}$

With the measured resistances, an individual resistance curve was created for every sensor. The starting point was the extended resistance curve (see Fig. 3.7 in every case. The two measured resistances served as fixpoints for its individual alteration. It can be divided into two consecutive steps:

1. offsetting the whole curve range of interest (20...300 K) by  $\Delta R$  so that it passes through the measured resistance at 76.90 K. All values for  $\Delta R$  were in the range of  $-0.87...-0.73 \Omega$  which, in the given temperature range of the experiments converts to an error in  $\Delta T$  between two sensors of up to 1 K.
2. using the second fixpoint at 273.15 K to exclusively adjust the slope of the linear resistance curve part so that it passes through said point. The curve was determined to follow a linear fit starting from 70 K via determination of the original curve's derivative.

## D Calculation of Measurement Uncertainties

In this part of the appendix, three different result uncertainty calculations executed within this thesis shall be described in further detail. All measurement inaccuracies of the used devices can be found in Appendix B.

### Joule Heating Errors

The electric heater outputs throughout this thesis were calculated according to equation (3.12). The voltages were measured with a National Instruments® PXI-4071 Multimeter (Cryocooler Performance) and an Astro-Med® Dash 18X Data Acquisition Recorder (Heat Transfer Experiments). The currents were measured by a R&S® HM8143 (Cryocooler Performance) and an Agilent® 34401A respective an Aim® TTI PLH120 (Heat Transfer Experiments). To calculate the final uncertainty in power output, the error propagation from the measurements of  $U$  and  $I$  has to be considered and the following correlation is obtained using equation (3.20):

$$s_C(\bar{Q}) = \sqrt{I^2 \cdot s_B^2(\bar{U}) + U^2 \cdot s_B^2(\bar{I})} \quad (\text{D.1})$$

Thus, the type B uncertainties of the voltage and current measurements  $s_B^2(U)$  and  $s_B^2(I)$  had to be calculated using the inaccuracies of the used devices and equation (3.19) which yielded

$$s_B(\bar{I}) = \frac{2 \cdot \Delta I}{\sqrt{12}} \quad (\text{D.2})$$

for the current measurement uncertainty and the voltage measurement accordingly.



## Temperature Errors

In all temperature measurement cases of this work, the result values were obtained via calibration curves defining the correlation between sensor resistance and temperature. The resistance was always indirectly measured according to section 3.3.4 using  $U$  and  $I$  via Ohm's law:

$$R_{el} = \frac{U}{I} \quad (D.3)$$

The currents were provided by Lakeshore<sup>®</sup> 120 current sources. Voltages were measured by a National Instruments<sup>®</sup> PXI-4071 Multimeter (Cryocooler Performance) and an Astro-Med<sup>®</sup> Dash 18X Data Acquisition Recorder (Heat Transfer Experiments). Again, for the final uncertainty in the electrical resistance determination, the error propagation of  $\Delta U$  and  $\Delta I$  had to be considered using equation (3.20) which yielded:

$$s_C(\bar{R}_{el}) = \sqrt{\left(\frac{1}{I}\right)^2 \cdot s_B^2(\bar{U}) + \left(-\frac{U}{I^2}\right)^2 \cdot s_B^2(\bar{I})} \quad (D.4)$$

The type B uncertainties  $s_B^2(U)$  and  $s_B^2(I)$  were calculated according to equation (D.2). To obtain the temperature uncertainties  $s_C(T)$ , another error propagation had to be calculated with the results yielded by equation (D.8). In order to use equation (3.20) for this, the local derivative at the measured value of  $R_{el}$  had to be calculated from the individual inverse resistance curve  $T(R_{el})$  for the respective sensor. Substituted into equation (3.20) it simplifies to

$$s_C(T) = \left(\frac{\delta T(R_{el})}{\delta R_{el}}\right)_{\bar{R}_{el}} \cdot s_C(\bar{R}_{el}). \quad (D.5)$$

However, this is only the uncertainty caused by the measurement inaccuracies of  $R_{el}$ . Also the guaranteed maximum deviations of  $T(R_{el})$  from the real temperature given by the manufacturer have to be accounted for. Their contribution to the overall temperature uncertainty was calculated according to equation (3.19) and then added to  $s_C(T)$  to receive the final uncertainty of the temperature measurements.

The values depicted in Fig. 4.5 and their uncertainties obtained via this procedure are tabulated in the following table.

## Heat Loads through Cryogel<sup>®</sup>Z - Errors

As discussed in section 6.1, the errors of  $\dot{Q}_{i,CG}$  can be assumed to be exclusively dependent on the linear fit quality of the HMCs. This correlation shall be described in the following.

The linear regression was conducted with the help of OriginPro<sup>®</sup> 2016 in all cases. It yielded the slope  $\bar{b}$  and the intercept  $\overline{\Delta T}_0$  value. These were used to calculate  $\dot{Q}_i$  according to the following equation:

$$\bar{\dot{Q}}_{i,CG} = \frac{\overline{\Delta T}_{0,i}}{\bar{b}_i} \quad (\text{D.6})$$

The regression also yielded the uncertainties  $s(\bar{b}_i)$  and  $s(\overline{\Delta T}_{0,i})$ . Thus, with equations (3.20) and (D.6) one obtains

$$s_C(\bar{\dot{Q}}_{i,CG}) = \sqrt{\left(\frac{1}{\bar{b}_i}\right)^2 \cdot s^2(\overline{\Delta T}_0) + \left(-\frac{\overline{\Delta T}_{0,i}}{\bar{b}_i^2}\right)^2 \cdot s^2(\bar{b}_i)}. \quad (\text{D.7})$$

To receive the uncertainty of  $\dot{q}_{i,CG}$ , the values  $s_C(\bar{\dot{Q}}_{i,CG})$  were divided by the Cryogel<sup>®</sup>Z stack cross section  $A_{CG} = 2 \cdot 0.2513 \text{ m}^2$ :

$$s_C(\bar{\dot{Q}}_{i,CG}) = \frac{s_C(\bar{\dot{Q}}_i)}{A_{CG}} \quad (\text{D.8})$$

## E Parasitic Heat Load Estimation

To allow for a better evaluation of the experimentally obtained values for  $\dot{Q}_{i,CG}$ , approximate values were calculated for all terms contributing to the overall parasitic heat load on the thermal shield and the cold mass of the experimental setup. For comparability reasons to the values stated in Table 6.1, the parasitic heat loads were scaled up to heat fluxes  $\dot{q}_{i,CG}$  per  $\text{m}^2$  of Cryogel<sup>®</sup>Z insulation as well. To be able to correct all measured  $\dot{q}_{i,CG}$ , the parasitic heat load calculations were performed for all thermal conditions during the experiments. The used equations can be found in section 3.1. The respective results are tabulated in Tables E.1 to E.4.

Table E.1: Approximated parasitic heat loads for  $\bar{T}_{1st} = 35.3 \text{ K}$  and  $\bar{T}_{2nd} = 5.45 \text{ K}$ .  $\dot{Q}_{1,CG}$  was not measured at these temperatures.

Contribution	2 <sup>nd</sup> Stage Value / $\frac{\text{W}}{\text{m}_{\text{CG}}^2}$
$\dot{q}_{rad}$	negl.
$\dot{q}_{gas}$	negl.
$\dot{q}_{solid}$	0.005
$\sum \dot{q}_i$	0.005

Table E.2: Approximated parasitic heat loads for  $\bar{T}_{1st} = 40.3 \text{ K}$  and  $\bar{T}_{2nd} = 5.83 \text{ K}$

Contribution	1 <sup>st</sup> Stage Value / $\frac{\text{W}}{\text{m}_{\text{CG}}^2}$	2 <sup>nd</sup> Stage Value / $\frac{\text{W}}{\text{m}_{\text{CG}}^2}$
$\dot{q}_{rad}$	1.89	0.001
$\dot{q}_{gas}$	0.01	negl.
$\dot{q}_{solid}$	0.41	0.005
$\sum \dot{q}_i$	2.31	0.006

Table E.3: Approximated parasitic heat loads for  $\bar{T}_{1st} = 52.7 \text{ K}$  and  $\bar{T}_{2nd} = 6.80 \text{ K}$

Contribution	1 <sup>st</sup> Stage Value / $\frac{\text{W}}{\text{m}_{\text{CG}}^2}$	2 <sup>nd</sup> Stage Value / $\frac{\text{W}}{\text{m}_{\text{CG}}^2}$
$\dot{q}_{rad}$	1.84	0.002
$\dot{q}_{gas}$	0.01	negl.
$\dot{q}_{solid}$	0.40	0.005
$\sum \dot{q}_i$	2.25	0.007

Table E.4: Approximated parasitic heat loads for  $\bar{T}_{1st} = 80.3 K$  and  $\bar{T}_{2nd} = 15.91 K$ 

Contribution	1 <sup>st</sup> Stage Value / $\frac{W}{m_{CG}^2}$	2 <sup>nd</sup> Stage Value / $\frac{W}{m_{CG}^2}$
$\dot{q}_{rad}$	1.71	0.002
$\dot{q}_{gas}$	0.01	negl.
$\dot{q}_{solid}$	0.34	0.004
$\sum \dot{q}_i$	2.06	0.006

Due to the low pressure inside the cryostat ( $3 \dots 4 \cdot 10^{-7}$  mbar) during all experiments, the contributions of  $\dot{Q}_{cond}$  and  $\dot{Q}_{sorp}$  could be neglected [29]. The low pressure was also responsible for the low values of  $\dot{q}_{gas}$ . It can furthermore be seen in the above tables that throughout all measured thermal conditions, the contribution of  $\dot{q}_{rad}$  on the first stage exceeds all others by far. This calls for a further look into its calculation at this point.

Following equations (3.5) and (3.6), in a first step,  $A_1$  and  $A_2$  were determined. In order to do so, the insulation of the cold mass with MLI against the cryostat walls need to be considered. This insulation is depicted below.

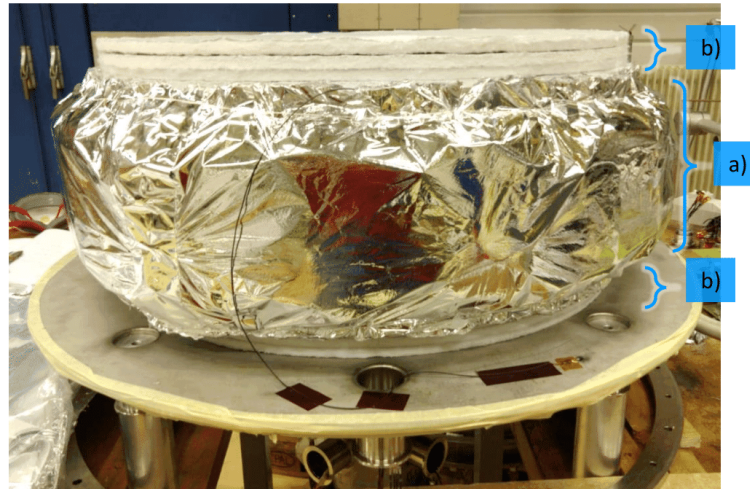


Figure E.1: MLI insulation of the experimental area against thermal radiation from the cryostat vessel walls (Photo by courtesy of V. Ilardi). a) nearly free-floating 20-layer MLI blanket, b) uncovered layers of Cryogel<sup>®</sup> Z.

Figure E.1 shows the relevant setup part for the calculation of  $\dot{q}_{rad}$ . A MLI blanket of 20 individual layers was loosely attached around all copper parts and a major part of the Cryogel Z with the help of thin fabric threads to avoid touching the cryostat top and bottom panel. The distances b) had to be left uncovered to avoid this thermal contact in compressed state during the experiments as well. Especially when considering that a lower Cryogel Z dilatation than expected was recorded during the compression (see section 5.2), this leaves an uncovered surface of Cryogel Z ( $A_1$ ) that is prone to receive thermal radiation from the stainless steel

vessel walls at room temperature. Thus, with the known  $\epsilon = -0.263$  during the experiments,  $A_1$  and its counterpart  $A_2$  could be approximated to  $0.113 \text{ m}^2$  and  $0.132 \text{ m}^2$  respectively. With the emissivity  $e_1 = 0.49$  of silica [61] which makes up the major part of the Cryogel Z layers seen from the side and  $e_2 = 0.08$  (stainless steel at 300 K [29]), merely  $T_1$  was left to be determined for every experimental case separately.  $T_2$  was always measured to be around 291 K during the respective experiments. Information about  $T_1$  was gained with the help of the conducted numerical simulations for section 6.2 which allowed the determination of the expected mean surface temperature of the concerning Cryogel Z layers in Fig. E.1 b). Its range was found to be between 271.1 K and 273.3 K.

For the calculation of  $\dot{q}_{solid}$  of every case, two influences were considered. Firstly, the parasitic heat load on both stages via the thermalized wires which was calculated using equation (3.7). Secondly, the heat conduction through the applied MLI insulation for which the benchmark stated in [29] was used (see also: Table 3.1).

## F Tabulated Result Values

### *In-Situ* Heat Meter Calibrations

Table F.1: Tabulated values for the HMC in Fig. 5.2.

$\dot{Q}_{EH222} / \text{W}$	$T(\text{TT23}) - T(\text{TT21}) / \text{K}$
$0 \pm 0$	0.185
$0.25 \pm 0.005$	0.205
$0.51 \pm 0.008$	0.230
$1.00 \pm 0.014$	0.271
$1.50 \pm 0.020$	0.311
$2.01 \pm 0.026$	0.362

Table F.2: Tabulated values for the HMC in Fig. 5.3 (a).

$\dot{Q}_{EH222} / \text{W}$	$T(\text{TT15}) - T(\text{TT10}) / \text{K}$
$0 \pm 0$	6.821
$5.05 \pm 0.046$	8.655
$10.06 \pm 0.090$	10.516
$15.01 \pm 0.134$	12.226
$20.14 \pm 0.180$	14.187

Table F.3: Tabulated values for the HMC in Fig. 5.3 (b).

$\dot{Q}_{EH222} / \text{W}$	$T(\text{TT22}) - T(\text{TT21}) / \text{K}$
$0 \pm 0$	2.148
$0.50 \pm 0.008$	2.609
$1.00 \pm 0.014$	2.980
$1.50 \pm 0.020$	3.369

Table F.4: Tabulated values for the HMC in Fig. 5.4 (a).

$\dot{Q}_{EH222} / \text{W}$	$T(\text{TT15}) - T(\text{TT12}) / \text{K}$
$0 \pm 0$	5.227
$10.06 \pm 0.090$	8.736
$15.01 \pm 0.134$	10.487
$20.11 \pm 0.180$	12.299

Table F.5: Tabulated values for the HMC in Fig. 5.4 (b).

$\dot{Q}_{EH222} / \text{W}$	$T(\text{TT23}) - T(\text{TT21}) / \text{K}$
$0 \pm 0$	0.269
$0.25 \pm 0.005$	0.630
$0.50 \pm 0.008$	0.715
$1.00 \pm 0.014$	0.707
$1.50 \pm 0.020$	0.916

Table F.6: Tabulated values for the HMC in Fig. 5.5 (a).

$\dot{Q}_{EH222} / \text{W}$	$T(\text{TT15}) - T(\text{TT10}) / \text{K}$
$0 \pm 0$	9.716
$5.02 \pm 0.045$	13.287
$7.54 \pm 0.068$	14.919
$10.06 \pm 0.090$	16.700
$15.06 \pm 0.135$	20.572

Table F.7: Tabulated values for the HMC in Fig. 5.5 (b).

$\dot{Q}_{EH222} / \text{W}$	$T(\text{TT22}) - T(\text{TT21}) / \text{K}$
$0 \pm 0$	4.240
$0.12 \pm 0.003$	4.294
$0.50 \pm 0.008$	4.488
$1.00 \pm 0.014$	4.771

## Cryomech<sup>®</sup>PT420 Capacity Map

Table F.8: Cooling capacity and temperature values of Fig. 4.5 with their respective errors.

$\dot{Q}_c(1^{st} \text{ stage}) / \text{W}$	$\dot{Q}_c(2^{st} \text{ stage}) / \text{W}$	$T(1^{st} \text{ stage}) / \text{K}$	$T(2^{nd} \text{ stage}) / \text{K}$
$75.2 \pm 0.09$	$1.51 \pm 0.053$	$53.9 \pm 0.83$	$3.92 \pm 0.014$
$74.9 \pm 0.09$	$1.97 \pm 0.061$	$54.3 \pm 0.82$	$4.22 \pm 0.009$
$75.1 \pm 0.09$	$2.49 \pm 0.069$	$56.0 \pm 0.81$	$4.62 \pm 0.008$
$75.1 \pm 0.09$	$3.01 \pm 0.075$	$55.6 \pm 0.81$	$4.89 \pm 0.008$
$75.0 \pm 0.09$	$3.51 \pm 0.081$	$56.2 \pm 0.82$	$5.13 \pm 0.011$
$74.9 \pm 0.09$	$4.05 \pm 0.088$	$56.3 \pm 0.81$	$5.33 \pm 0.012$
$75.2 \pm 0.09$	$4.50 \pm 0.092$	$56.9 \pm 0.81$	$5.53 \pm 0.014$
$80.1 \pm 0.10$	$1.51 \pm 0.053$	$57.3 \pm 0.80$	$3.90 \pm 0.014$
$80.0 \pm 0.10$	$1.97 \pm 0.061$	$58.5 \pm 0.80$	$4.24 \pm 0.009$
$80.0 \pm 0.10$	$2.49 \pm 0.069$	$58.8 \pm 0.79$	$4.60 \pm 0.008$
$79.9 \pm 0.10$	$3.02 \pm 0.075$	$57.6 \pm 0.80$	$4.87 \pm 0.008$
$79.9 \pm 0.10$	$3.51 \pm 0.081$	$58.6 \pm 0.79$	$5.08 \pm 0.011$
$80.0 \pm 0.10$	$4.06 \pm 0.088$	$58.9 \pm 0.79$	$5.33 \pm 0.012$
$80.0 \pm 0.10$	$4.51 \pm 0.093$	$59.5 \pm 0.79$	$5.56 \pm 0.014$
$84.5 \pm 0.10$	$1.50 \pm 0.053$	$59.8 \pm 0.79$	$3.90 \pm 0.014$
$85.0 \pm 0.10$	$1.97 \pm 0.061$	$61.3 \pm 0.78$	$4.24 \pm 0.009$
$85.0 \pm 0.10$	$2.49 \pm 0.069$	$61.1 \pm 0.78$	$4.60 \pm 0.008$
$84.5 \pm 0.10$	$3.02 \pm 0.075$	$60.7 \pm 0.78$	$4.86 \pm 0.008$
$85.3 \pm 0.10$	$3.49 \pm 0.081$	$61.5 \pm 0.77$	$5.07 \pm 0.011$

Table F.8 (continued): Cooling capacity and temperature values of Fig. 4.5 with their respective errors.

$\dot{Q}_c(1^{st} \text{ stage})$ / W	$\dot{Q}_c(2^{st} \text{ stage})$ / W	$T(1^{st} \text{ stage})$ / K	$T(2^{nd} \text{ stage})$ / K
85.1 ±0.10	4.06 ±0.089	61.7 ±0.77	5.34 ±0.008
85.2 ±0.10	4.52 ±0.093	61.9 ±0.77	5.69 ±0.015
90.3 ±0.11	1.50 ±0.053	63.2 ±0.76	3.91 ±0.014
90.4 ±0.11	1.97 ±0.061	64.2 ±0.76	4.25 ±0.009
90.4 ±0.11	2.49 ±0.069	64.3 ±0.76	4.63 ±0.008
90.0 ±0.11	3.01 ±0.075	63.5 ±0.76	4.86 ±0.008
90.2 ±0.11	3.51 ±0.082	64.8 ±0.75	5.13 ±0.011
89.9 ±0.11	4.06 ±0.088	64.5 ±0.75	5.51 ±0.014
90.0 ±0.11	4.51 ±0.092	64.7 ±0.75	5.98 ±0.018
94.9 ±0.11	1.51 ±0.053	65.6 ±0.75	3.95 ±0.014
95.0 ±0.11	1.96 ±0.061	66.1 ±0.74	4.25 ±0.009
95.0 ±0.11	2.51 ±0.069	66.2 ±0.74	4.65 ±0.008
95.2 ±0.11	3.02 ±0.076	65.9 ±0.74	4.88 ±0.008
95.0 ±0.11	3.51 ±0.081	66.6 ±0.74	5.23 ±0.013
94.9 ±0.11	4.06 ±0.088	66.2 ±0.74	5.63 ±0.015
95.2 ±0.11	4.48 ±0.092	66.5 ±0.74	6.26 ±0.018
98.3 ±0.12	1.51 ±0.053	66.6 ±0.74	3.93 ±0.014
98.4 ±0.12	2.01 ±0.062	67.4 ±0.73	4.23 ±0.009
97.6 ±0.12	2.48 ±0.068	67.5 ±0.73	4.65 ±0.008
98.3 ±0.12	3.02 ±0.076	67.5 ±0.73	4.92 ±0.008
98.4 ±0.12	3.49 ±0.081	67.9 ±0.73	5.35 ±0.012
97.1 ±0.12	4.06 ±0.088	67.9 ±0.73	5.77 ±0.015
97.8 ±0.12	4.48 ±0.092	68.4 ±0.73	6.77 ±0.020